Shear-wave Splitting in the Earth's Crust

Sheila Peacock

Doctor of Philosophy

University of Edinburgh

1986

DECLARATION

I declare that this thesis was composed by myself and that the work described was entirely my own unless otherwise stated.

ABSTRACT

Shear-wave splitting (birefringence or double refraction), the most diagnostic effect of anisotropy on seismic waves, has been observed in three separate experiments: downhole recordings of shear-wave vibrator signals in shale; records of aftershocks of the 1984 North Wales earthquake; and microearthquake records from the Anza seismic gap on the San Jacinto Fault, Southern California. In the shale, which is transversely isotropic with a vertical axis of symmetry, split shear waves have SH and SV polarizations and splitting is observed when the shear-wave vibrator baseplate is oriented so that both SH and SV waves are radiated towards the receiver. The anisotropy also causes the polarization of the SV component to deviate appreciably from perpendicular to the raypath. Both these results agree with theoretical predictions and are modelled successfully by synthetic seismograms.

In North Wales almost all shear-wave arrivals at four three-component seismic stations directly above the aftershock foci show anisotropy-induced shear-wave splitting. Polarizations of shear-wave first arrivals at one station sited on a granite outcrop are aligned with the northwest-southeast compressive axis of the regional stress field determined by independent methods, and the anisotropy is interpreted as being due to northwest-southeast striking stress-aligned, liquid-filled cracks and microcracks pervading the crust (extensive-dilatancy anisotropy or EDA). At least one station shows polarizations parallel to the cleavage of strongly anisotropic slate underlying the site. The observed seismograms are matched by synthetic seismograms of shear waves

propagating through layers of cracked rock and slate.

Polarizations of split shear waves recorded by a network in the Anza seismic gap indicate anisotropy with a north-south axis of symmetry, probably caused by EDA aligned in the regional stress field. At one network station, KNW, polarizations indicate a northwest-southeast stress field, and delays between split shear-wave arrivals from some events appear to increase significantly over the 29 months of recording. This increase in delay could be caused by the elastic "bowing" of microcracks as strain accumulates before an impending larger earthquake within the seismic gap. EDA has now been identified in many places around the world, but this is the first observation of temporal variations which may be precursory to an earthquake.

ACKNOWLEDGEMENTS

My greatest thanks go to Stuart Crampin, my supervisor, for his constant enthusiastic support and his patience, and for encouraging me to travel and finding funds for me to do so.

David Booth kindly guided me in using his anisotropic reflectivity program, and gave invaluable second opinions on many aspects of my thesis.

Russ Evans gave crucial assistance on many occasions, and he, Charlie Fyfe and Bob McGonigle were indispensable to my computing.

Everyone else in the Global Seismology Research Group of the British Geological Survey (BGS) helped me at some time. Chris Browitt, Head of the Group, allowed me to use the facilities. The Analysis Section (Jane Barker, Glen Ford, Peter Marrow, Richard Newmark, David Redmayne, Maureen Ritchie, Terry Turbitt, Alice Walker and various vacation students) did all the routine processing and location of the North Wales aftershocks, without which I could not have produced the results for Chapter 3. The Field Section (Peter Day, Stan Morgan, Dave Petrie and Dai Stewart) installed and maintained the instruments in North Wales. Bruce Hobbs, my University supervisor, and Ken Creer and other members of the Geophysics Department, supported me and saw very little of me in return. I am also grateful for support from Advisory staff and operators of the Edinburgh Regional Computer Centre, who helped to satisfy my greed for disk space and CPU time.

The postgraduate students in BGS gave me constant advice, suggestions, criticism and support: Elsa Aristodemou, Iain Bush, Pat Condon, Philippa Cooke, Liu Enru, Alan Logan, Colin MacBeth,

Andrew McDonald, Ian Main, Graham Roberts, Martin Russell and Jandyr Travassos.

I am grateful to James D. Robertson of Arco Oil and Gas for providing the shear-wave vibrator data for Chapter 2 and patiently answering my queries.

Jane Evans, Malcolm Howells, Tony Reedman, Brinley Roberts and W. E. Tremlett advised me on the geology of North Wales, and Brinley Roberts generously allowed me to reproduce part of his published geological map of the Lleyn Peninsula. David Taylor derived elastic constants for the slate model in the Chapter 3 synthetic seismograms.

In the United States, Joe Fletcher, Linda Haar, Tim MacDonald, Howard Bundock, Larry Baker, Sam Stewart and others at the U.S. Geological Survey, Menlo Park; and Frank Vernon of the University of California, San Diego, did all the routine processing of data from Anza, and were hospitable to me and helped me with my processing for Chapter 4. I am especially grateful to Linda and Robert Haar for having me to stay with them during my visits to California. Siobhan Clyde and Gavin Kerr helped with data processing in Edinburgh. Malcolm Clark advised me on statistics and Chen Tian-Chang helped with computing.

Balamir Üçer and his family, and Alan Logan, John Lovell and John McDonald helped make my stay in Turkey useful and enjoyable.

My studentship was financed by the Natural Environment Research Council (NERC), which also supported my visit to Turkey in September 1984. NERC, the IASPEI/IAVCEI Durham Fund, and IASPEI general funds financed my attendance at the 23rd General Assembly of the International Association of Seismology and Physics of the

Earth's Interior in Tokyo in August 1985. My visits to the USA were financed by NERC and by USGS grants 110177 and 14-08-0001-G1169.

CONTENTS

Enclosed in back cover:

Peacock, S., and Crampin, S., 1985. Shear-wave vibrator signals in transversely isotropic shale, *Geophysics*, **50**, 1285-1293.

CHAPTER 1

Introduction: seismic anisotropy in the Earth's lithosphere

1.1 Introduction

Anisotropy has recently come to prominence in seismology as evidence accumulates that it may be ubiquitous in the Earth's lithosphere (Crampin *et al.* 1984a, Crampin 1986a). Crampin (1986b) has pointed out that two types of anisotropy should be distinguished: vertical transverse isotropy, in which elastic properties vary only with incidence angle in the vertical plane; and general anisotropy in which properties also vary with azimuth. Effects of azimuthal anisotropy are observed in seismic records from diverse sites including the oceanic upper mantle (e.g. Raitt *et al.* 1969; Butler 1985); the continental upper mantle (Bamford 1977; Drummond 1985); the ocean crust (White and Whitmarsh 1984; Shearer and Orcutt 1985); the continental crust in earthquake zones (Crampin *et al.* 1985; Crampin and Booth 1985; Buchbinder 1985; Crampin *et al.* 1986a; Kaneshima *et al.* 1986a and other references cited by Crampin 1986a); beneath a dormant volcano (Kohler *et al.* 1982; Crampin *et al.* 1986b); a hot-dry-rock geothermal reservoir (Roberts and Crampin 1986); and a sedimentary basin (Crampin and Bush 1986; Crampin *et al.* 1986c). Transverse isotropy alone is less common, and has been reliably observed only in seismic exploration of horizontally bedded sedimentary rocks on land and undersea (Robertson and Corrigan 1983; Puzyrev *et al.* 1984; Carlson *et al.* 1984; Banik 1984; Davis and Clowes 1986).

This widespread occurrence in various tectonic and geological settings reflects the diversity of causes of anisotropy and

underlines the necessity of considering it in seismic experiments of all types. Correct interpretation of anisotropic effects can lead to improved understanding of present and ancient stress fields, geological structure and tectonic processes, and is important to mining, drilling and excavation (Crampin 1981, 1985a; 1986a, c; Doyle *et al.* 1982, 1985; Crampin *et al.* 1980, 1984a).

1.2 Causes of anisotropy

Four causes of seismic anisotropy are most commonly invoked to explain field observations:

1. Aligned anisotropic crystals (crystalline anisotropy)
2. Aligned non-spherical sediment grains (lithological anisotropy)
3. Periodic thin layering of isotropic materials (PTL anisotropy)
4. Aligned cracks and microcracks (extensive-dilatancy anisotropy, EDA)

Several other possible causes of anisotropy are listed by Crampin *et al.* (1984a), but have not so far been observed.

1.2.1 Aligned anisotropic crystals

Anisotropic crystals may be aligned by plastic flow or crystallization under stress (Babuška 1984). The alignment of *a*-axes of orthorhombic olivine and *c*-axes of orthorhombic pyroxene crystals parallel to the direction of flow are thought to cause the observed anisotropy in the upper mantle (Hess 1964; Francis 1969; Ave'Lallemant and Carter 1970; Christensen 1984), while in the Antarctic ice sheet, overall anisotropy is caused by hexagonal ice crystals with *c*-axes parallel to the flow direction (Bentley 1971).

Anisotropy, along with cleavage, schistosity or banding, is caused in slate, schist and gneiss by recrystallization of minerals under stress, especially micas with *c*-axes parallel to the direction of maximum compression (Christensen 1965, 1966; Harker 1950). The observed anisotropy in all rocks with aligned crystals may be caused by a combination of the inherent anisotropy of the individual crystals and the effective anisotropy caused by cracks along grain boundaries (Simmons and Richter 1976; S. Crampin, personal communication) and cleavage cracks along the cleavage planes within a grain (Simmons and Richter 1976; Kranz 1983). These cracks will tend to be closed if they are not near-parallel to the maximum compressive stress.

1.2.2 Aligned non-spherical sediment grains

Elongated or flattened sediment grains may be aligned during deposition or by subsequent compaction or plastic flow deformation, to cause overall anisotropy (Crampin *et al.* 1984a), which may be enhanced if the grains are intrinsically anisotropic. In shales and clays, for instance, the thin platy crystals of clay minerals settle out of water to lie flat on the depositional surface. Aligned pore space in bedding planes may contribute to the anisotropy. Lithological anisotropy has been observed in shale by Kaarsberg (1968), Robertson and Corrigan (1983) and Banik (1984); in clays by Puzyrev *et al.* (1984) and Brodov *et al.* (1984); and in submarine turbidites by Davis and Clowes (1986).

Crystalline and lithological anisotropy are inherent in a rock and continuous at all length scales greater than the size of the grain (Crampin *et al.* 1984a), and I shall use the term *intrinsic*

anisotropy to cover both and to distinguish them from other types of anisotropy which are dependent on external conditions or length scale.

1.2.3 Periodic thin layering of isotropic materials

The effective anisotropy of repeated thin layers of isotropic materials to seismic waves of length greater than the repeat distance is well established by theory (Postma 1955; Levin 1978; Helbig 1984). In practice this type of anisotropy is often combined with anisotropy caused by aligned sediment grains in one or more of the repeating layers (Puzyrev *et al.* 1984). It has been observed in laboratory experiments including those of Melia and Carlson (1984) on glass-epoxy models and Zykov *et al.* (1984) on ice-clay models; in layers of clay and calcareous ocean sediments by Carlson *et al.* (1984); and coexisting with crack-induced azimuthal anisotropy in the Paris Basin (I. Bush, personal communication).

1.2.4 Crack-induced anisotropy

A rock containing a set of aligned joints, cracks, microcracks or pores is effectively anisotropic (Crampin 1978; Crampin *et al.* 1984a). Effective elastic constants of media pervaded by aligned empty or fluid-filled microcracks are given by Crampin (1978) from the velocity variation formulae of Garbin and Knopoff (1973, 1975a, b); and by Hudson (1980, 1981; Crampin 1984b). Cracks at all depths in the Earth's crust are probably fluid-filled (Crampin and Atkinson 1985): the fluid may be water of meteoric or metamorphic origin (Fyfe *et al.* 1978), water at supercritical temperatures

(Crampin *et al.* 1986b), or in some places, liquid or gaseous hydrocarbons (Crampin 1984a), or possibly primordial methane and other gases (Gold and Soter 1980). The pore-fluid pressure in these inclusions is likely to be close to lithostatic (Gold and Soter 1980; Crampin *et al.* 1984b), holding the cracks open at all depths in the crust. Water-filled cracks have been found at depths of 12 km in the Kola deep borehole, USSR (Koslovsky 1984), and fluid-filled cracks have been cited to explain electrical conductivity results from the lower crust (Shankland and Ander 1983; Gough 1986) and "bright spots" in deep seismic reflection records (Brown *et al.* 1985; Blundell 1985).

Cracks, microcracks and pores are abundant in crustal rocks (Simmons and Richter 1976) and are controlled by many factors (Crampin and Atkinson 1985). Cracks along the boundaries (Simmons and Richter 1976) of aligned crystals and grains have already been mentioned as contributing to intrinsic anisotropy; but the most important cause of crack alignment in the crust is non-hydrostatic stress (Nur and Simmons 1969; Hadley 1975; Crampin 1978, 1985b; Crampin *et al.* 1980; Atkinson 1982, 1984). Low stresses cause preferential opening and subcritical growth of existing cracks parallel to the direction of maximum compression, probably by the mechanism of stress corrosion by fluids at the stress concentrations at crack tips (Atkinson 1979, 1982, 1984) and elastic "bowing" of crack walls (Crampin *et al.* 1984b). Stress corrosion occurs at the tips of existing fluid-filled cracks of any orientation: the new growth is parallel to the direction of maximum compressive stress (Kranz 1983). If the existing crack is not parallel to the direction of maximum compression, it closes,

expelling its fluid content into the new cracks at its tips (Kranz 1983, S. Crampin, personal communication). There is evidence, summarized by Crampin and Atkinson (1985) and Crampin (1985b, 1986a), that local and regional stress fields cause alignment of cracks, and hence anisotropy, throughout the Earth's crust. These pervasive stress-aligned cracks have been called *extensive-dilatancy anisotropy* (EDA) by Crampin *et al.* (1984b). It is not possible to examine these cracks in hand specimens or borehole walls because drilling or mining the rock *in situ* or extracting rock specimens changes the stress field, causing the crack alignment to alter or disappear; and experiments on laboratory specimens cannot reproduce all the factors affecting cracks at depths greater than a few metres in the Earth's crust (Crampin and Atkinson 1985).

At high stress intensities (Atkinson 1984) conventional dilatancy occurs (Brace *et al.* 1966): new cracks open parallel to the direction of maximum compression, cracks become interconnected, and there is shear dislocation along cracks, leading to permanent strain. Rapid crack growth and failure of the rock finally occurs at stress intensities up to two orders of magnitude higher than the lowest values at which subcritical crack growth has been observed (Crampin *et al.* 1984b). These high stress intensities occur in the Earth's crust only at the nucleation point of earthquakes (Crampin *et al.* 1984b).

1.3 Extensive-dilatancy anisotropy (EDA) and earthquake prediction

Changes in stress can affect large volumes of rock around the focus of an impending earthquake, as indicated by changes in strain determined by geodetic surveys (summarized in Rikitake 1976);

changes in the coefficient b in the earthquake frequency-magnitude equation $\log N = a - bM$ (Smith 1986); and other precursors (Dobrovolsky *et al.* 1979), which can be detected hundreds of kilometres from the eventual epicentre. Precursory changes in the velocity ratio of P- and shear waves, V_p/V_s (Semenov 1969; Aggarwal *et al.* 1973; Whitcomb *et al.* 1973; Ohtake 1973); and in seismic wave attenuation (Sato 1986), have been attributed to crack growth under high stress (Mjachkin *et al.* 1975) and movement of fluids in cracks (Scholz *et al.* 1973), but since stresses high enough to cause conventional dilatancy are restricted to the immediate focal zone of the impending earthquake, it is probable that these precursors are caused by modifications to EDA cracks at lower stresses (Crampin *et al.* 1984b). The changes in velocity and attenuation of seismic waves caused by changes in aligned cracks will vary spatially (Crampin 1984b), and on some raypaths no change may occur. The apparently random spatial variation of observed changes (e.g. Sato 1986) and their apparent absence in some experiments (e.g. Boore *et al.* 1975) may be a consequence of the distribution of recording stations with respect to the crack alignment (Crampin 1978; Crampin *et al.* 1980, 1984b).

Changes in stress can cause changes in crack orientation, size, density and aspect ratio (Crampin 1986a). Changes in aspect ratio by elastic "bowing" of crack walls occur immediately when stress is applied, and may be the first observable precursor (Peacock *et al.* 1986: see Chapter 4). Laboratory measurements have shown that anelastic subcritical crack growth in response to stress change is rapid enough to cause detectable changes in crack size within a useful time interval for prediction (days, months or years, Crampin

et al. 1984b). Systematic analysis of anisotropic changes in velocity and attenuation caused by changes in crack parameters may allow detection of stress changes well in advance of a large earthquake (Crampin *et al.* 1984b; Crampin 1986a).

1.4 Effects of anisotropy on seismic body waves

Crampin (1981, 1984c) gives a comprehensive description of seismic wave propagation in anisotropic media, from which this brief summary is drawn.

In isotropic media, body waves are of two types: compressional (P) waves, polarized parallel to the direction of propagation, and shear (S) waves, which may be polarized in any direction in the plane perpendicular to the direction of propagation (Fig. 1.1a). In an anisotropic medium, three types of body waves propagate, with polarizations not in general parallel or perpendicular to the direction of propagation (rigorously defined as the direction perpendicular to the surfaces of constant phase). The phase velocities of these waves vary with the direction of propagation through the anisotropic medium. The fastest wave, with polarization closest to the propagation direction, is labelled *quasi*-P (qP); the other two are *quasi*-S (qS1 and qS2), and for most directions of propagation have different velocities. The three waves with the same propagation direction have mutually orthogonal polarizations (Fig. 1.1b), which are fixed with respect to the axes of anisotropic symmetry of the medium for a given propagation direction. The orientation of the three mutually orthogonal polarizations with respect to both the direction of propagation and the medium varies with the direction of propagation.

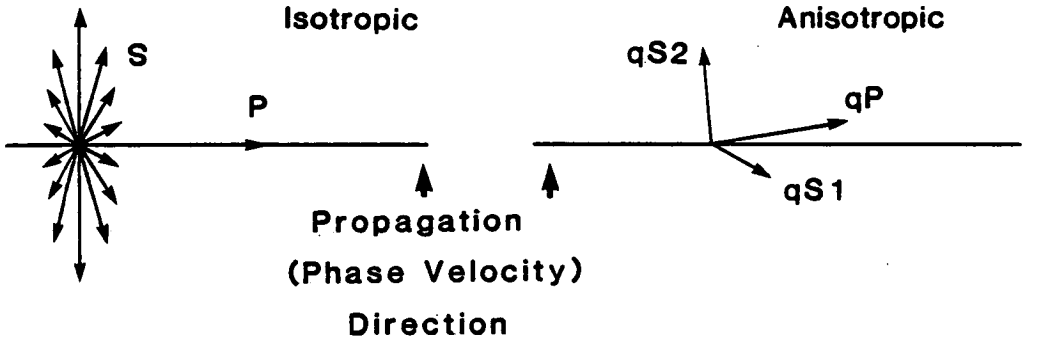

Fig. 1.1 Schematic diagrams showing particle-motion polarizations with respect to the propagation (phase-velocity) direction, of seismic body-waves in (a) isotropic and (b) anisotropic media. In an anisotropic medium the mutually orthogonal polarizations of the three body waves with coincident propagation direction are fixed within the medium. The waves in the anisotropic medium are denoted *quasi*-P (qP) and *quasi*-S (qS), as their polarizations are not exactly parallel (P) or perpendicular (S) to the propagation direction, as in isotropic media.

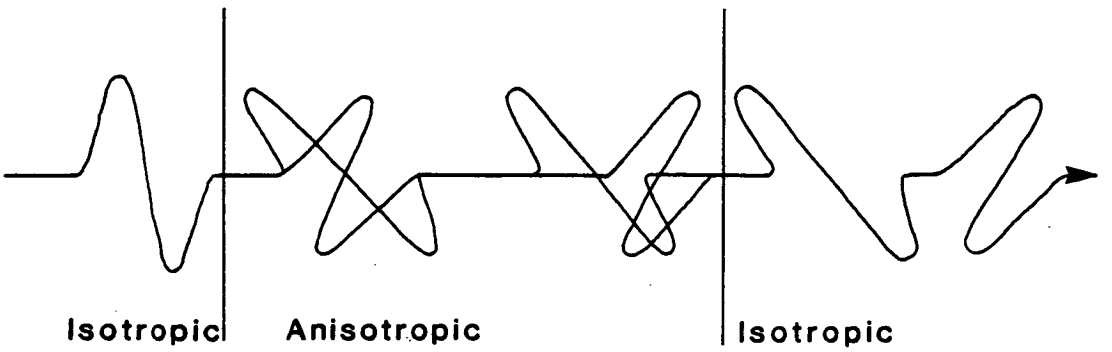

Fig. 1.2 Schematic illustration of shear-wave splitting. The shear wave (left) enters an anisotropic medium and is split into two or more components with polarizations fixed in the medium, which travel at different velocities and do not recombine into the original waveform on leaving the anisotropic medium.

As a consequence of the phase velocities varying with propagation direction, the group-velocity directions (directions of energy transport, seismic ray directions) of the three waves in anisotropic media deviate from the propagation direction and are not coincident; the deviation varies with the direction of propagation. Conversely, the three waves with a common group-velocity direction have different propagation (phase-velocity) directions, and non-orthogonal polarizations. This is important since most field measurements yield group-velocity values while elastic properties of rock are usually considered as functions of phase propagation direction.

The attenuation of body waves in anisotropic media also varies with direction of propagation, approximately inversely as the velocity (Crampin 1981, 1984b), and may be described by the imaginary parts of complex elastic constants.

1.5 Detecting anisotropy

Propagation through an anisotropic medium leaves four distinctive effects on seismic body wavetrains (Crampin 1984a): variations of velocity and attenuation with direction of propagation; shear-wave splitting; and polarization anomalies. Observations of the last two may be complicated by the effects of the free surface (Crampin 1984d; Booth and Crampin 1985).

1.5.1 Velocity and attenuation variations

Determinations of velocity and attenuation variations with direction require many accurately known travel times and paths, since the velocity and attenuation variations due to anisotropy in

the Earth are often small (Crampin *et al.* 1986b; Crampin 1985a). Even if accurate measurements are available, the effects of anisotropy may be confused with those of inhomogeneity, or may be ambiguous and interpretable by an alternative isotropic model (e.g. Drummond 1985). Unlike shear-wave splitting and polarization anomalies, velocity variations with direction can be detected with single-component seismometers, and until recently most reports of anisotropy have come from studying variations of P-wave velocity with azimuth or incidence angle because most field experiments, especially reflection and refraction surveys, have used single-component instruments (e.g. Raitt *et al.* 1969 and Bamford 1977 on the upper mantle, Kohler *et al.* 1982 on Mount Hood, Oregon, USA, and Bentley 1971 on anisotropic ice).

There is little experimental data on attenuation anisotropy, because of the difficulty in measuring attenuation (Crampin 1986a) and distinguishing between the effects of anisotropy and inhomogeneity. Young *et al.* (1984) have used attenuation anisotropy in small-scale experiments to determine crack orientation and density behind the rock faces of opencast coal mines.

1.5.2 Shear-wave splitting

A shear wave entering an anisotropic medium is generally split into three component waves, qS1, qS2 and qP, with orthogonal polarizations fixed in the medium (Crampin 1981). The three waves travel at different velocities and become separated from each other. The separation of the two quasi-shear waves and the components of their polarizations perpendicular to the direction of propagation persist during subsequent propagation through isotropic

media, and a three-component seismometer receives three distinct arrivals with different polarizations (Keith and Crampin 1977a). In weakly anisotropic media the qP component is usually too small to be detected (Crampin 1984c), but on three-component recordings the separate arrivals of the two near-orthogonally polarized shear waves are the clearest diagnostic of anisotropy (Fig. 1.2). The polarizations are not generally exactly orthogonal since the waves arriving at the seismometer have coincident group-velocity directions but not phase-velocity directions (Crampin 1984c). A single measurement of the polarization of the first-arriving shear wave can give the orientation of the axes of anisotropic symmetry, and the delay between the first and second shear-wave arrivals indicates the degree of anisotropy along the raypath (Crampin 1985a).

1.5.3 Polarization anomalies

The angle between the polarization and group-velocity directions of qP and qS waves can be measured at a receiver in contact with an anisotropic medium if the group-velocity direction can be determined independently (e.g. by assuming straight raypaths). For qP waves the deviation of polarization direction from group-velocity direction is small (Crampin *et al.* 1982). For qS waves the deviation of polarization from perpendicular to the group-velocity direction may be large (Crampin 1978), but will be difficult to measure accurately if the shear-wave arrival is superimposed on a P-wave coda. With a source of pure shear waves, such as a shear-wave vibrator, and a medium in which there are no large-amplitude mode conversions at interfaces, the deviation can

be measured, but the measured values may still be inaccurate if inhomogeneity in the medium causes the group velocity to depart from the assumed direction (Peacock and Crampin 1985: see Chapter 2). In three-component vertical seismic profiles and other situations in which orientations of receivers are deduced from observed polarizations, systematic errors of several degrees in orientation could result from discounting the effects of anisotropy on polarizations and group-velocity directions (Crampin 1986c).

A receiver not in contact with an anisotropic medium records departure of polarizations from the propagation direction within the medium as anomalous mode conversions at the interfaces (Keith and Crampin 1977b). Any wave passing from an isotropic medium to an anisotropic medium is generally converted into three refracted waves, qP, qS1 and qS2, and three reflected waves, P, SH and SV, even for normal incidence (Keith and Crampin 1977a). On passing from the anisotropic medium to an isotropic medium, a qP or qS wave is converted into three reflected waves, qP, qS1 and qS2, and three refracted waves, P, SH and SV (Fig. 1.3). The generation of reflected and refracted SH by incident P and SV waves on a plane horizontal interface is peculiar to anisotropic media. Booth and Crampin (1983a, b) have modelled these anomalous waves from a hypothetical anisotropic upper mantle, but conclude that for the weak anisotropy in the real Earth the anomalous waves will generally be too small to be detected.

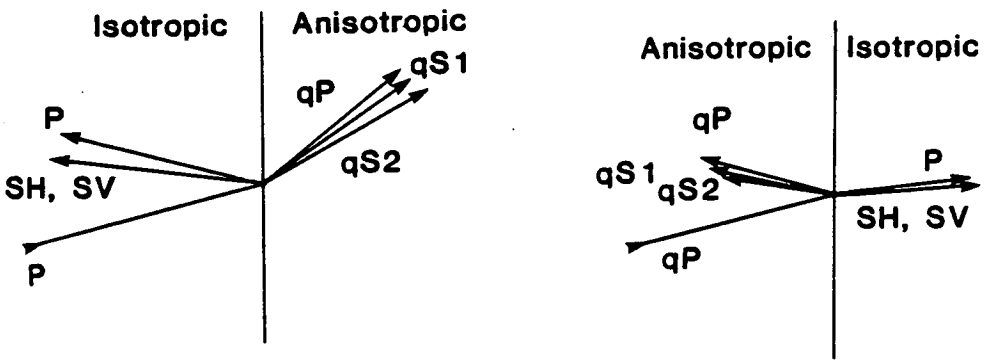

Fig. 1.3 Schematic diagrams of the refracted and reflected phases generated by (a) a P-wave incident from an isotropic medium on to the boundary with an anisotropic medium; (b) a qP wave incident from an anisotropic medium on to the boundary with an isotropic medium. At both interfaces anomalous phases with SH or near-SH polarizations are generated.

1.6 Free surface effects

The motion at the free surface caused by seismic waves incident from below does not correspond exactly to the motion at depth. Nuttli (1961) and Evans (1984a) have shown that for plane shear waves arriving at the surface of an isotropic medium, at angles of incidence less than arcsin V_S/V_P, the motion at the surface has approximately twice the amplitude of the motion at depth but otherwise reproduces the motion of the incident shear wave; but at greater angles of incidence shear waves suffer mode conversions and phase and amplitude changes, and reconstructing the motion at depth is impossible without detailed knowledge of the source, path and interfaces. For a surface station recording waves from a subsurface source, the critical angle arcsin V_S/V_P defines a *shear-wave window* (Evans 1984a; Crampin 1985a) around the epicentre of the source, within which the station must lie if shear-wave records from it are to be analysed for splitting or polarization anomalies. In practice the shear-wave window is not well defined, since curved wavefronts, low-velocity or anisotropic surface layers, surface topography, and focusing effects of topography and internal interfaces alter the incidence angle of shear waves (Evans 1984a; Crampin 1984d).

A curved SV wavefront incident on the surface at the critical angle is converted into a radially polarized local SP wave travelling along the surface. This local SP wave was predicted by Gilbert and Knopoff (1961) and Kawasaki *et al.* (1973), and has been observed in Turkey (R. Evans, private communication quoted in Booth and Crampin 1985). It decays rapidly with distance, but may be focused by topography to appear as a prominent, near-radial

precursor to the main shear-wave arrival and be misinterpreted as the first of a pair of split shear waves (Evans 1984a; Crampin 1984d).

Receivers in deep boreholes (depth greater than the seismic wavelength) do not suffer from these free-surface effects (Crampin 1985a).

1.7 This thesis

The three principal chapters of this thesis describe three different investigations of shear-wave splitting due to anisotropy in the Earth's crust. Chapter 2 is a study of the splitting and polarizations of the signal from a shear-wave vibrator received at a downhole geophone in transversely isotropic shale. Chapters 3 and 4 describe the effects of extensive-dilatancy anisotropy on shear waves from local earthquakes in two contrasting seismic zones. In Chapter 3 shear waves from aftershocks of the 1984 North Wales earthquake, a rare intraplate event at unusual depth, show evidence for alignment of cracks and microcracks in the regional stress field. In Chapter 4 evidence for crack-induced anisotropy is seen in shear waves from small earthquakes in the Anza seismic gap on the San Jacinto Fault, Southern California; and a temporal change in the characteristics of shear-wave splitting is observed for the first time, supporting the hypothesis that EDA may be used to predict earthquakes.

Discussion and some speculation are in Chapter 5.

CHAPTER 2

Shear-wave vibrator signals in transversely isotropic shale with a vertical axis of symmetry

(The contents of this chapter have been published as "Shear-wave vibrator signals in transversely isotropic shale", by S. Peacock and S. Crampin, 1985, *Geophysics*, **50**, 1285-1293.)

2.1 Introduction

A shear wave vibrator used with a three-component well geophone is a powerful tool for detecting and quantifying anisotropy in near-surface rock formations. There are three reasons for this: firstly, three-component records of shear wavetrains, from which polarizations can be determined, may contain more than three times as much information about the raypaths as equivalent recordings of P-wavetrains (Crampin 1985a); secondly, the signal from the shear-wave vibrator shows shear-wave polarizations relatively uncontaminated by P-waves; and thirdly, downhole recording avoids the complicated interactions of shear waves with the free surface (Nuttli 1961; Evans 1984a).

Robertson and Corrigan (1983) demonstrated the use of a shear-wave vibrator in deriving elastic constants and shear-wave surfaces in shales, in experiments aimed at determining the radiation pattern of the vibrator. In this chapter we present two results of reprocessing their data. The first is that shear-wave splitting may best be observed if the vibrator baseplate is oriented at an angle other than parallel or perpendicular to the shot-borehole line, since only then are both SH and SV waves

radiated towards the geophone. The second is that the SV-wave polarization deviates appreciably from perpendicular to the group-velocity direction, which in turn deviates from the phase-velocity direction. Both these observations are found to agree with theoretical results, and can be reproduced in synthetic seismograms.

2.2 The shear-wave vibrator experiments

Robertson and Corrigan performed their experiments at two sites: Geary, Oklahoma, on the Permian Dog Creek shale; and Sulphur Springs, Hopkins County, Texas, on the Eocene Wills Point Formation shale. The arrangement of source and geophone at both sites is shown in Fig. 2.1. At Geary the geophone depth was 430 ft (131 m); at Sulphur springs, 175 ft (53.3 m). At Geary they shot a single line out to 62° incidence angle, and also tested the azimuthal variation of the shear-wave vibrator signal by shooting with the baseplate at various orientations on a single site. At Sulphur Springs they shot out to incidence angles of 75° and 80° respectively along lines running east and north from the geophone. They present the data from both sites in the usual format for vibrator data, as cross-correlograms of the signal received at the geophone with the source signal measured by a velocity sensor on the baseplate.

Accurate straight-ray incidence angles at the geophone from each shotpoint are given at Sulphur Springs but not at Geary. The records from Geary are noisier than those from Sulphur Springs, and cover a smaller range of incidence angles, so we have concentrated on the data from Sulphur Springs.

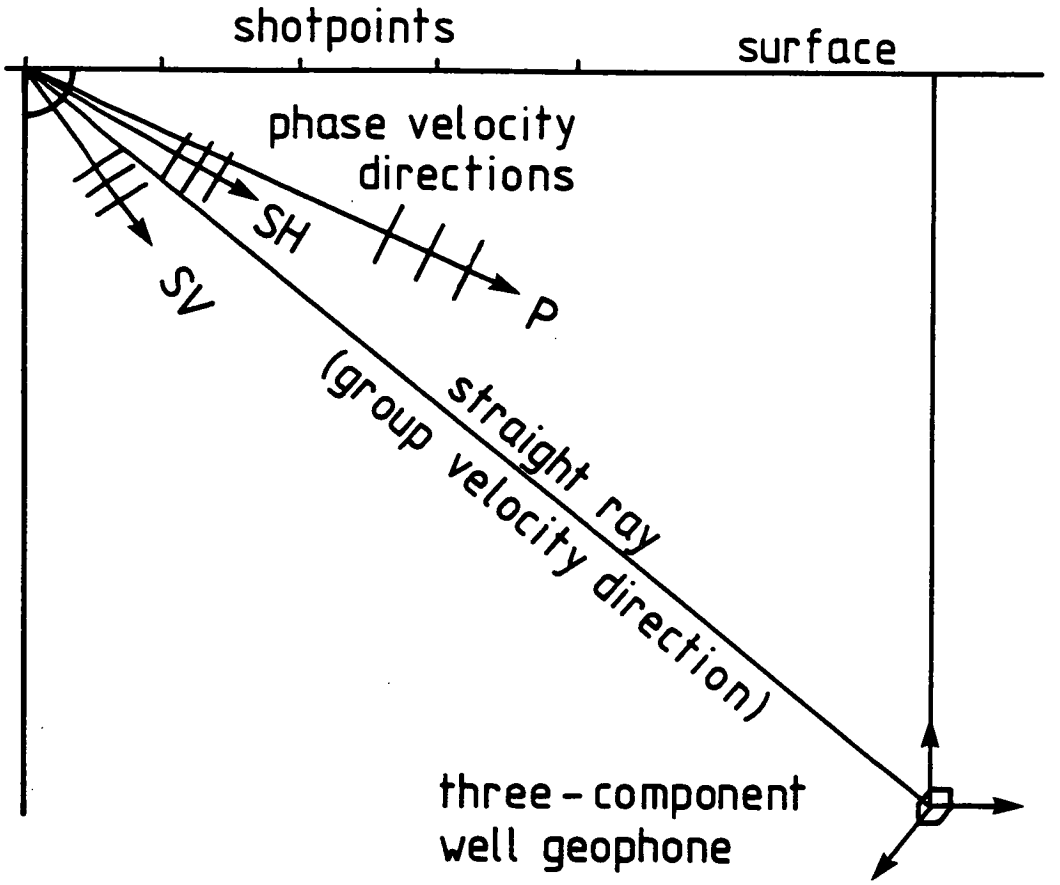

Fig. 2.1 Layout of the experiments by Robertson and Corrigan, showing schematic planes of constant phase and the divergence of phase velocity from group velocity in a transversely isotropic medium.

2.3 Data processing to reveal shear-wave splitting

J. D. Robertson provided the data displayed in Figs. 2, 3 and 6-10 of Robertson and Corrigan (1983) as digital records with sampling rate 500/s. Note that in Fig. 7 of Robertson and Corrigan (1983) the value of incidence angle θ along the bottom of the seismic section should run from 5° to 75°, not 10° to 80° (S. Crampin, J. D. Robertson, personal communication, 1983). The vibrator frequency was swept from 5 to 55 Hz in 10 seconds for each shot. Robertson and Corrigan processed the data in three stages: (1) correction for spherical divergence, (2) rotation of the horizontal component readings to parallel and perpendicular to the shot line, and (3) rotation of the radial and vertical components to lie parallel and perpendicular, respectively, to the direction of the incoming wave.

To speed up subsequent processing, we first halved the sampling rate of the digital records to 250/s. Aliasing should not be important as the highest vibrator frequency used at Sulphur Springs was 55 Hz and the data were filtered with a 62 Hz low-pass filter before being recorded.

2.3.1 Simulation of a mixed-polarity source

Direct observation of shear-wave splitting in a transversely isotropic medium with a vertical axis of symmetry requires a source of mixed SH- and SV-polarized shear waves, since the fixed polarizations of split shear waves in the medium are SH and SV (Crampin 1986b). Robertson and Corrigan (1983) showed that the shear-wave vibrator baseplate oriented along ('radial') or perpendicular ('transverse') to the shot-borehole line sends waves

of only one polarity along the line: SV waves from the radial baseplate, SH waves from the transverse baseplate. Intermediate orientations of the baseplate are required to give mixed polarity shear waves at the geophone. The azimuthal radiation test results from Geary, in Figs. 6 and 14 of Robertson and Corrigan (1983), show this mixed polarity signal; but since the test was performed at only one vibrator-geophone separation, we cannot see the variation of the signal with incidence angle. (There is no appreciable shear-wave splitting in the record of the azimuthal test, because the incidence angle, 35°, is close to a direction of singularity (Crampin 1981) of the shear-wave surfaces in the Geary shale seen in Fig. 11 of Robertson and Corrigan 1983.)

To show the variation of a mixed SH and SV signal with incidence angle, we simulated a shot with baseplate orientation 45° at each shotpoint of the polar radiation tests at Sulphur Springs (Figs. 7-10 of Robertson and Corrigan 1983) by vector addition of the signal from the radial and transverse baseplate shots. This procedure requires that the variation of amplitude of the vibrator signal with azimuth is sinusoidal for the SV component and cosinusoidal for the SH component. Sine and cosine curves in Fig. 14 of Robertson and Corrigan (1983) fit well the observations from the azimuthal radiation test in their Fig. 6. Two other requirements are that the input signals from the radial and transverse baseplate shots be as similar as possible, and that the two shots be made on exactly the same site. Cross-correlation removes source differences from the signals; and since there was no information about the difference in the vibrator position between radial and transverse baseplate shots, we have assumed that the

difference was less than the size of the baseplate.

2.3.2 Processing for SV polarization anomalies

We also investigated the angle between the SV polarization and group-velocity directions. Robertson and Corrigan had discovered that at high incidence angles the arrival angle of the SV wave appeared to be greater than the straight-ray incidence angle: they attributed this to an increase in velocity with depth in the rock causing the raypaths to curve (Fig. 2.2a). At each shotpoint they estimated the deviation of the SV arrival from the straight-ray direction by rotating the 'P' (radial) and 'SV' (perpendicular to the raypath in the vertical plane, in their notation) components of the signal from radial-baseplate motion to give maximum amplitude on the 'SV' component. This was their processing operation (3) described above. Its effect was to align the 'SV' component parallel to the direction of SV *polarization*, which in anisotropic media generally deviates from perpendicular to the group-velocity direction (Fig. 2.2b) (Crampin 1981, 1984c). The straight-ray incidence angles and apparent incidence angles derived from SV polarization are listed in Table 2.1.

As we did not know the actual group-velocity direction, only the angle between the straight-ray and SV polarization directions, we assumed that any increase in velocity in the rock did not cause the group velocity to deviate appreciably from the straight-ray direction, and rotated the 'P' and 'SV' components to lie along and perpendicular to the straight-ray direction. Deviation of SV polarization from perpendicular to the straight-ray direction then appears as a signal on the 'P' component, and comparison of the

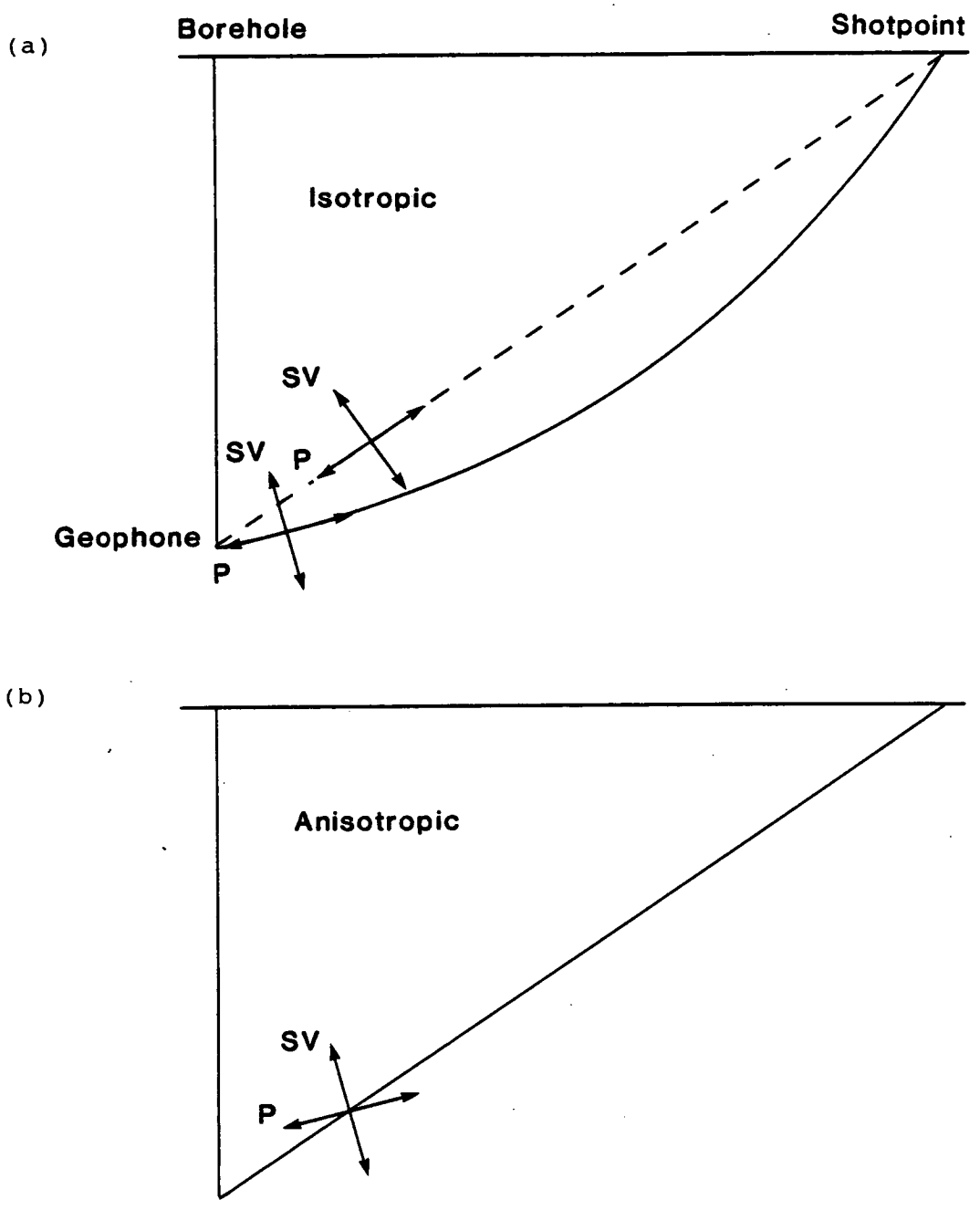

Fig. 2.2 Schematic diagrams showing raypaths (group velocity directions) and seismic wave polarizations in (a) an isotropic medium in which the velocity increases with depth (the straight raypath is shown for reference as a dashed line); (b) a homogeneous transversely isotropic medium with properties similar to those of the Sulphur Springs shale.

Table 2.1

SV-arrival-derived incidence angles and corresponding straight-ray angles at Sulphur Springs (Robertson, personal communication).

Incidence angles in degrees

East line		North line	
straight ray	SV-derived	straight ray	SV-derived
5	5	10	5
10	5	15	5
15	10	20	10
20	10	25	20
25	20	30	30
30	30	35	40
35	40	40	50
40	50	45	60
45	60	50	70
50	80	55	90
55	85	60	95
60	100	65	105
65	105	70	120
70	115	75	125
		80	130

observed angle of SV polarization from the straight-ray angle with theoretical angles between SV polarization and group-velocity direction will show the true deviation of group velocity from the straight raypath.

2.4 Results

Cross-correlograms from the Sulphur Springs site East and North shot lines are shown in Figs. 2.3 and 2.4. They show the mixed SH and SV signal from the simulated shots with the baseplate at 45°, and the small 'P' component signal accompanying the main SV arrival, caused by the deviation of the SV polarization from perpendicular to the straight-ray direction.

We measured travel times of SH and SV waves from these cross-correlograms and calculated velocities for each incidence angle, assuming straight raypaths. Travel-times were measured to the peak of the cross-correlation function.

2.4.1 Shear-wave splitting

The polarization diagrams (hodograms) in Fig. 2.5 are of the first shear-wave arrival from the simulated shots with the baseplate at 45° at Sulphur Springs. The axes of these plots have been restored to vertical, horizontal radial, and transverse, to show that shear waves are split into SH and SV components. The degree of splitting increases with increasing incidence angle, and complete separation of the faster SH from the slower SV wave occurs at incidence angles greater than 60°.

Fig. 2.3 Sulphur Springs test, East line: observed record sections with baseplate transverse (left) and baseplate radial (right), and simulated sections for baseplate at 45° (centre). Reference axes rotated for each shot: straight ray, 'P'; perpendicular to the straight ray in the vertical plane, 'SV'; and horizontal transverse, 'SH'.

Fig. 2.4 Sulphur Springs test, North line: notation as in Fig. 2.3.

Fig. 2.3

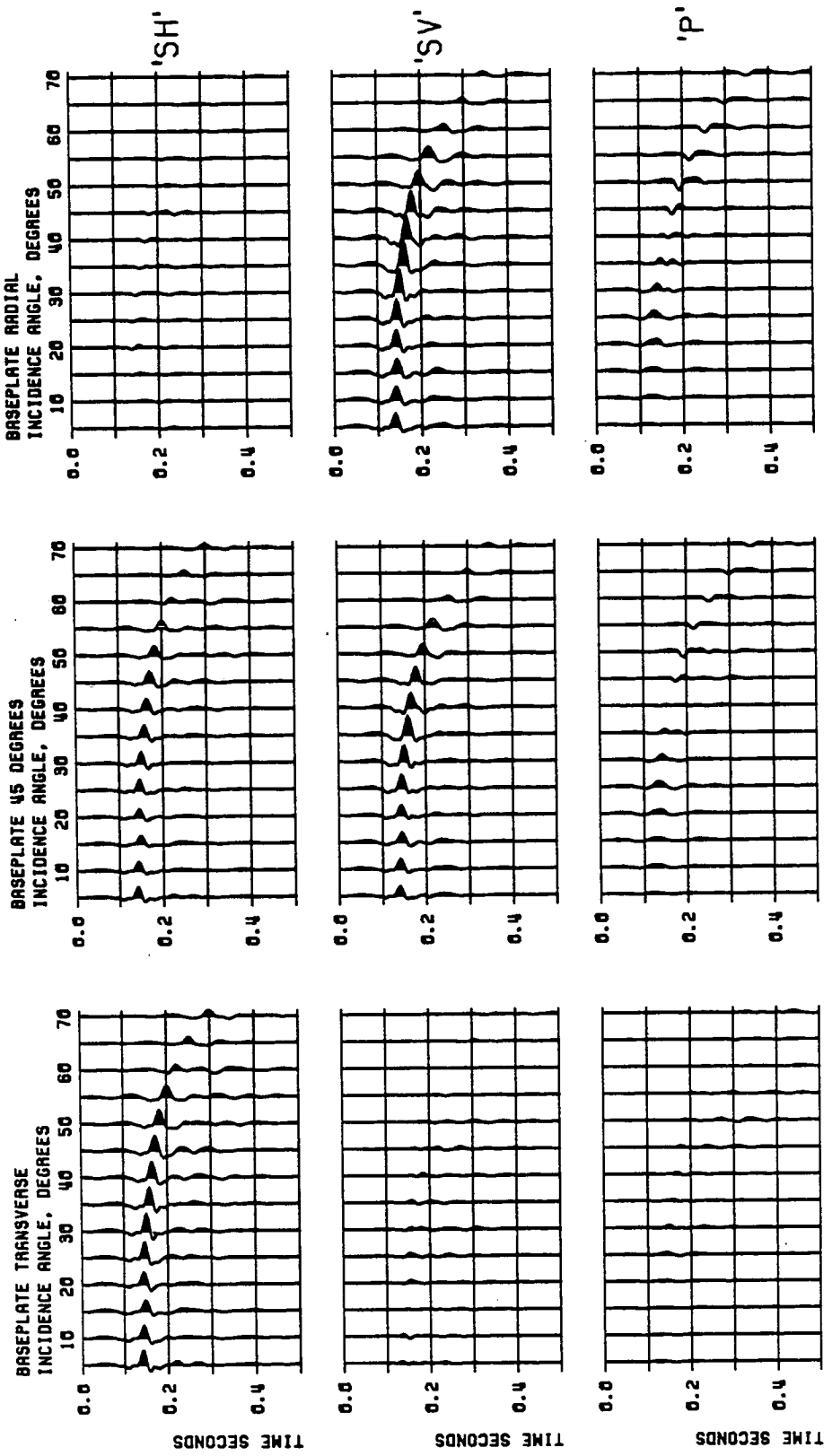
'SH'
'SV'
'P'
BASEPLATE RADIAL
INCIDENCE ANGLE, DEGREES
BASEPLATE 45 DEGREES
INCIDENCE ANGLE, DEGREES
BASEPLATE TRANSVERSE
INCIDENCE ANGLE, DEGREES
10 20 30 40 50 60 70
0.0 0.2 0.4
TIME SECONDS

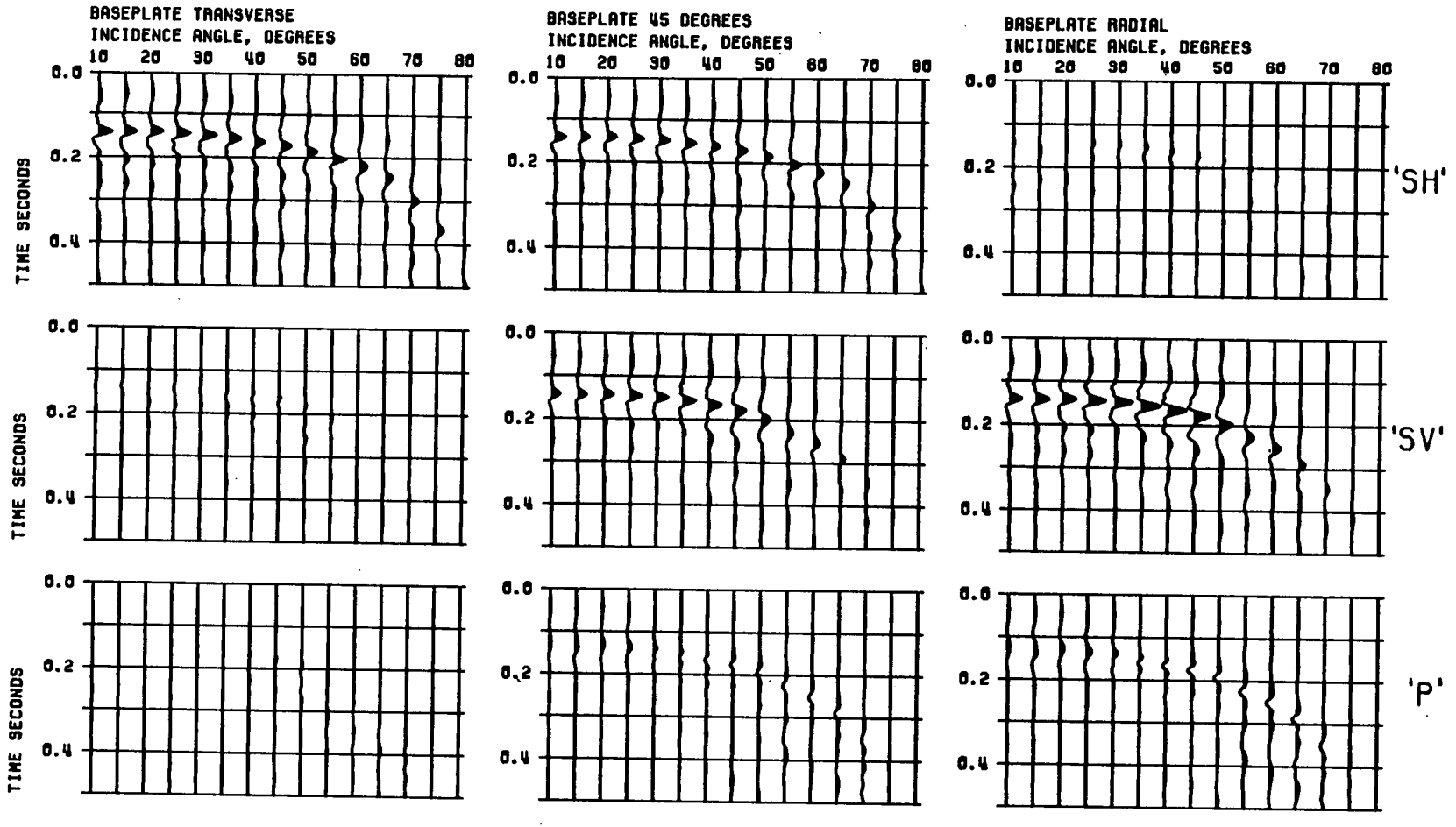
BASEPLATE TRANSVERSE
INCIDENCE ANGLE, DEGREES
10 20 30 40 50 60 70 80
BASEPLATE 45 DEGREES
INCIDENCE ANGLE, DEGREES
10 20 30 40 50 60 70 80
BASEPLATE RADIAL
INCIDENCE ANGLE, DEGREES
10 20 30 40 50 60 70 80
TIME SECONDS
0.0
0.2
0.4
'SH'
'SV'
'P'

Fig. 2.4

Fig. 2.5 Polarization diagrams from the simulated shots of Fig. 2.3 and 2.4 with the baseplate at 45°. (a) East line, from Fig. 2.3. (b) North line, from Fig. 2.4. (c) Corresponding polarization diagrams from synthetic records (Fig. 2.13). Axes rotated to vertical, horizontal radial, and horizontal transverse orientations. Motions shown are Up (U), Down (D), Towards (T) and Away (A) from the geophone, and Left (L) and Right (R) of the source to geophone line.

Fig. 2.5

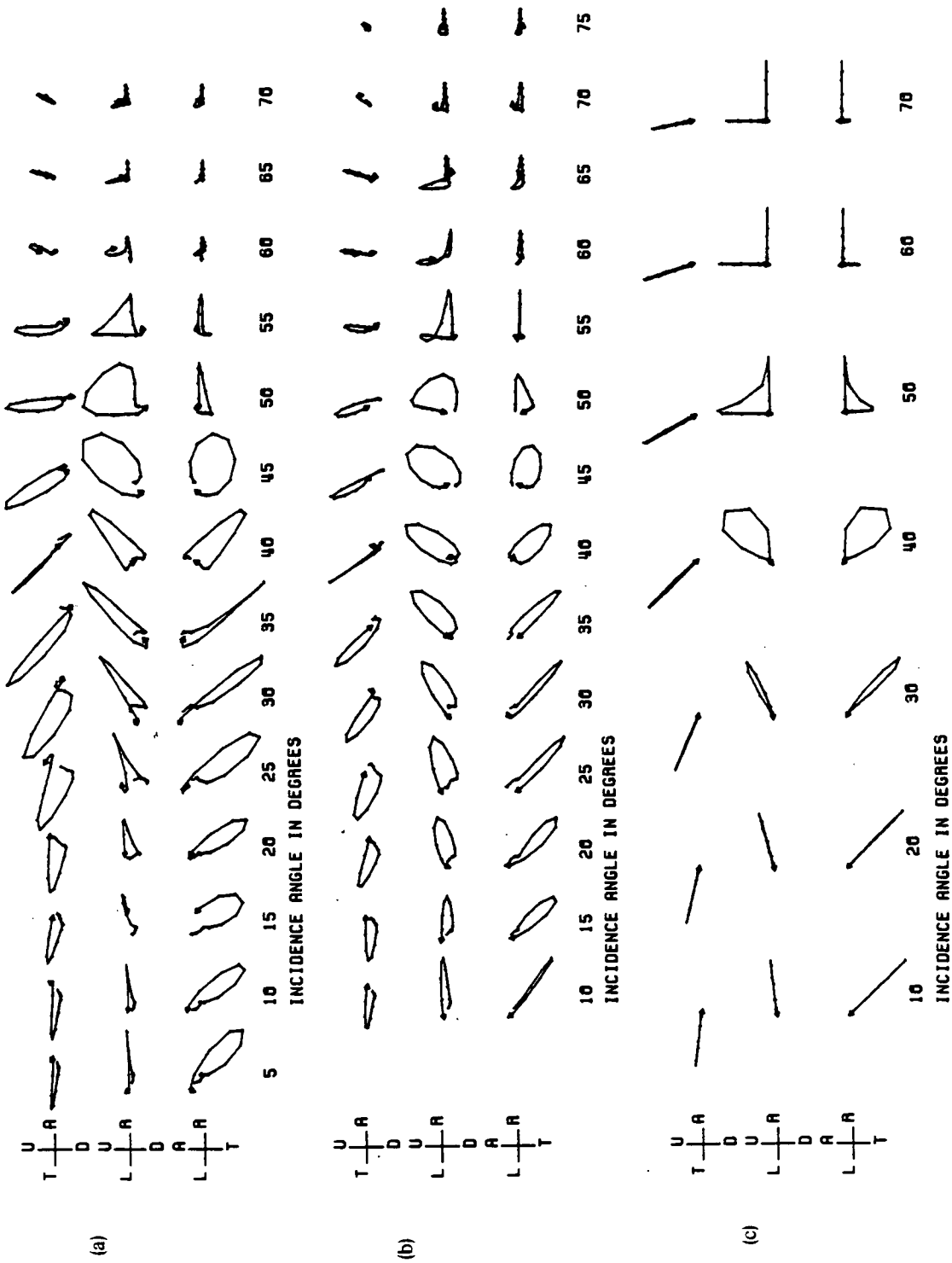
(a)
(b)
(c)
TRAD
LUAD
LAAT
5 10 15 20 25 30 35 40 45 50 55 60 65 70
10 15 20 25 30 35 40 45 50 55 60 65 70 75
10 20 30 40 50 60 70
INCIDENCE ANGLE IN DEGREES

2.4.2 SV polarization anomalies

The particle motions in Fig. 2.6 are of the components of particle displacement parallel ('P') and perpendicular ('SV') to the straight-ray direction in the vertical plane, of the SV arrival from radial baseplate motion. The deviation of SV polarization from normal to the straight-ray direction is seen as an inclination of the main SV motion from parallel to the 'SV' axis. The deviation increases with increasing incidence angle. At low incidence angles the motions are made triangular by noise slightly before the main SV arrival, which is probably due to the cross-correlation process failing to simulate perfectly a single pulse from the vibrator signal.

2.5 Comparison with theory

We compared the results with theoretical variations of wave velocity, polarization angle and group-velocity deviation angle in the shale at Sulphur Springs. Velocities, polarization angles and group-velocity deviation angles were computed from the elastic constants of the shale using the formulae of Crampin (1981). The elastic constants used are listed in Table 2.2; these are not exactly the constants determined by Robertson and Corrigan (1983, Table 2), because theoretical velocities derived from those constants do not fit our observed velocities. We did not have accurate values of the velocities shown in Fig. 12 of Robertson and Corrigan (1983), from which their elastic constants are derived. We also lacked the P-wave velocities used to derive constants A and C, so we adjusted the constants F, L and N by trial and error to fit a group-velocity surface to our observed velocities, leaving A

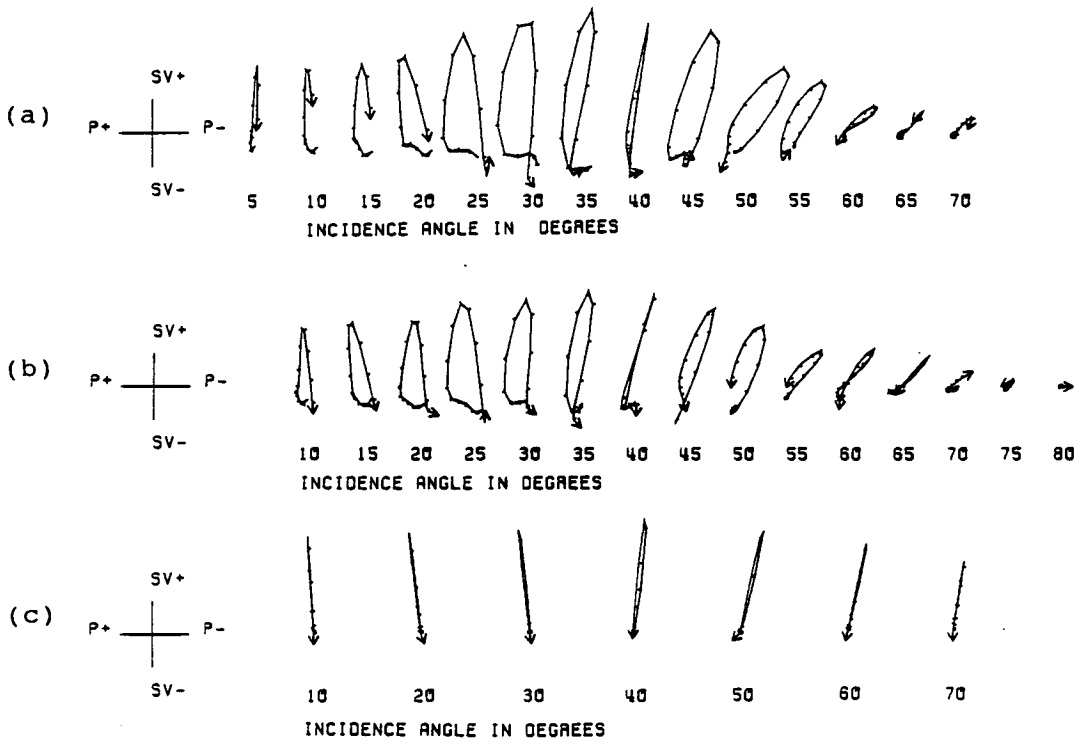

Fig. 2.6 'P'- and 'SV'-component polarization diagrams from shots with the baseplate radial. (a) East line. (b) North line. (c) Synthetic. Following Robertson and Corrigan, axis labels P+ and P- represent motion towards and away from the geophone, respectively, along the straight ray path between shot and geophone. SV represents motion perpendicular to the straight ray path in the vertical plane; SV+ is upward and SV- is downward.

Table 2.2

Elastic constants of the Sulphur Springs shale

density=1.8g/cm^3

		elastic constants (units 10^9N/m^2) original value	new value
c_{1111}	A	3.52	3.52
c_{3333}	C	2.02	2.02
c_{1133}	F	2.03	2.02
c_{1313}	L	0.27	0.26
c_{1212}	N	0.42	0.51

and C alone. The result is shown in Fig. 2.7. Velocities derived from the original constants of Robertson and Corrigan are shown in Fig. 2.8 for comparison.

The chosen group-velocity surfaces fit the observations up to 60° incidence angle: at greater incidence angles the observations are clearly affected by an increase in velocity with depth, possibly accompanied by a change in anisotropic properties, which invalidates the straight-ray assumption. A better fit of the theoretical group-velocity surface to the high incidence-angle velocities would be to the detriment of the fit to the lower incidence-angle velocities.

2.5.1 Velocities

The theoretical shear-wave phase and group velocities at Sulphur Springs, calculated from the elastic constants in Table 2.2, are shown in Fig. 2.9. Note that the velocity variations have been plotted against the incidence angle of the group velocity, since this angle can be equated with the observed straight-ray angle, while it is not possible to observe the incidence angle of the phase velocity with the single geophone. The velocity variation is that of a medium with hexagonal symmetry, with the slow direction for SH waves parallel to the symmetry axis (vertical), and a line singularity (Crampin 1981) at 45° (35° for the group velocities).

The delay between the two split shear waves increases with increasing incidence angle, as seen in Fig. 2.5, because both the path length through the shale and the difference between the SH- and SV-wave velocities increase with incidence angle. The increase in velocity with depth, which affects the observed

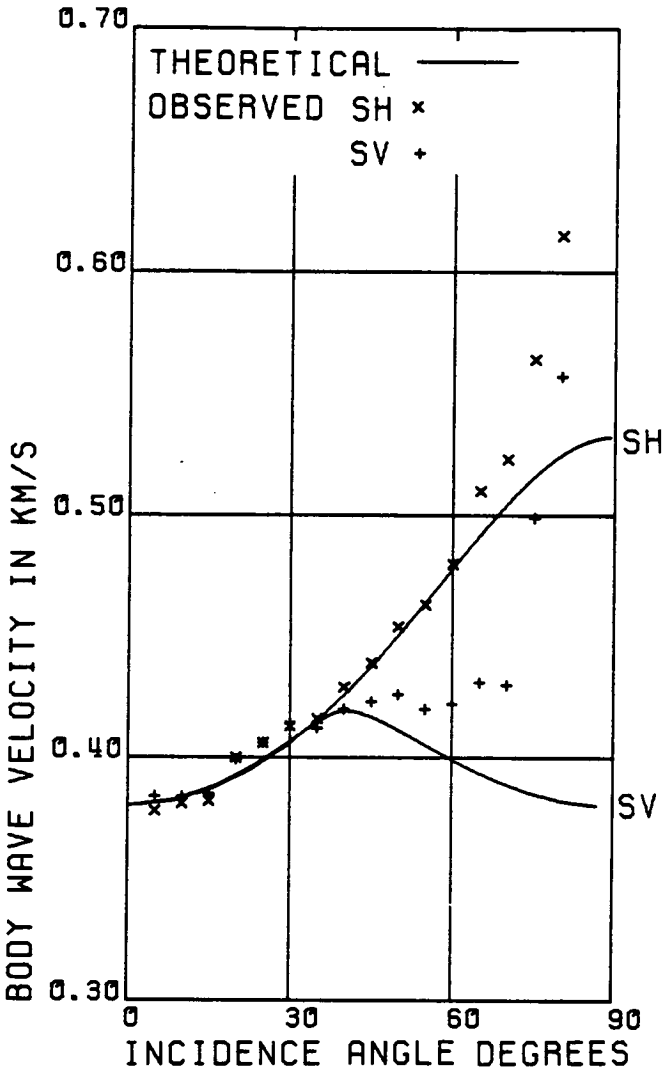

Fig. 2.7 Theoretical group velocities at Sulphur Springs, calculated from the new elastic constants listed in Table 2.2; and observed velocities, plotted at the group-velocity incidence angle.

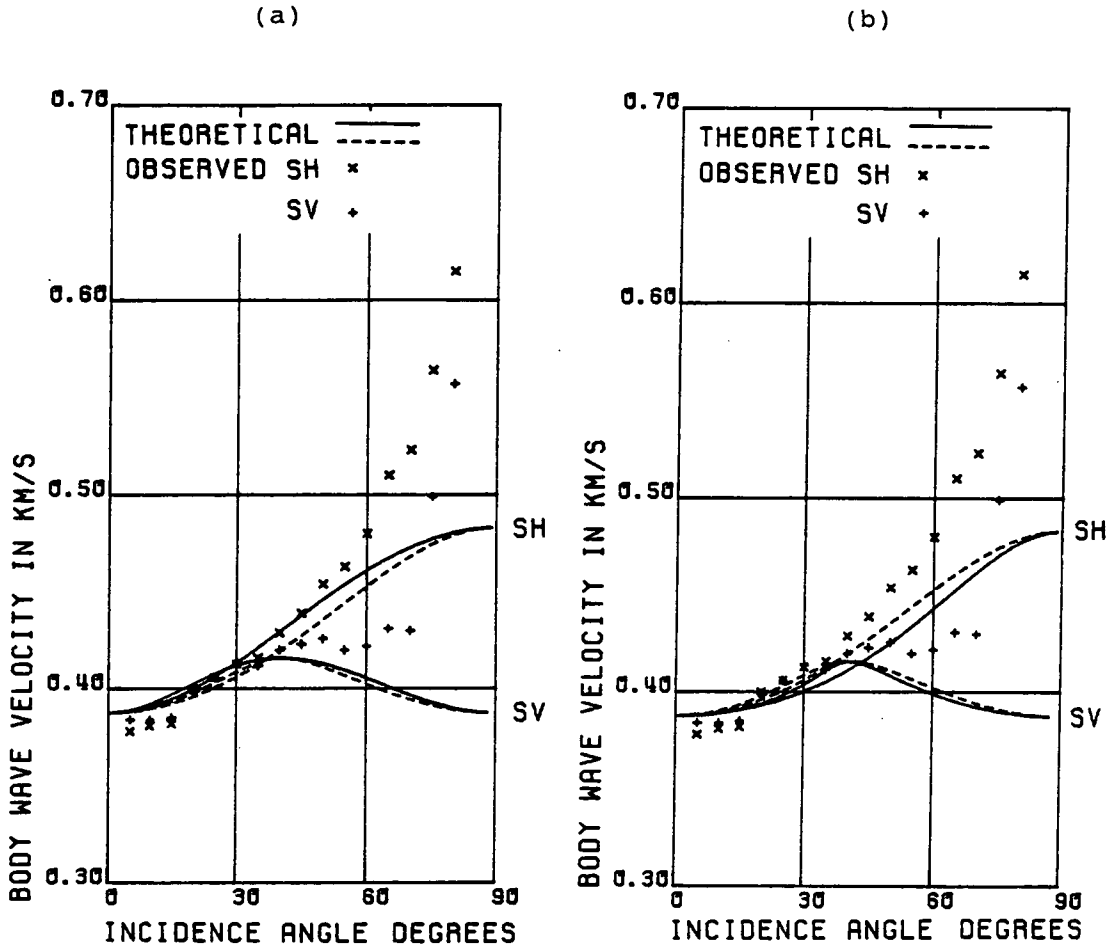

Fig. 2.8 Theoretical phase and group velocities calculated from the elastic constants of Robertson and Corrigan (1983) (Table 2.2), and observed group velocities, plotted against (a) phase-velocity incidence angle; (b) group-velocity incidence angle. Solid line - phase velocity; dashed line - group velocity.

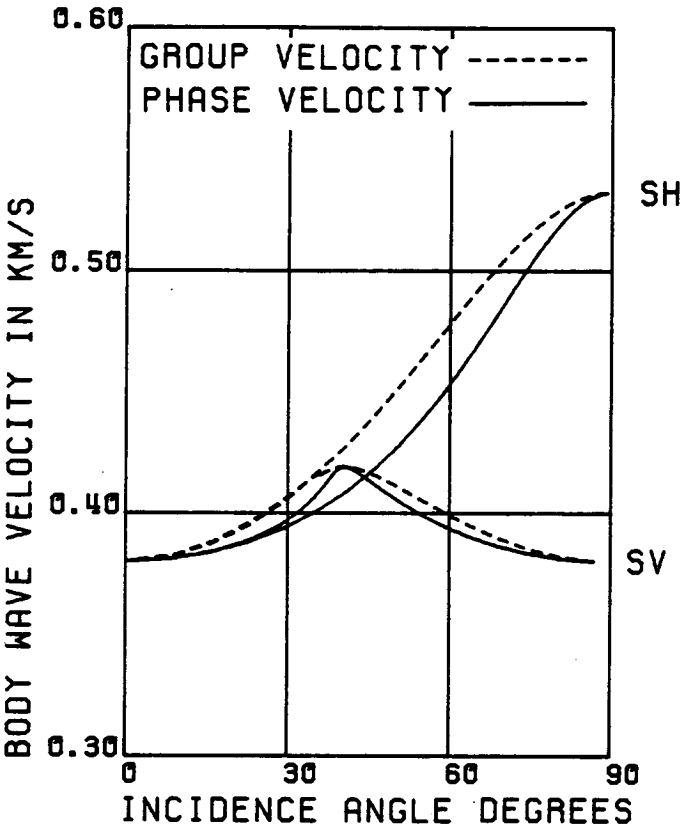

Fig. 2.9 Variation of shear-wave phase and group velocity with group-velocity incidence angle in the Sulphur Springs shale, calculated from the new elastic constants in Table 2.2.

velocities at large straight-ray incidence angles in Fig. 2.7, should add to the increase in delay between the split shear waves by causing the raypath to curve and thus making the true incidence angle closer to horizontal than the straight-ray angle. In fact the difference between the SH and SV observed velocities decreases at the highest straight-ray incidence angles (75° and 80°), suggesting that either the degree of anisotropy of the shale decreases with depth or the raypath has dived below the level of the geophone and has a true incidence angle substantially greater than 90°. Compaction of the shale at depth may reduce the pore space between bedding planes, reducing its contribution to the anisotropy. The possibility of diving rays will be considered in the next section.

2.5.2 Polarization angles

Fig. 2.10(a) shows the deviation of the phase-velocity vectors of the three body waves from the group-velocity direction, as a function of group-velocity incidence angle. The sign convention is that the deviation is positive when the phase-velocity incidence angle is greater than the group-velocity incidence angle. P and SH phase-velocity incidence angles are consistently less than the group-velocity incidence angle, but the SV phase-velocity incidence angle switches abruptly at 40° from being less to being greater than the group-velocity incidence angle.

Fig. 2.10(b) shows the angles between polarization and the phase- and group-velocity directions of SV waves. The angle between the polarization and group velocity is the one that we can observe at the geophone. For SV waves at high incidence angles it

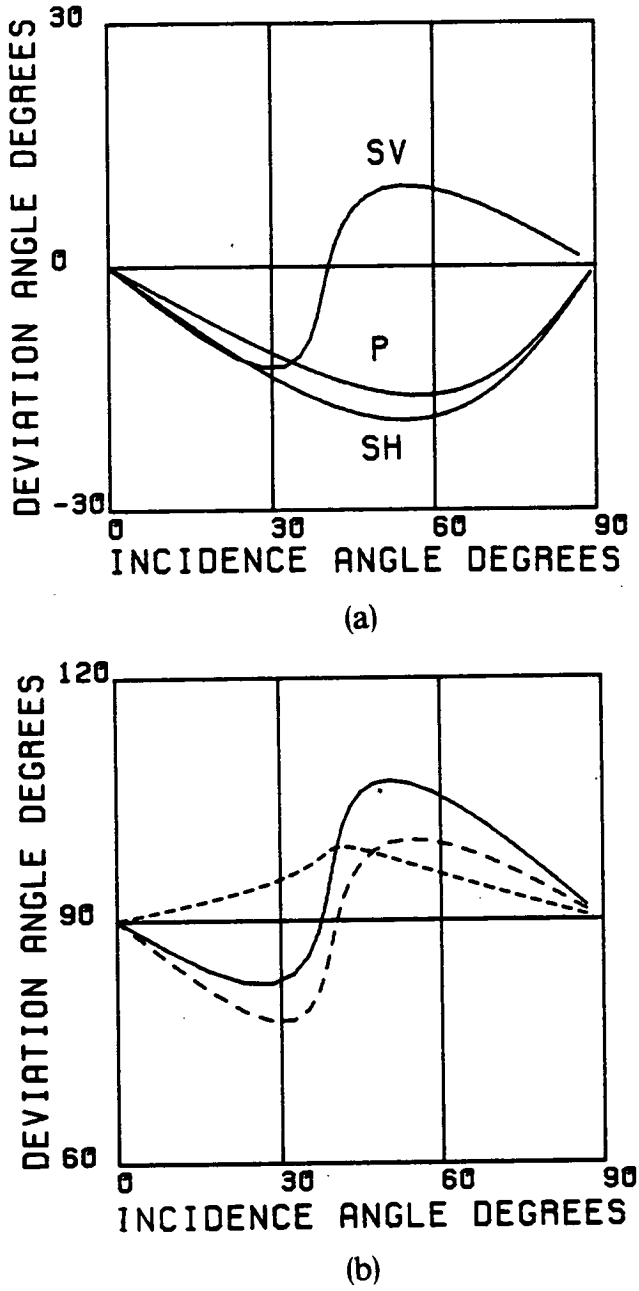

Fig. 2.10 Variation of calculated deviation angles with group-velocity incidence angle in the Sulphur Springs shale (new elastic constants). (a) Deviation of P, SH, and SV phase velocities from the group-velocity direction. (b) angle between SV-wave phase-velocity direction and polarization (short dash); angle between group- and phase-velocity directions, as in (a) (long dash); and resultant angle between polarization and group-velocity direction (solid line).

is large, up to 15° at incidence angle 50°. In Fig. 2.11 the theoretical angle between SV polarization and group velocity is compared with the measured angles between SV polarization and the straight-ray direction (data from Table 2.1). The observed and theoretical values agree for incidence angles less than 45°, suggesting that the raypaths at these incidence angles are not refracted by an increase in velocity with depth. At higher incidence angles the theoretical angle is decreasing but the observed angle continues to increase, indicating that an increase in velocity with depth is causing the raypaths to curve so that the group-velocity incidence angle is greater than the straight-ray angle. At the maximum incidence angle, 80°, the theoretical angle between the polarization and group-velocity directions is 99°, while the observed angle between the straight-ray and SV polarization is 140°. The true incidence angle of the group velocity is therefore approximately 121°: which supports the suggestion in the previous section that the ray has dived below the level of the geophone. The true group-velocity incidence angles of the diving rays may be larger than the values given in Table 2.1 for straight-ray incidence angles greater than 55° since at incidence angles between 90° and 140° the normal to the SV polarization deviates from the group-velocity direction towards 90°.

2.6 Synthetic seismograms

The simple arrangement of source, medium and geophone in the experiments of Robertson and Corrigan (1983) is well-suited to modelling with synthetic seismograms. We used the program

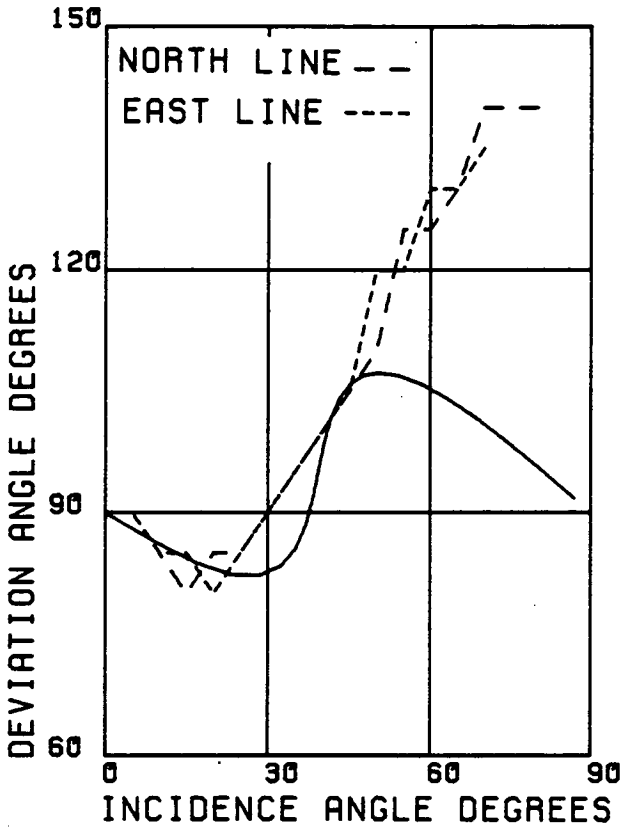

Fig. 2.11 Observed angle between SV polarization and straight-ray direction at Sulphur Springs (dashed lines), superimposed on the theoretical, anisotropy-induced variation of the angle between SV polarization and group-velocity direction, as in Fig. 2.8(b) (solid line).

described in Keith and Crampin (1977a, b, c) which synthesizes a plane wave passing through a set of isotropic and anisotropic plane layers between two isotropic half-spaces. Plane waves of frequency 14 Hz were incident on the upper boundary and the program calculated the signal received at the lower boundary.

The model of the Sulphur Springs experiment consisted of a single anisotropic layer, with the density and elastic constants given in Table 2.2, between two half-spaces with shear-wave velocities equal to the lowest velocity of shear waves in the anisotropic layer (380 m/s). We synthesized the signal from the radial baseplate with a pure plane SV wave incident on the model layer, and the transverse baseplate signal with a pure SH wave. The baseplate at 45° was simulated in the same way as for the real data, by vector addition of the output signals from input SH and input SV waves. The approximation of the vibrator signal by a plane wave is reasonable since the path is through a single homogeneous medium and the geophone is beneath the surface (which has different effects on plane and curved wavefronts - Booth and Crampin 1985), and the shortest path length (53 m) is greater than one wavelength (27 m for 14 Hz waves).

We simulated the varying incidence angles in the real experiment by altering the orientation of the anisotropic symmetry axis within the layer, rather than by altering the incidence angle of the plane waves on the layer, to avoid mode conversions of waves incident at oblique angles on the interfaces. Mode conversions are unwanted since there are no interfaces between the source and geophone in the real experiment, and the reaction of the synthetic plane wavefront to an oblique interface would be different from the

reaction of the real curved wavefront.

The orientation of the symmetry axis was chosen to give group-velocity incidence angles equal to the straight-ray incidence angles in the real experiment. The deviation of phase velocity from group velocity is different for SH and SV waves (Fig. 2.10a), so SH and SV waves with the same group-velocity direction have different phase-velocity directions. Since the program requires that the phase-velocity direction be specified, we used the deviation angles plotted in Fig. 2.10(a) to determine the SH and SV phase-velocity directions corresponding to each group-velocity incidence angle. Fig. 2.12 shows the relation of the synthetic model to the real experiment. We simulated the change in travel path length with incidence angle in the real experiment by altering the thickness of the anisotropic layer. The appropriate thickness for SH waves was different from that for SV waves because the plane-wave signal input of the synthetic seismogram travels at the phase velocity. The real straight-ray path in Fig. 2.12 has length $l = h/\cos\theta$; the phase-velocity paths have length $l \cos\alpha$ where α is the deviation of phase from group velocity.

Synthetic seismograms using this model are superimposed on the real cross-correlograms from the Sulphur Springs North line shots in Fig. 2.13. Since the real arrival is at the peak of the cross-correlogram, the start time of the synthetic seismogram has been taken at the peak of the input pulse.

At low incidence angles the synthetic seismograms agree with the real ones, exactly as expected from Fig. 2.7. At higher incidence angles (greater than 60°) the real arrival is before the synthetic, because the synthetic model does not allow for the

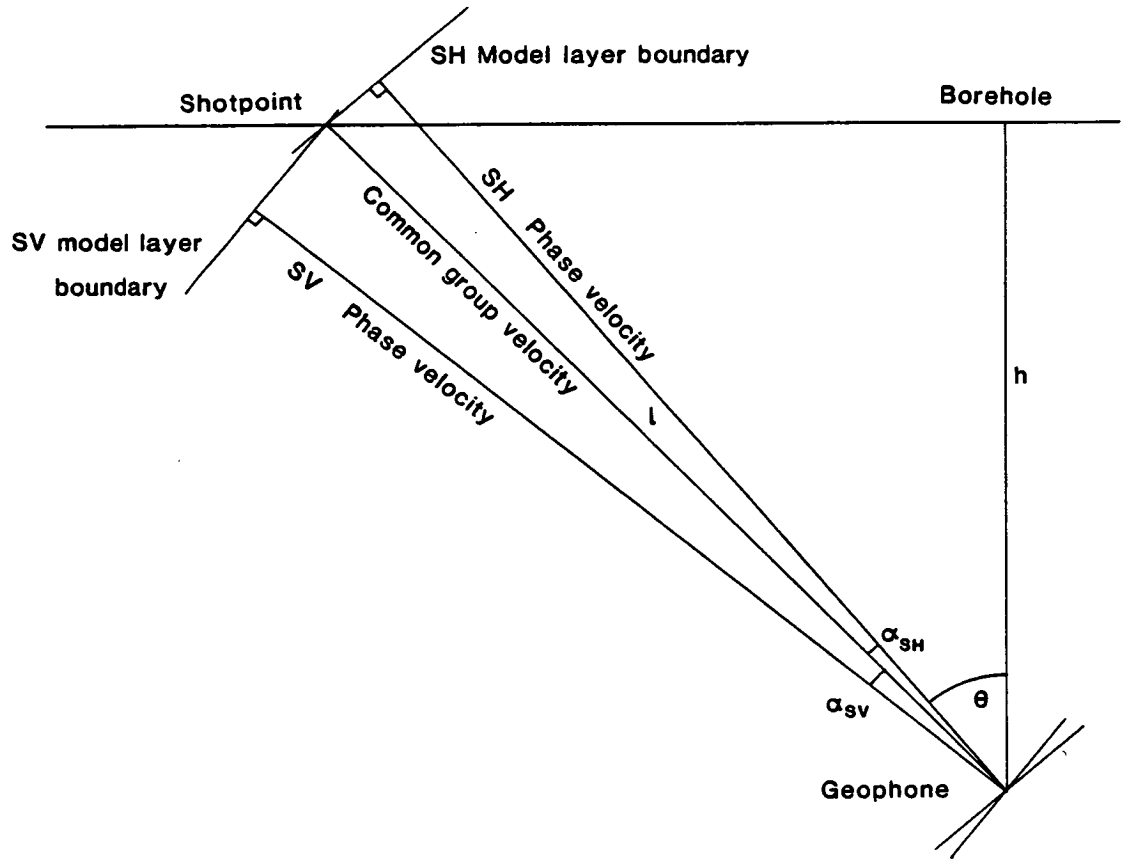

Fig. 2.12 Schematic diagram showing relationship of synthetic seismogram models to the real experiment.

Fig. 2.13 Synthetic seismograms of SH, SV, and mixed polarity shear waves passing through the Sulphur Springs shale (dashed lines) compared with the real seismograms (solid lines) from the North shot line (as in Fig. 2.4) at every ten degrees of incidence angle.

Fig. 2.13

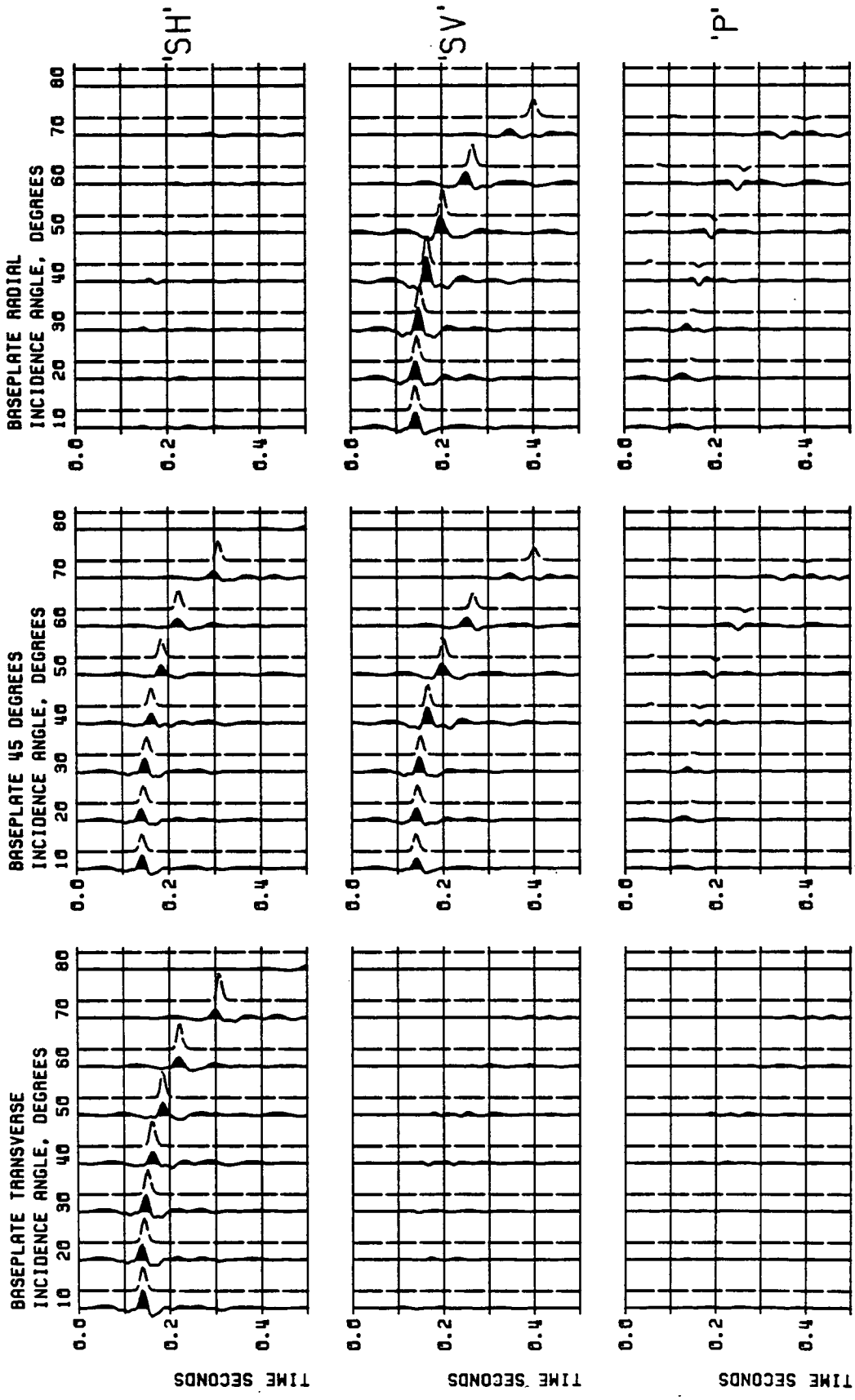
'SH'
'SV'
'P'
BASEPLATE RADIAL
INCIDENCE ANGLE, DEGREES
BASEPLATE 45 DEGREES
INCIDENCE ANGLE, DEGREES
BASEPLATE TRANSVERSE
INCIDENCE ANGLE, DEGREES
10 20 30 40 50 60 70 80
0.0 0.2 0.4
TIME SECONDS

increase in velocity with depth in the real shale.

Particle motions from the synthetic shots with "baseplate 45°" are in Fig. 2.5(c). They show the same increase in the degree of shear-wave splitting with increasing incidence angle as the real seismograms.

Fig. 2.6(c) shows polarization diagrams of the 'SV' and 'P' components of the synthetic seismogram from an input SV wave. As in Fig. 2.6(a) and (b), the inclination of the traces from parallel to the 'SV' axis is the measure of the deviation of SV-wave polarization from perpendicular to the group velocity. The inclination is not as great as in the plots of real data from Sulphur Springs in Fig. 2.6(a) and (b), again because the synthetic seismogram model does not include any increase in velocity with depth in the real shale. The deviations of the synthetic polarizations in Fig. 2.6(c) match the calculated deviation of polarization from group velocity in Fig. 2.10(b).

2.7 Conclusions

We have simulated records of mixed-polarity shear waves propagating through transversely isotropic shale, and shown that shear-wave splitting, a crucial indicator of anisotropy, is clearly seen when the results are presented as polarization diagrams. The experiments of Robertson and Corrigan (1983) show that a shear-wave vibrator is a well-determined and repeatable source of shear waves. We suggest that one shot with the mixed-polarity signal from a shear-wave vibrator oriented neither radial nor transverse to the shot-receiver line reveals as much information about the anisotropy of the rocks along the raypath as two shots with the vibrator

radial and transverse to the shot line.

Although transverse isotropy with a vertical symmetry axis is mathematically closer to isotropy than to more general anisotropy (Crampin 1986b), its effects on shear-wave velocities and polarizations can be misleading if interpreted using an isotropic model. We have shown that the deviation of SV polarization from normal to the group-velocity direction can be misinterpreted as refraction due to an increase in velocity with depth. Comparison with calculated polarization angles for the Sulphur Springs shale showed that the observed polarization anomaly was entirely caused by anisotropy up to incidence angles of 45°, and that anisotropy had an appreciable effect at greater incidence angles.

The synthetic seismograms model both the shear-wave splitting and SV polarization anomalies caused by the anisotropic shale. This is probably the first time that detailed observations of particle motion in a transversely isotropic medium, in either laboratory or field, have been modelled by synthetic seismograms. The phase and group velocities, the polarizations and the shear-wave splitting of the synthetic seismograms all agree remarkably well with the real data, and give a valuable test of theoretical ideas. The success of the modelling here was due to the wave velocities being measured for a wide range of incidence angles, allowing accurate determination of elastic constants. Determination of elastic constants by trial-and-error fitting of group-velocity surfaces to observations would have been more difficult if there had been cusps on the group-velocity surface (Crampin 1981).

Shales, mudstones and other fine-grained sediments, and periodic thin layering of contrasting sediments (Crampin *et al.* 1984a), which show transverse isotropy, are common in the ancient marine deposits where oil is found; and recent ideas that more general anisotropy caused by aligned cracks and microcracks is widespread in all rock types (Crampin and Atkinson 1985) have been borne out by shear-wave vibrator experiments in the Paris Basin (Crampin and Bush 1986; Crampin *et al.* 1986c) and elsewhere. It seems that interpretation of seismic records, especially shear-wave records, should proceed from an assumption of general anisotropy, and be supported by synthetic seismograms that match every detail of the observed shear-wave particle motion.

CHAPTER 3

Shear-wave splitting in the aftershock zone of the 1984 North Wales earthquake

3.1 Introduction

Stress fields in the Earth's crust cause alignment of the fluid-filled cracks, microcracks and pores which apparently pervade crustal rocks at all depths (Simmons and Richter 1976; Gold and Soter 1980; Crampin *et al.* 1980; Crampin 1985b: see Chapter 1). These stress-aligned cracks throughout the crust are called extensive-dilatancy anisotropy or EDA (Crampin 1986a). Fluid-filled cracks and microcracks are generally aligned vertically parallel to the direction of maximum deviatoric compression (Crampin 1978), probably by the mechanisms of subcritical crack growth by means of stress corrosion at crack tips (Atkinson 1982, 1984) and elastic "bowing" of the walls of favourably oriented cracks (Crampin *et al.* 1984b). The cracked rocks show effective seismic anisotropy with hexagonal (cylindrical) symmetry about a horizontal axis normal to the crack faces (Crampin 1978). Shear waves propagating through these distributions of aligned cracks are split into two or more components with different velocities and polarizations aligned by the anisotropy (Crampin 1978, 1984b). The horizontal polarizations of faster and slower split shear waves propagating through vertical parallel microcracks striking east-west are shown in Fig. 3.1 (Crampin 1984b).

Analysis of shear-wave polarizations recorded at the free surface is restricted to arrivals within the "shear-wave window",

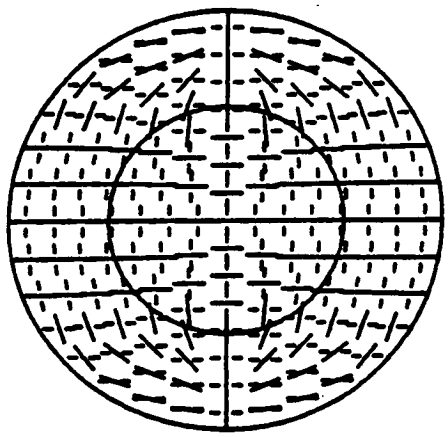

Fig. 3.1 Horizontal equal-area projection out to 90° of theoretical polarizations of split shear wave components after passing through a medium with cracks striking east-west. The unbroken bar is the polarization of the first-arriving component; the broken bar is the polarization of the second (slower) component. The inner circle marks 45° incidence angle.

the area above the source within which shear waves are incident at the surface at less than a critical angle arcsin V_S/V_P (Nuttli 1961; Evans 1984a - see Chapter 1). The polarizations of shear waves incident at greater angles are severely disturbed by the free surface. For Poisson's ratio 0.25 the critical angle is about 35°, but curved wavefronts may be incident at slightly greater angles before being affected by the free surface (Booth and Crampin 1985). The shear-wave window is not generally a well-defined circle since topography and low-velocity or anisotropic surface layers may alter the angle of incidence (Crampin *et al.* 1985). The inner circle in Fig. 3.1 is at 45° incidence angle: polarizations of leading split shear-wave arrivals within this circle, and therefore within the shear-wave window, are almost uniformly parallel to the strike of the aligned cracks. Booth *et al.* (1986) show that cracks dipping at small angles to the vertical show a similar distribution of polarizations within the shear-wave window.

EDA was first invoked to explain aligned shear-wave polarizations from the Turkish Dilatancy Projects (TDP) in the Izmit seismic gap on the North Anatolian Fault, Turkey (Crampin *et al.* 1980, 1985; Booth *et al.* 1985; Crampin and Booth 1985), where shear-wave splitting was observed in experiments designed to test the idea of Crampin (1978) that aligned cracks opened by high stress cause the observed velocity and V_P/V_S changes before large earthquakes (summarized by Rikitake 1976). As subcritical crack growth can occur at stress intensities two or more orders of magnitude lower than that required to create new fractures (Atkinson 1984), EDA should not be restricted to the immediate vicinity of high stress concentrations on fault zones. The uniform

alignments of shear-wave polarizations at all but one of the TDP stations, which are apparently unaffected by marked differences in topography and geology among the sites (Crampin *et al.* 1985), suggest that the alignment of cracks by stress is invariant over large volumes of rock and that shear-wave polarizations are a stable means of detecting crack alignment (Crampin 1985a).

Similar observations of shear-wave splitting around active fault zones in Garm, Tadzhikistan, USSR (Crampin *et al.* 1986a); the Charlevoix seismic zone, Quebec (Buchbinder 1985); several areas in Japan (Kaneshima *et al.* 1986a, b); and around the San Jacinto Fault, Southern California (Peacock *et al.* 1986: see Chapter 4) have since been interpreted as being due to EDA affecting large volumes of rock around the fault zone. Crampin *et al.* (1980, 1984b) suggest that changes in stress intensity or orientation could cause detectable changes in crack geometry, and evidence for such changes has been found in Southern California (Peacock *et al.* 1986: see Chapter 4) and in the TDP study area (Chen *et al.* 1986).

Evidence that intraplate stress fields may also cause EDA has come from beneath Mount Hood, Oregon, USA (Kohler *et al.* 1982; Crampin *et al.* 1986b); at the site of the hot-dry-rock geothermal project in Cornwall (Roberts and Crampin 1986); and in sediments in the Paris Basin (Crampin & Bush 1986; Crampin *et al.* 1986c).

In this chapter we investigate anisotropy in the crust of the Lleyn Peninsula, North Wales, using shear waves from aftershocks of the 1984 North Wales earthquake, a rare intraplate event in an area of low seismicity (Turbitt *et al.* 1985). We look for evidence of microcracks aligned in the regional stress field, and for any changes in crack geometry (Crampin *et al.* 1980, 1984b) that could be

caused by adjustment of the hypocentral zone to the abrupt release of stress at the mainshock.

3.2 The North Wales earthquake and aftershocks

The 5.4 M_L (5.2 m_b) North Wales earthquake is one of the largest to have occurred on the British mainland in the past 100 years (Turbitt *et al.* 1985), and was felt in Wales, much of England, and parts of Scotland and Ireland. A hypocentre below the Lleyn Peninsula was determined by Turbitt *et al.* (1985) and more precisely by Ansell *et al.* (1986) at 52° 57.5' N, 4° 23.9' W, depth 22.8 km.

3.2.1 Aftershock recording and location

A temporary network of 16 seismic stations was set up by the British Geological Survey (BGS) around the epicentre to record the aftershock sequence (Fig. 3.2) and during a year of operation recorded over 300 aftershocks (Turbitt *et al.* 1985; Marrow and Walker 1986; Browitt *et al.* 1985). The stations consisted of Willmore Mark III seismometers in concrete-floored pits, resting on bedrock where possible. The seismometers were linked by land line or UHF radio to three base stations, where the signals were recorded on analogue tape. At the recording speed of 15/160 inches per second (ips) the system response is flat to velocity between 2 and 26 Hz (Turbitt and Stewart 1982). The frequencies of shear waves from the aftershocks were around 8-24 Hz.

The aftershocks were located by BGS staff using HYPO71 (Lee and Lahr 1975) with a velocity model adapted from the northern end of the LISP-B Delta seismic refraction line (Table 3.1) (Edwards and Blundell 1984). The small RMS errors in the locations, which

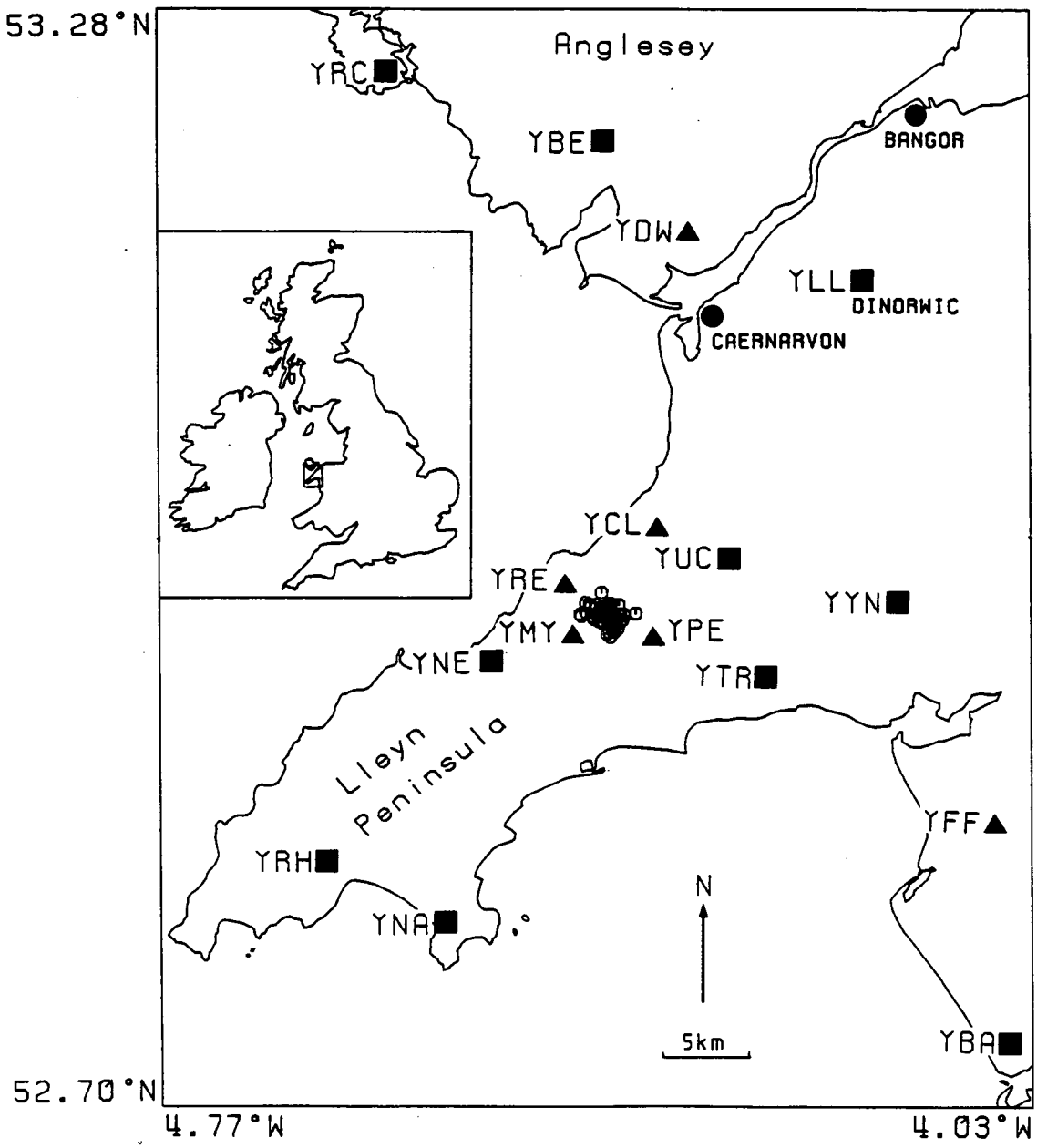

Fig. 3.2 Map of the Lleyn peninsula and part of Anglesey, showing the BGS seismic network. Triangles - three-component stations; squares - vertical component stations; open circles - epicentres of aftershocks. The inset shows the location of the Lleyn Peninsula in the British Isles.

Table 3.1 (a) Velocity model used in hypocentre location.

Layer	P-wave velocity km/s	Depth to top of layer km
1	5.40	0
2	6.05	2
3	6.50	13
4	6.80	25
5	8.00	34

V_p/V_s = 1.68

(b) Station positions

Station	Latitude °N	Longitude °E	Grid East	Grid North	Height m
YNA	52.8010	-4.5283	229.571	325.629	54
YRH	52.8335	-4.6288	222.930	329.500	300
YNE	52.9385	-4.4890	232.756	340.839	192
YBE	53.2137	-4.3897	240.450	371.215	62
YRC	53.2507	-4.5740	228.289	375.745	24
YLL	53.1402	-4.1703	254.842	362.568	162
YUC	52.9948	-4.2878	246.474	346.653	211
YMY	52.9522	-4.4188	237.518	342.200	171
YPE	52.9512	-4.3510	242.068	341.940	195
YTR	52.9308	-4.2535	248.550	339.460	57
YYN	52.9692	-4.1438	256.050	343.500	235
YBA	52.7348	-4.0517	261.496	317.255	250
YFF	52.8537	-4.0605	261.270	330.492	240
YDW	53.1643	-4.3188	245.002	365.571	9
YRE	52.9810	-4.4255	237.186	345.418	197
YCL	53.0088	-4.3493	242.400	348.338	340

Table 3.2 Mean polarizations of shear-wave first arrivals at the four 3-component stations, with standard deviations and mean resultant length (the mean resultant length is a measure of alignment of polarizations in one direction: values near 1 indicate strong unimodal alignment; values near 0 indicate no alignment i.e. a uniform (random) distribution of polarizations).

Station	Number of readings	Mean polarization degrees	Standard deviation degrees	Mean resultant length
YMY	33	109.1	33.0	0.51
YRE	32	146.4	38.5	0.40
YCL	15	90.8	21.4	0.76
YPE	17	13.7	12.7	0.91

increased when the model parameters were perturbed (Marrow and Walker 1986) suggest that the model is appropriate. Location errors are ±1.3 km (Marrow and Walker 1986).

The aftershocks used in the shear-wave analysis are shown in Fig. 3.2. They form a tight cluster at depth 20-25 km. Four of the six three-component stations in the BGS network, YRE, YMY, YCL, and YPE, are within the shear-wave window of the aftershock cluster.

3.2.2 Geological setting

The Lleyn Peninsula is made up mostly of Precambrian and Lower Palaeozoic sedimentary and volcanic rocks, folded and faulted by the Caledonian orogeny and the sediments metamorphosed to slate (Roberts 1979; Tremlett 1962, 1964, 1965). The rocks immediately around the epicentres are Ordovician slates, sandstones and tuffs, intruded by several small igneous bosses (of microgranite, felsite or andesite) of Ordovician or Caledonian age, which form low hills (Fig. 3.3). In most places the bedrock is covered with thick layers of glacial drift. Station YMY is on drift near an outcrop of felsite, and it is not clear whether the underlying rock is slate or felsite (A. Reedman, personal communication; Tremlett 1962; Roberts 1979). Station YRE is on landslide blocks of felsite overlying slate. YCL is on drift overlying slate, and YPE is on a small andesite intrusion (Croudace 1982).

The North Wales earthquake is not associated with a well-defined active fault zone (Turbitt *et al.* 1985; Marrow and Walker 1986). The 20-25 km depth range of the mainshock and aftershock foci is unusual for earthquakes in the continental crust, which are

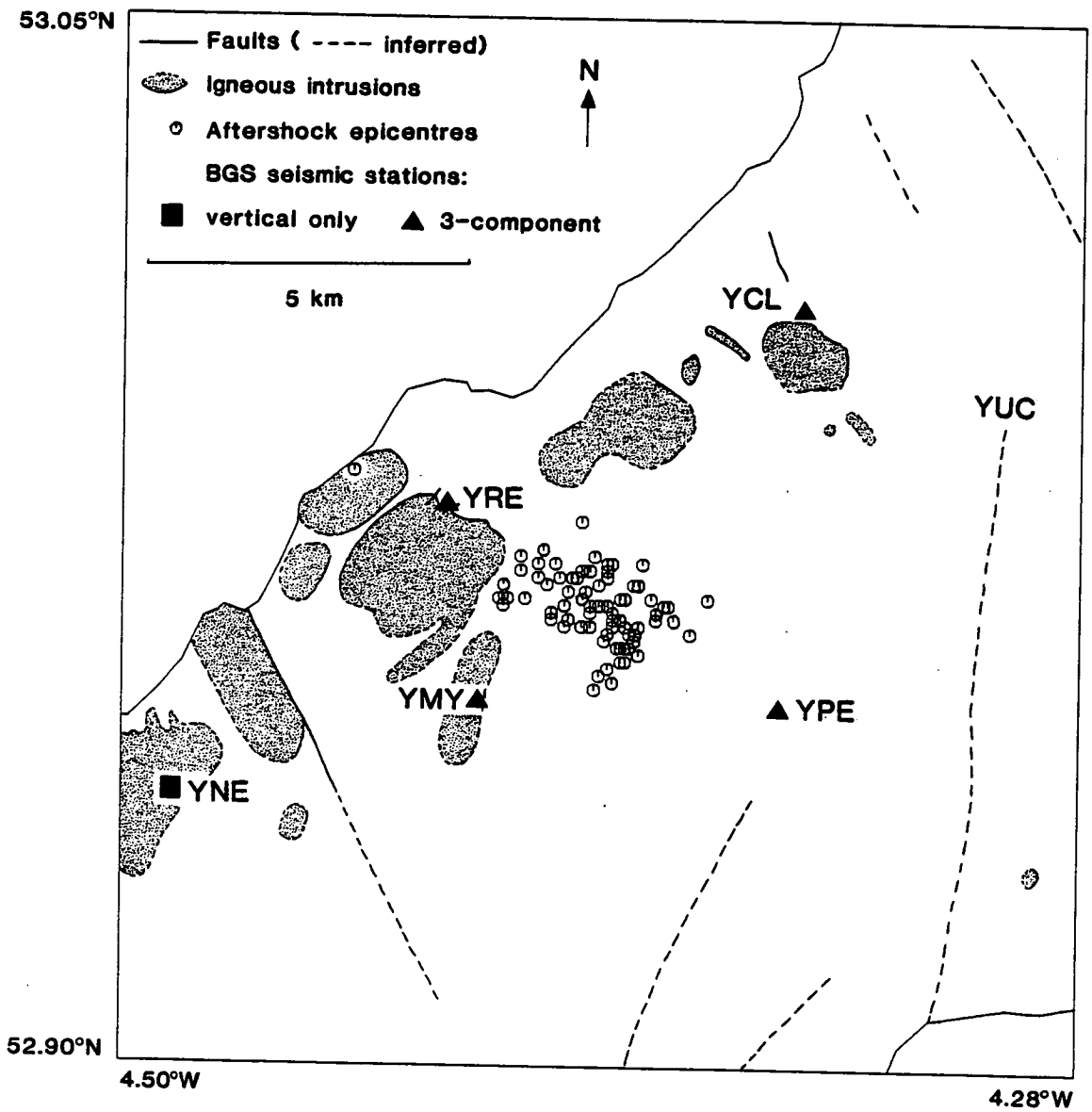

Fig. 3.3 Map of immediate epicentral area, showing geology (simplified from Roberts 1979, with permission), BGS seismic stations, and epicentres of aftershocks used in shear-wave investigation.

generally believed to be concentrated in a brittle-ductile transition zone between 8 and 15 km depth (Evans 1984b). Low heat flow in this area may cause the crust to be brittle and fracture at greater depth (Burley and Edmunds 1978; Ansell *et al.* 1986).

3.3 Results

Analogue records of 74 aftershocks recorded at the four three-component stations within the shear-wave window were digitized at 128 samples per second. Evidence of shear-wave splitting is seen in almost all records, indicating some form of effective anisotropy along the raypaths. The shear-wave arrivals were plotted as polarization diagrams in three mutually orthogonal cross-sections, and the horizontal polarization of the first shear-wave arrival and the time delay between the two split shear-wave arrivals were measured from the horizontal section. Fig. 3.4 shows sample seismograms and polarization diagrams from the four stations.

(There is a distinct contrast in signal frequencies between YRE and the other stations (note the different time scales below the seismograms in Fig. 3.4): the dominant frequency of the shear-wave arrivals at YRE is approximately 8 Hz, while at the other three-component stations it is 11-22 Hz. The site at YRE is presumably acting as a low-pass filter. Polarizations at YRE are clearer after the removal of high frequencies, but delays are sometimes more difficult to measure because the loss of high frequencies "rounds off" the sharp changes in polarization at the arrival of the second shear wave.)

Fig. 3.4 Sample three-component seismograms and polarization diagrams showing shear-wave splitting at (a) station YMY, from an event at depth 22.12 km, distance 1.9 km at azimuth N 38°E from the station; (b) station YRE, from an event at depth 23.44 km, distance 3.8 km at azimuth N 143°E from the station; (c) station YCL, from an event at depth 20.3 km, distance 6.2 km at azimuth N 222°E from the station; (d) station YPE, from an event at depth 23.22 km, distance 2.1 km at azimuth N 326°E from the station. The horizontal components have been rotated to radial and transverse to the epicentre-station line. The polarization diagrams are numbered to correspond to the time intervals marked above the seismograms, which are 0.08 s long for (a) and (d), and 0.15 s long for (b) and (c). Note the different time scales marked beneath each seismogram - 5 seconds for (a) and (d); 6 seconds for (b) and (c). Labels on the polarization diagrams are Up, Down, Towards and Away from the epicentre, and Left and Right when facing away from the epicentre. Ticks on the particle displacements are 1/128 s apart, and a scale factor (x 1, x 2 etc.) is shown above each set of polarization diagrams. Shear-wave splitting is seen in the horizontal plane, where the arrivals of both split shear waves are marked with arrowheads.

Fig. 3.4 (a)

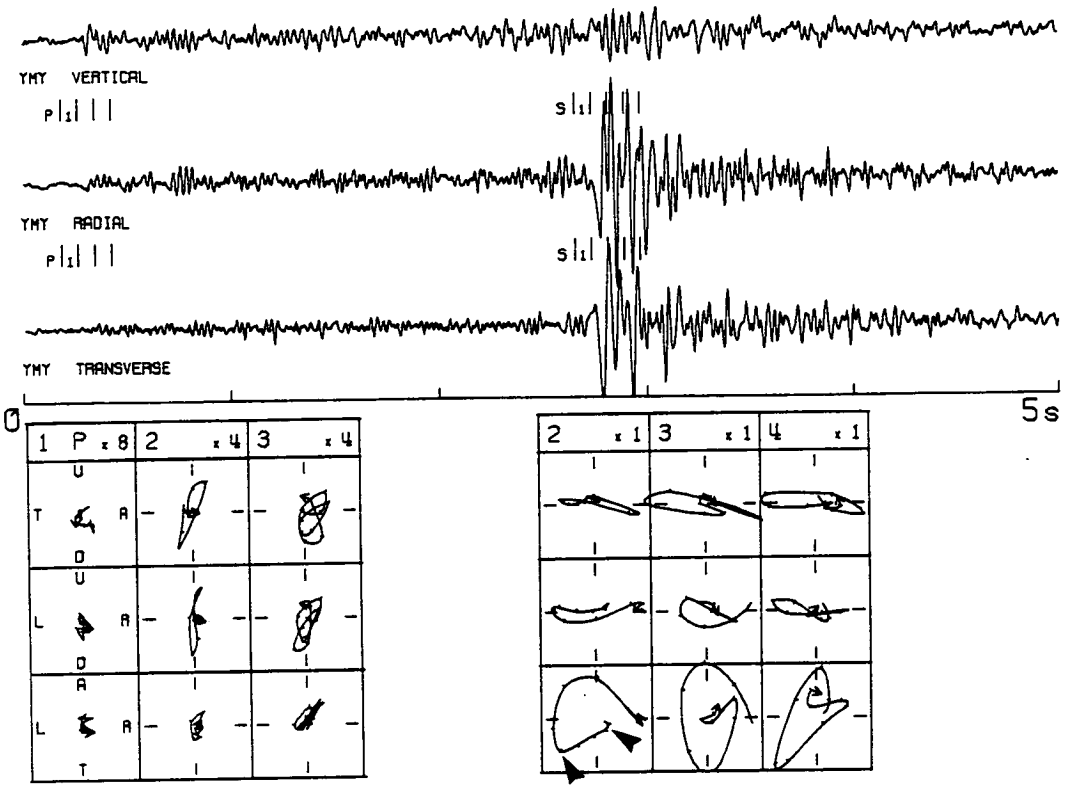
YMY VERTICAL
P
S
YMY RADIAL
P
S
YMY TRANSVERSE
0
5s
1 P x 8
2 x 4
3 x 4
2 x 1
3 x 1
4 x 1
U
D
A
T
L
R

Fig. 3.4 (b)

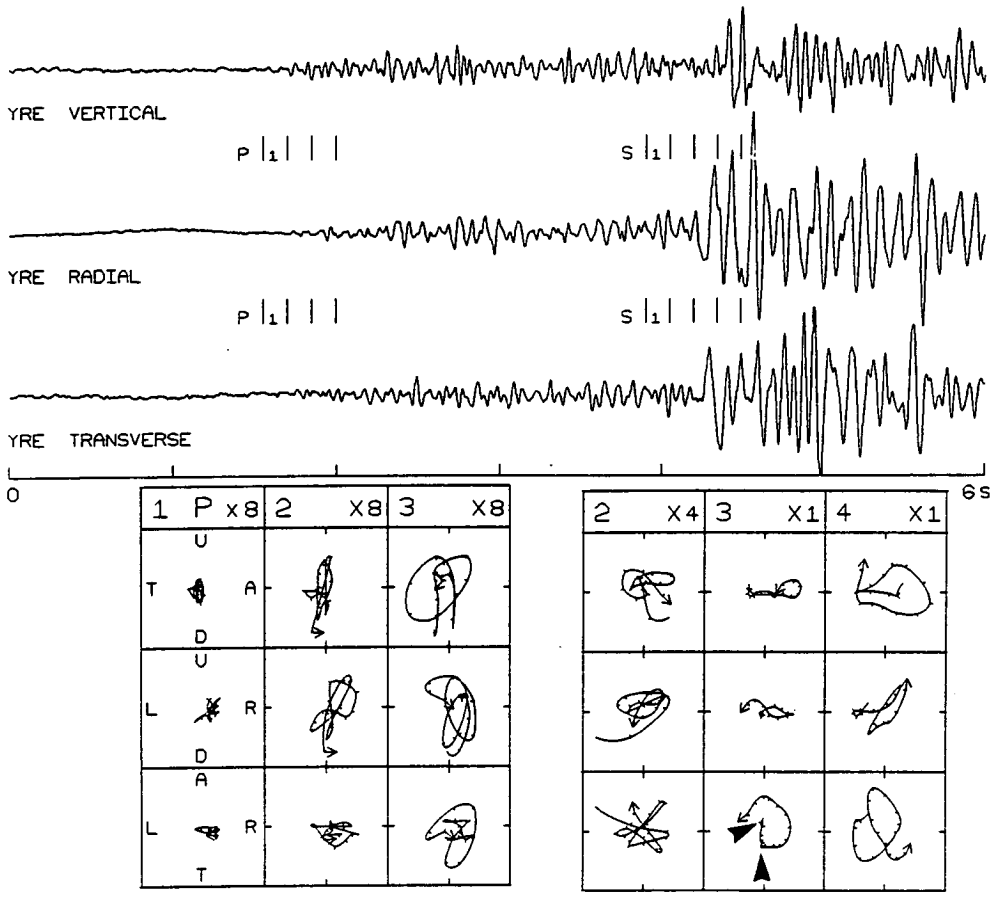
YRE VERTICAL
P
S
YRE RADIAL
P
S
YRE TRANSVERSE
0
6s
1 P x8
2 x8
3 x8
2 x4
3 x1
4 x1
U
T
A
D
L
R
A
T

Fig. 3.4 (c)

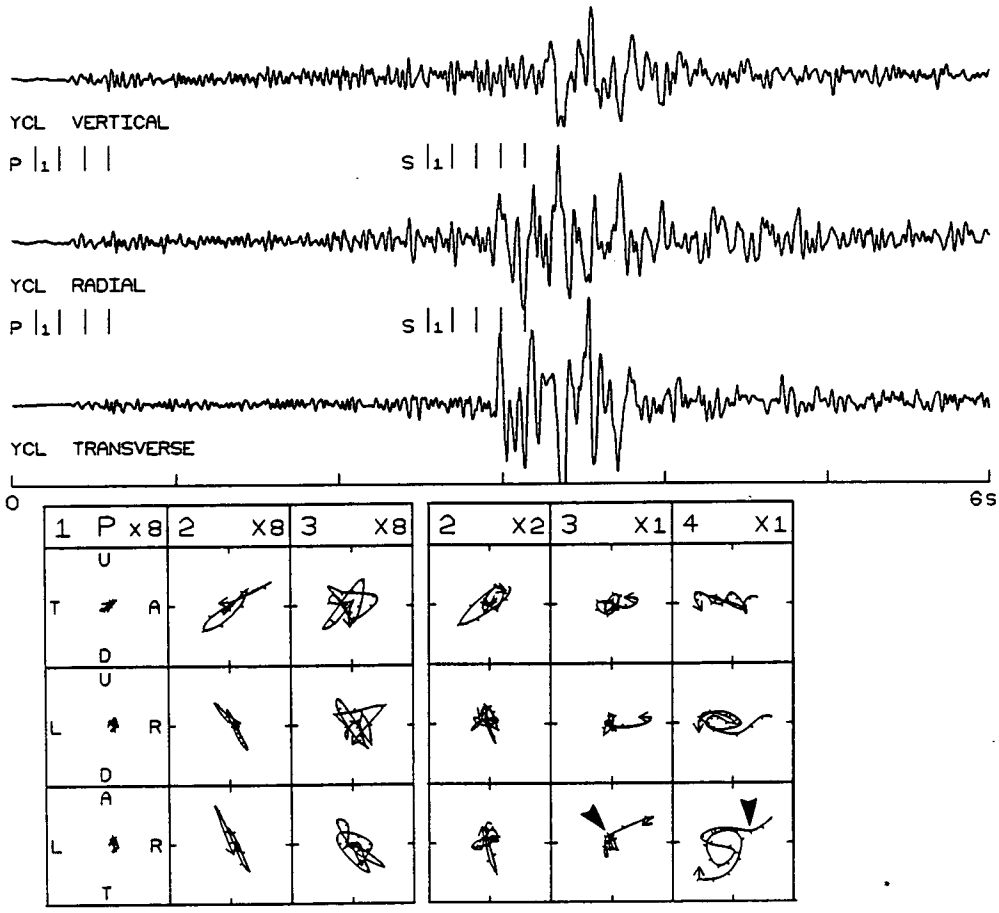
YCL VERTICAL
P
S
YCL RADIAL
P
S
YCL TRANSVERSE
0
6s
1 P x8
2 X8
3 X8
2 X2
3 X1
4 X1
U
T
A
D
U
L
R
D
A
L
R
T

Fig. 3.4 (d)

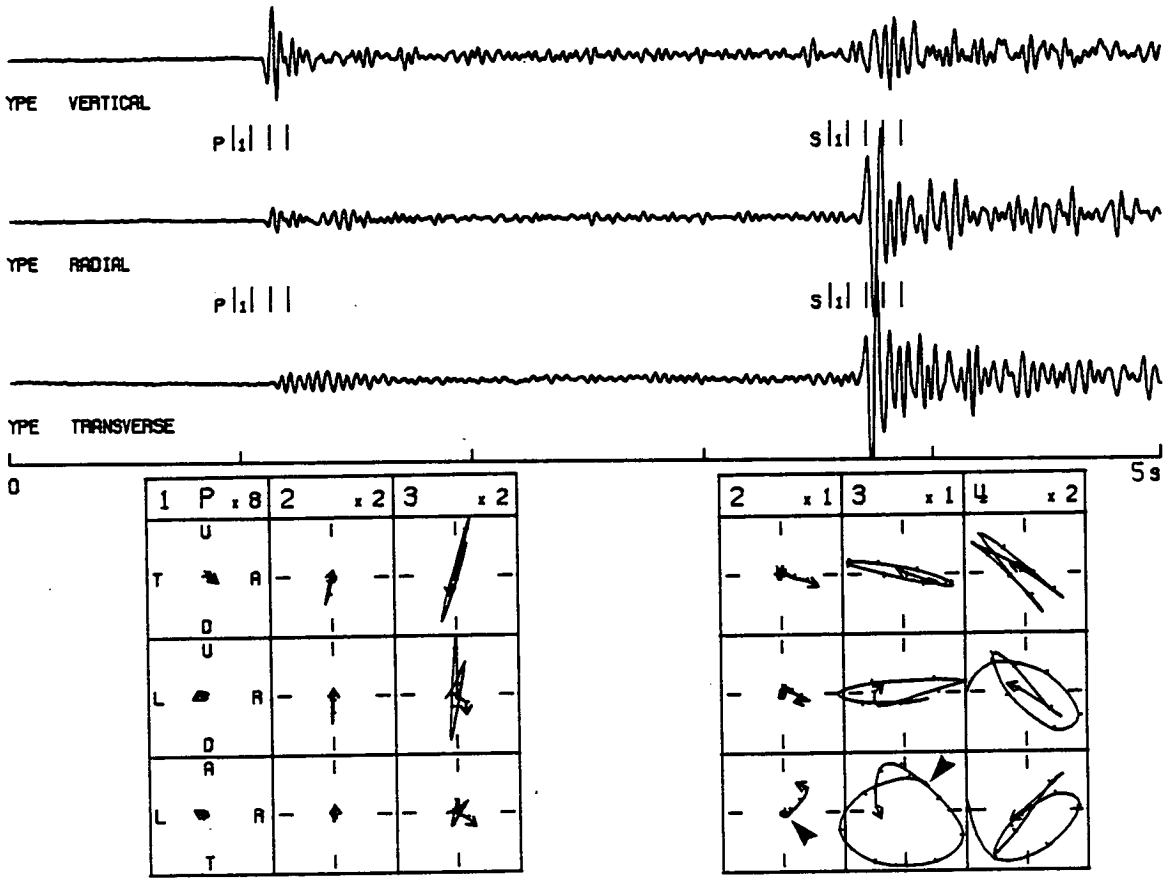
YPE VERTICAL
P
S
YPE RADIAL
P
S
YPE TRANSVERSE
0
5s
1 P x 8
2 x 2
3 x 2
2 x 1
3 x 1
4 x 2
U
T A
D
U
L R
D
A
L R
T

At this stage I rejected a number of records, including most from station YCL, with emergent shear-wave onsets and unclear polarizations. A few records from larger events had to be rejected because the signal amplitude was large enough to saturate the instruments. The polarizations from the remaining records are shown in Figs. 3.5 and 3.6. The polarizations at each station are aligned, as expected for shear-waves propagating through vertical parallel microcracks (Fig. 3.1) but the direction of alignment is different at each station. There is considerable scatter at all stations except YPE. Circular mean polarization directions, standard deviations and mean resultant lengths (a measure of the degree of alignment, Mardia 1972) are listed in Table 3.2.

The polarizations show no systematic change with time (Fig. 3.5).

3.4 Comparison with source polarizations

In the absence of anisotropy the observed polarizations would be those radiated from the source mechanisms, modified only by interaction with internal interfaces and topography (Crampin *et al.* 1986a). I compared the observed polarizations from 15 aftershocks with theoretical source polarizations from double-couple fault plane mechanisms (Table 3.3), determined from P-wave first motions at the BGS stations. Source-radiated and observed polarizations are shown in Fig. 3.7.

Errors in the positions of the observed shear-wave arrivals on the focal sphere may arise from errors in the hypocentre location and calculated P-wave takeoff angles, due to discrepancy between the true velocities of waves in the rock and the HYPO71 velocity

Fig. 3.5 Horizontal projections of the polarizations of shear-wave first arrivals at the four three-component stations, shown in equal-area projection of the lower hemisphere of directions out to 20°. The graph below each projection shows the polarizations plotted against time. Polarizations are in degrees east of north.

Fig. 3.5

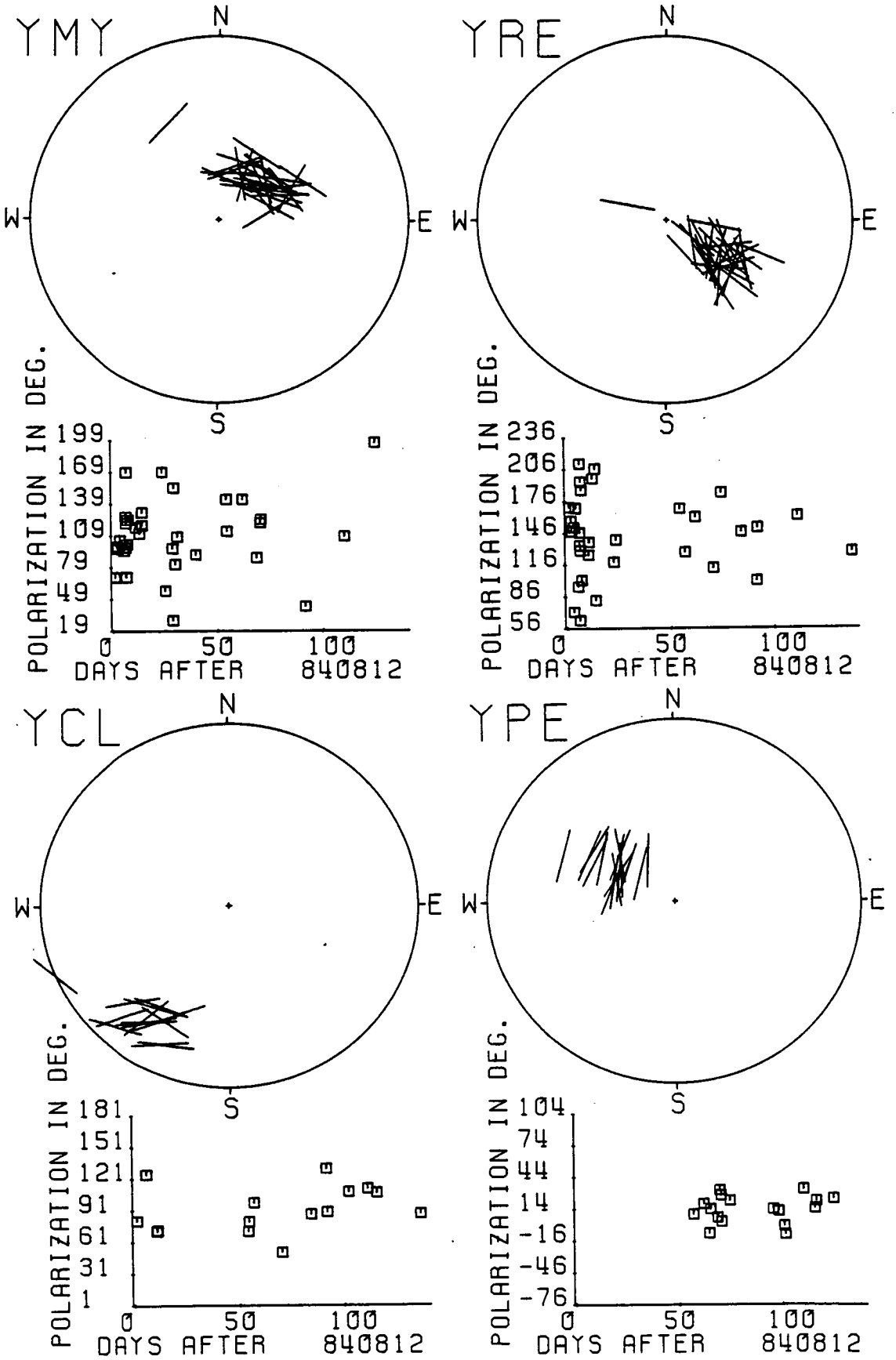
YMY
N
W
E
S
POLARIZATION IN DEG.
199
169
139
109
79
49
19
0
50
100
DAYS AFTER
840812
YRE
N
W
E
S
POLARIZATION IN DEG.
236
206
176
146
116
86
56
0
50
100
DAYS AFTER
840812
YCL
N
W
E
S
POLARIZATION IN DEG.
181
151
121
91
61
31
1
0
50
100
DAYS AFTER
840812
YPE
N
W
E
S
POLARIZATION IN DEG.
104
74
44
14
-16
-46
-76
0
50
100
DAYS AFTER
840812

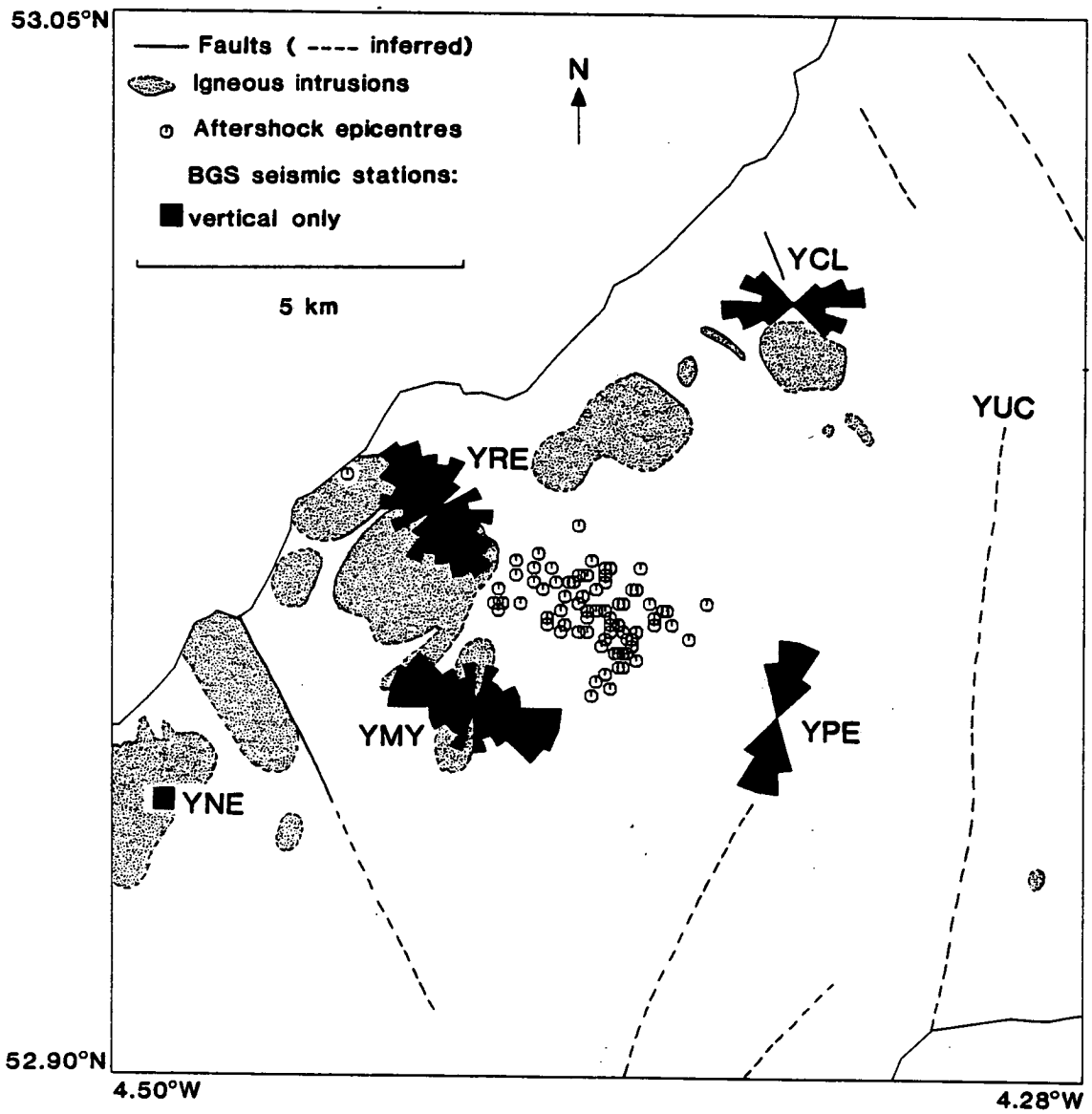

Fig. 3.6 Equal-area rose diagrams of the polarizations of shear-wave first arrivals at the four three-component stations, superimposed on the geological map of Fig. 3.3.

Table 3.3 Focal parameters of 22 earthquakes. Strike, dip and rake are as defined by Aki and Richards (1980). The numbered events are those for which shear-wave radiation patterns are shown in Fig. 3.7.

	Date and Time						Location					Mechanism		
							Latitude		Longitude		Depth	M_L	strike	dip	rake
No	Y	M	D	H	M	S	°N	min	°E	min	km		N°E	°	°
	84	8	14	2	50	9.37	52	58.17	-4	23.78	22.61	1.99	186	62	-55
1	84	8	15	8	41	45.69	52	57.76	-4	23.91	21.50	1.17	146	80	-90
	84	8	15	16	14	43.22	52	58.21	-4	24.21	22.30	0.49	162	64	-38
2	84	8	17	10	37	53.30	52	57.96	-4	22.58	22.49	1.38	20	70	-32
	84	8	17	11	3	59.10	52	57.89	-4	24.59	23.11	0.53	213	48	-135
3	84	8	18	7	42	30.06	52	57.83	-4	23.63	21.78	1.22	134	42	-113
	84	8	18	9	13	16.72	52	57.56	-4	23.18	22.10	1.37	152	62	-90
	84	8	18	11	37	27.73	52	57.41	-4	22.98	20.56	4.30	128	66	-90
4	84	8	18	15	58	19.24	52	57.77	-4	23.27	22.59	0.56	156	76	-20
5	84	8	19	4	50	53.12	52	58.07	-4	23.46	23.37	0.58	55	80	145
6	84	8	19	9	10	29.97	52	57.83	-4	23.42	21.52	0.15	243	78	-147
7	84	8	20	1	28	3.47	52	58.01	-4	23.93	22.75	-0.17	15	82	-8
	84	8	22	18	26	1.90	52	57.69	-4	23.38	21.41	1.07	20	70	-37
	84	8	24	22	45	1.38	52	57.54	-4	22.96	20.00	1.33	12	64	-48
8	84	8	26	17	7	2.60	52	57.37	-4	23.35	21.66	0.26	66	50	108
9	84	9	5	14	37	10.73	52	58.25	-4	24.10	22.90	1.19	13	80	-31
10	84	10	6	1	8	39.58	52	57.78	-4	23.79	22.78	1.13	180	62	-32
													185	64	-31*
11	84	10	8	20	47	36.25	52	57.50	-4	23.07	20.91	1.09	196	74	-8
12	84	10	16	12	35	5.55	52	57.53	-4	23.19	22.73	1.29	162	64	-36
13	84	10	17	3	51	43.08	52	57.95	-4	23.18	22.62	0.75	258	72	-159
14	84	10	22	13	34	31.94	52	57.92	-4	22.14	22.74	1.13	100	60	-157
													96	50	-156*
15	84	10	26	13	11	35.35	52	57.38	-4	23.43	23.46	1.05	37	40	90

*Focal mechanisms adjusted to improve fit of synthetic seismograms.

Fig. 3.7 Fault-plane solutions and theoretical shear-wave radiation patterns (out to incidence angle 45°) of 15 aftershocks, numbered to correspond with the list of focal parameters in Table 3.3. The observed polarizations of the first-arriving shear waves from these earthquakes at the named stations are shown as superimposed arrows. The projections are equal-area of the upper focal hemisphere; in the fault-plane solutions, crosses represent the P and T axes, open dots, dilations, filled dots, compressions, and smaller dots, less certain readings.

Fig. 3.7

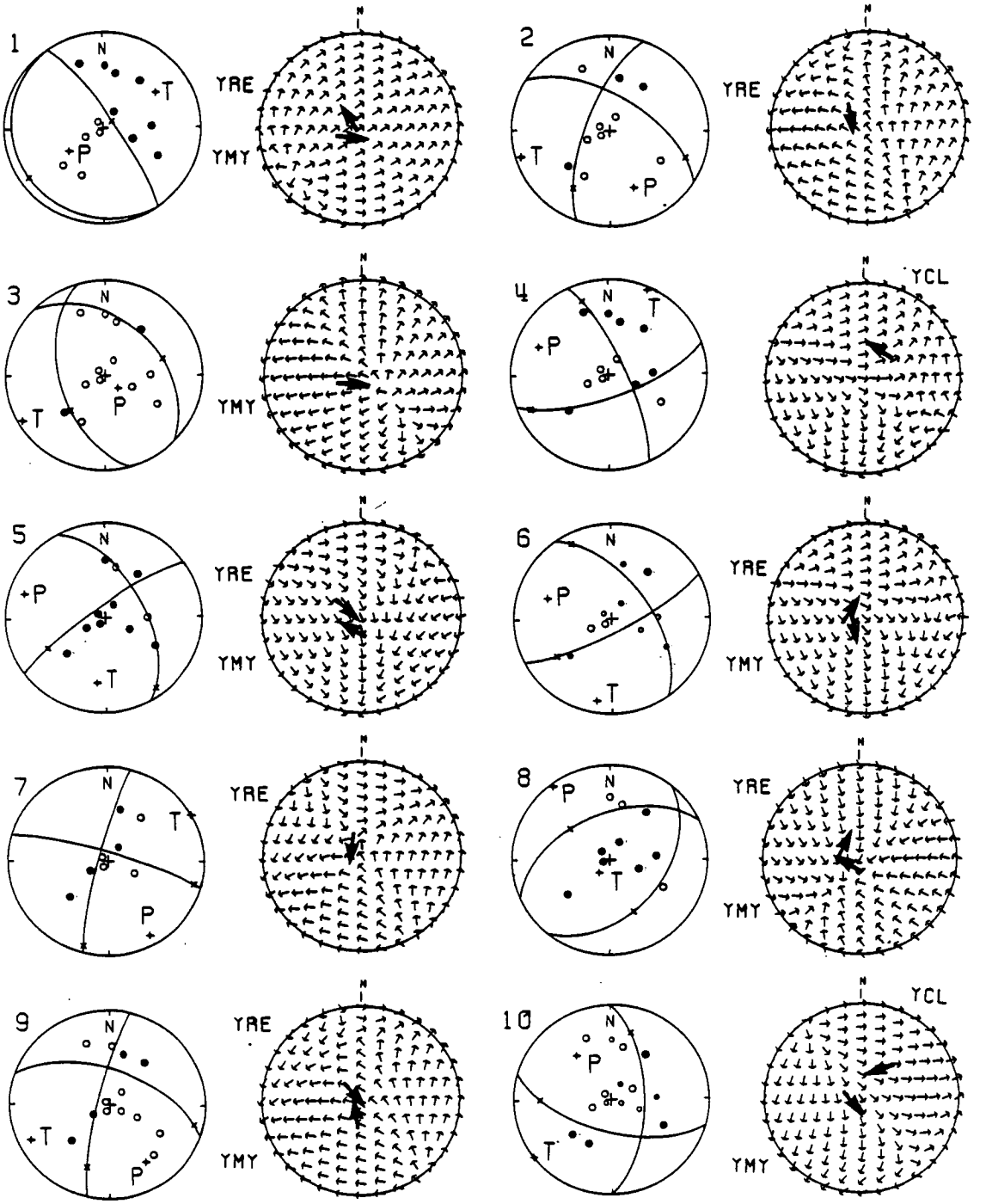
1
N
T
P
YRE
YMY
2
N
T
P
YRE
3
N
T
P
YMY
4
N
T
P
YCL
5
N
P
T
YRE
YMY
6
N
P
T
YRE
YMY
7
N
T
P
YRE
8
P
N
T
YRE
YMY
9
N
T
P
YRE
YMY
10
N
P
T
YCL
YMY

Fig. 3.7 (cont.)

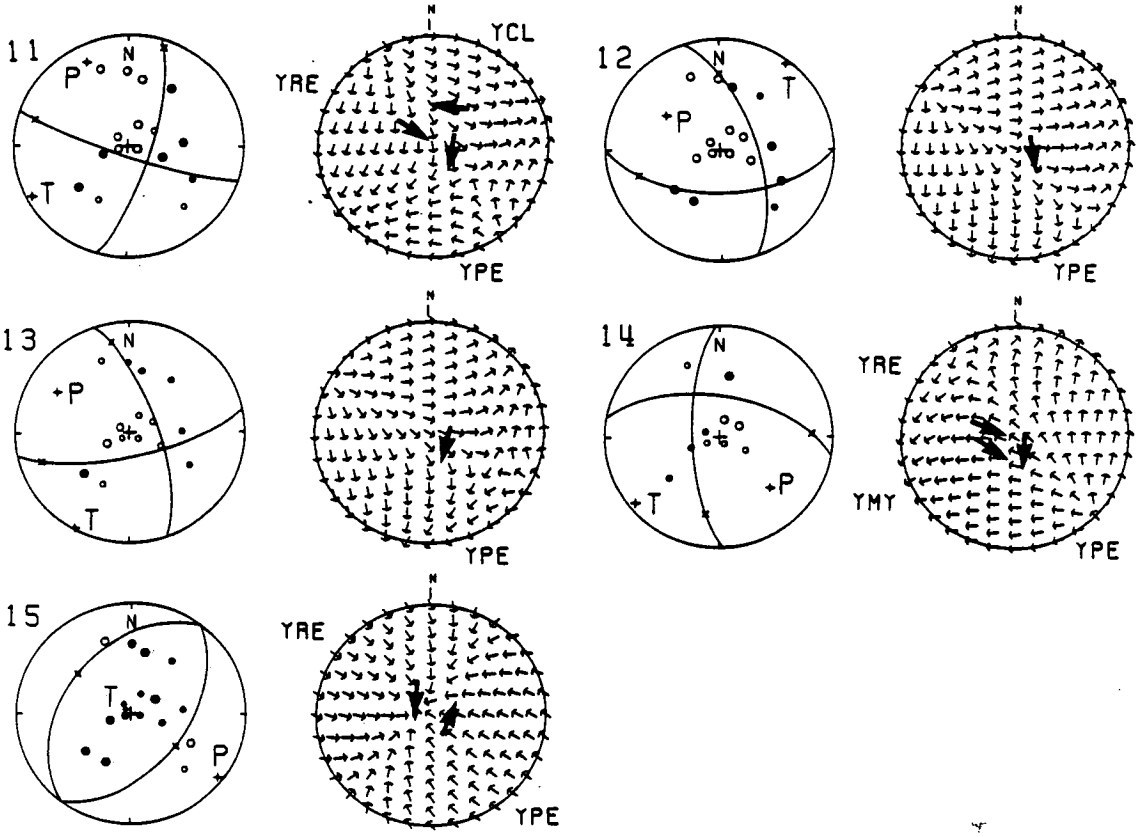
11
P
N
T
N
YCL
YRE
YPE
12
N
T
P
N
YPE
13
N
P
T
N
YPE
14
N
T
P
N
YRE
YMY
YPE
15
N
T
P
N
YRE
YPE

model. Inhomogeneity and effective anisotropy in the rock, unrecognized by HYPO71, contribute to the error (Doyle *et al.* 1982). Errors in the fault-plane solutions, due to misreading of the P-wave first motions or ambiguity in location of nodal planes, may cause errors in the derived source radiation pattern. The events in Fig. 3.7 have reasonably well-constrained nodal planes, so errors in the source mechanism should not be severe. The effect of these errors should be small except for observations near the intersection of nodal planes or near P or T axes, since over the rest of the focal sphere the source polarizations vary slowly with position, so their mislocation with respect to the observed polarizations will cause only minor errors. Nevertheless I have not attempted detailed comparison of the source and observed polarizations, and make only general comments.

The shear-wave polarizations (disregarding polarities) observed at station YMY from events 1, 3, 5, 8 and 10; station YRE for events 1, 5, 11 and 14; station YCL for events 10 and 11; and station YPE for events 11-15 deviate from the source polarization towards the dominant direction of shear-wave polarization at these respective stations (Fig. 3.6). At station YMY for events 6, 9, and 14; station YRE for events 2, 6, 7, 8, 9, and 15, and station YCL for event 4, source polarizations close to the dominant direction of shear-wave polarization at the station appear to give rise to observed polarizations deviating appreciably from the dominant direction.

The observed shear-wave polarization deviating from the source polarization towards a common direction is evidence that anisotropy is affecting the source polarizations (Crampin *et al.* 1986a).

Scattering of the observed polarizations away from the mean direction, and errors in the position of the observed arrival with respect to the source radiation pattern, may be the cause of many of the observations not fitting this pattern.

The poor agreement of many of the source and observed *polarities* may be due to the shear-wave first break being indistinct from the P-wave coda.

3.5 Interpretation of polarizations

In the Turkish Dilatancy Projects (Crampin and Booth 1985) and other studies of shear-wave polarizations (see Crampin 1986a) uniform alignments of shear-wave polarizations over all the network stations were attributed to vertical cracks aligned parallel to the axis of compression (or normal to the axis of tension) of the regional stress field. Polarizations not aligned with the regional stress field were generally explained by scattering of the shear waves by topography (e.g. Chen *et al.* 1986); or by cracks aligned in local stress anomalies (Peacock *et al.* 1986: see Chapter 4). In North Wales, despite subdued topography (compared with the TDP study area, Crampin *et al.* 1985) and near-vertical shear-wave incidence angles, the polarizations at the four stations are not all aligned in one direction. It seems that the polarizations are affected either by cracks aligned in a non-uniform stress field, or by some mechanism other than EDA, which varies from station to station. The evidence presented in the next section indicates that the stress field is uniform, and I suggest that the cause of the diverse polarization alignments is strongly anisotropic slate.

3.5.1 Evidence for a uniform regional stress field

Focal mechanisms of 22 aftershocks, derived from P-wave first motions, show that slip is occurring along a variety of planes (Fig. 3.8). If a common stress field is exciting all these motions, its orientation should appear as a common area in a superposition of nodal planes (Crampin and Booth 1985). A common area of tension, in the northeast quadrant, is defined when the nodal planes of the 22 aftershocks are superimposed (Fig. 3.9). This tension is in accord with the stress axes of the mainshock focal mechanism (Turbitt *et al.* 1985; Trodd *et al.* 1985), and with an *in-situ* stress measurement in the cavern of the Dinorwic pumped-storage power station, 25 km from the epicentral area (Douglas *et al.* 1977), which indicates a compressive axis striking N 300°E and dipping 26°. Other *in-situ* stress measurements (Klein and Brown 1983), and focal mechanisms of several recent British earthquakes (Marrow and Walker 1986), show that this approximately northwest-southeast compression affects most of Britain. Stress measurements from northern and central Europe also indicate uniform northwest-southeast compression (Greiner and Illies 1977; Liu 1983).

From the above evidence, the stress field in the Lleyn Peninsula is uniform both laterally and with depth down to the focal zone of the aftershocks. EDA aligned in the regional stress field would probably be uniform at all depths, so it seems likely that the observed polarizations are affected by local phenomena other than stress-aligned cracks.

Fig. 3.8 Fault-plane solutions of 22 aftershocks. Equal-area projections of the upper focal hemisphere.

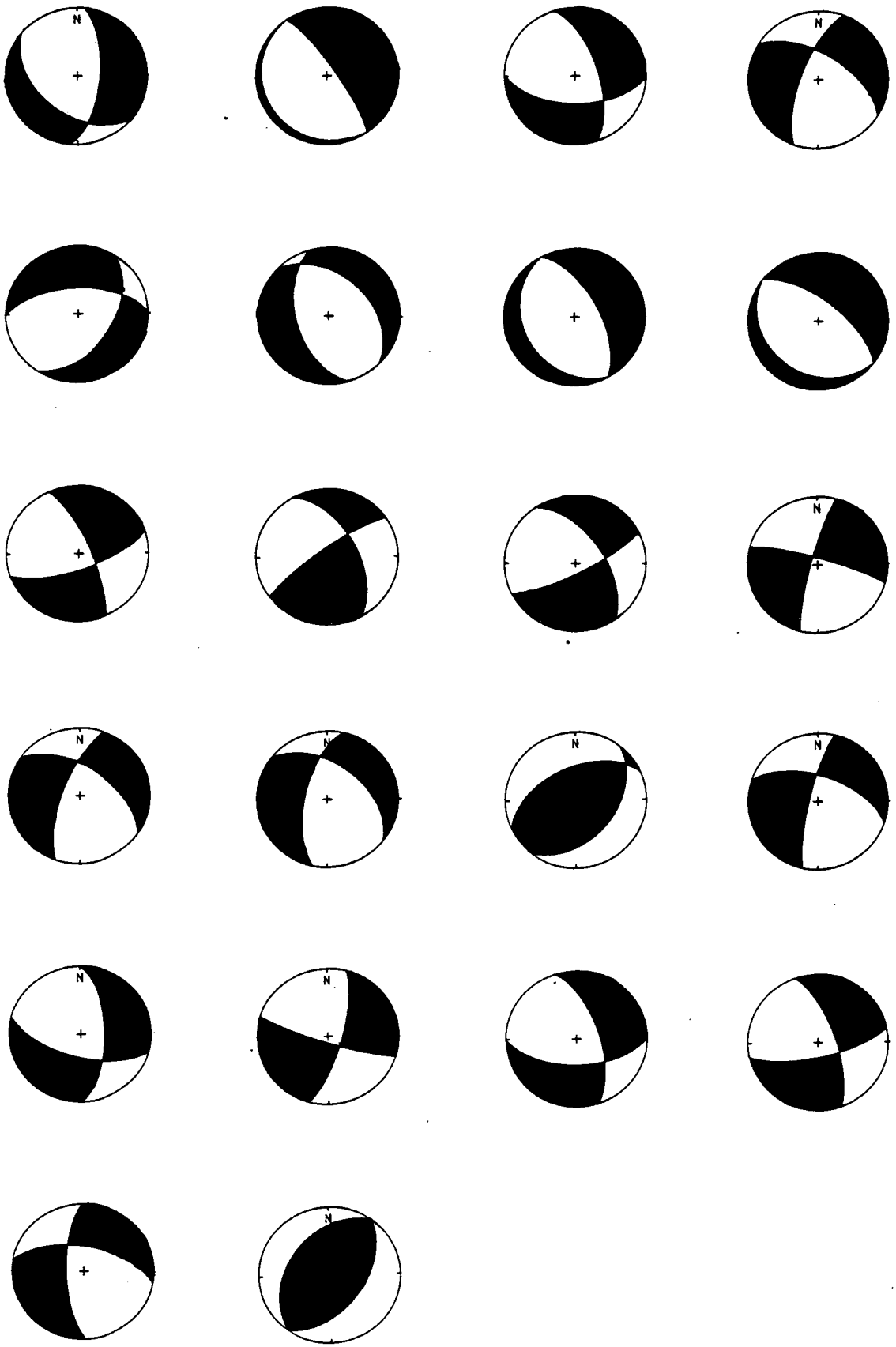

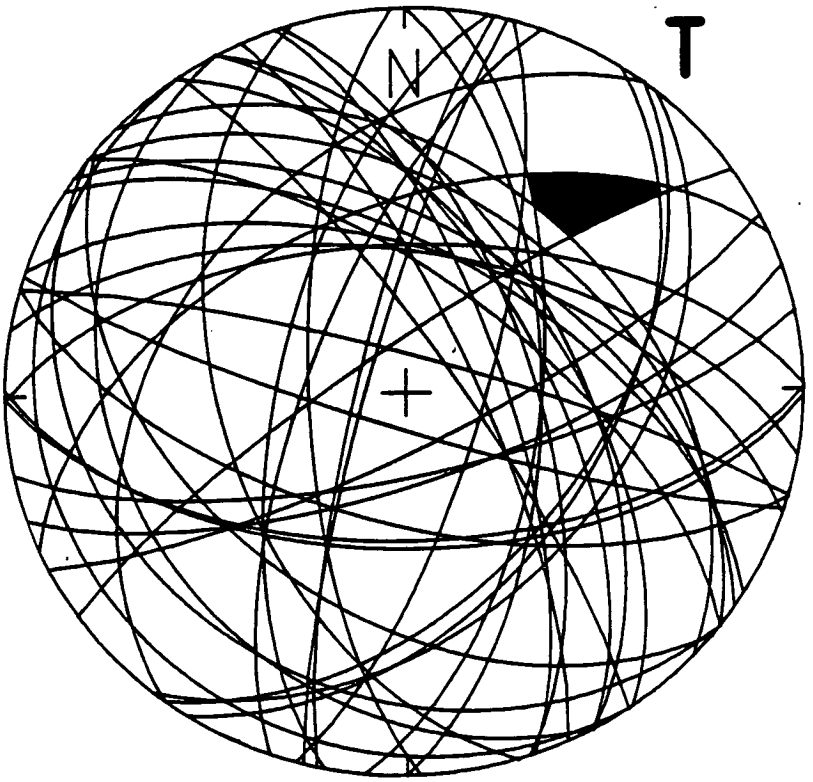

Fig. 3.9 Superimposed nodal planes of 22 focal mechanisms, showing a common area of tension.

3.5.2 Anisotropic slate - a possible cause of polarization alignment

At least three of the stations may be underlain by slate, either at the surface or at depth (A. Reedman, M. Howells, personal communication). The slate has a cleavage which generally dips near-vertically and strikes approximately N 70°E; the cleavage orientation is perturbed around the igneous intrusions, which were present before the cleavage developed (A. Reedman, personal communication). Christensen (1965, 1966) has found from laboratory measurements that a slate from Poultney, Vermont, USA, is anisotropic with hexagonal symmetry about an axis perpendicular to the plane of the cleavage, and with highest P- and shear-wave velocities in directions in the plane of the cleavage. For shear waves propagating in the plane of the cleavage, the wave polarized parallel to the cleavage travels faster than the wave polarized perpendicular to the cleavage. The cleavage and anisotropy are caused by formation of thin tabular crystals of anisotropic minerals (micas) perpendicular to the direction of maximum compression at the time of metamorphism (Harker 1950). Cracks along grain boundaries may also contribute to the anisotropy (see Chapter 1).

There are no detailed velocity measurements for the igneous rocks at the station sites, but laboratory experiments on other granites show that anisotropy due to crystal alignment is generally negligible (Nur and Simmons 1969; Babuška 1984).

3.5.3 Polarizations at YMY - aligned cracks (EDA)

The polarizations at station YMY are approximately parallel to the regional direction of compression indicated by the aftershock focal mechanisms and the *in-situ* stress measurement at Dinorwic. As the site is covered with drift, it is not certain whether the underlying rock is slate or felsite, but the perturbed cleavage of the slate around the igneous intrusions in this district tends to be parallel to the nearest contact of the intrusion (A. Reedman, personal communication), which is NNE-SSW here, so it seems unlikely that slate is causing the polarization alignment at YMY. Following the examples cited at the beginning of the chapter, I suggest that the shear-wave splitting and polarizations at YMY are due to vertical or near-vertical cracks and microcracks in the felsite and underlying rocks, aligned by the regional stress field. There is strong circumstantial evidence that the cracks are fluid-filled (Crampin *et al.* 1984b), but the seismic evidence is insufficient to confirm this.

3.5.4 YRE and YCL - slate or cracks

Raypaths from the aftershock zone to both YRE and YCL probably pass through several kilometres' thickness of igneous intrusions (see Fig. 3.3), and then through thin layers of slate before reaching the seismometers. At YRE the raypaths also pass through landslide debris, which may account for the "low-pass filter" effect mentioned earlier. The igneous intrusions and underlying rocks may be pervaded by cracks and microcracks aligned in the northwest-southeast regional stress field, as at YMY. The observed mean polarization direction at YRE and some of the individual

readings at YCL are approximately parallel to the regional stress field; but it is possible that the anisotropic slate, rather than stress-aligned cracks, causes the aligned polarizations at one or both sites. The cleavage of the slate at YCL strikes N 100°E and dips at 50°, and at YRE strikes approximately WNW-ESE (A. Reedman, personal communication). If the slate is as anisotropic as Christensen's samples from Poultney, then polarizations due to EDA in the underlying rock may be overprinted by even a thin layer of slate with vertical or steeply dipping cleavage. At YRE and YCL the strike of the slaty cleavage and the direction of regional compression are so similar that it is not possible to distinguish which is responsible for the observed polarization alignments.

3.5.5 YPE

Station YPE lies on an andesite boss approximately 700 m in diameter, surrounded and probably underlain by slate (A. Reedman, M. Howells, personal communication; Tremlett 1965; Croudace 1982), with cleavage striking ENE-WSW (J. A. Evans, personal communication), but possibly perturbed by the intrusion (A. Reedman, personal communication). Joints in the andesite trend N 75°E, and there is weak foliation parallel to the joints (A. Reedman, personal communication). The observed north-south shear-wave polarizations are not parallel to the slaty cleavage, the joints, or the strike of stress-aligned cracks inferred from station YMY. The alignment may be due to scattering by topography or irregular interfaces between contrasting rock types; but the topography is gentle around the site and should have little effect on near-vertically incident shear waves, and there is no evidence

of scattering in the generally clear and simple shear-wave arrivals at YPE. (see Fig. 3.4d).

3.6 Synthetic seismograms

To test my interpretation of the shear-wave polarizations, I synthesized seismograms at station YRE, assuming that cracks in the igneous rock, rather than the slaty cleavage, are responsible for the polarization alignment; and station YCL, assuming that a thin surface layer of slate is responsible for the alignment. I used the anisotropic reflectivity method (Booth and Crampin 1983a; Crampin and Booth 1985) with a velocity model of a thin surface layer over a layer of cracked rock extending to the depth of the source. Elastic constants for the cracked layers (Table 3.4) were derived by the method of Hudson (1980, 1981; Crampin 1984b) for fluid-filled cracks in an intrinsically isotropic medium with velocities intermediate between those of layers 2 and 3 of the LISP-B velocity model (V_p = 6.3 km/s; V_s = 3.8 km/s). The velocity variations in the cracked layer with crack density 0.01 and negligible aspect ratio are shown in Fig. 3.10(a) (crack density is the dimensionless quantity Na^3/v where N is the number of cracks of radius a in volume v of rock).

The choice of events to model was restricted to those in Fig. 3.7, for which there are both clear shear-wave arrivals and well-constrained fault-plane solutions. For station YCL, only event 10 in Fig. 3.7 has both of these requirements. Event 14 has the best shear-wave arrival at station YRE. I made small adjustments to the fault-plane solutions of both events to improve the match between the relative amplitudes of the synthetic and observed split shear-wave components. The adjusted fault-plane

Table 3.4 Elastic parameters of cracked medium and slate used in synthetic seismograms

	cracked rock crack density 0.01 density=2.64g/cm^3 elastic constants (units 10^{10}N/m^2)	Slate (Christensen 1966) density 2.77g/cm^3 elastic constants (units 10^{10}N/m^2)
c_{1111}	9.6873	6.7598
c_{3333}	9.6889	10.9244
c_{1133}	2.8225	4.2163
c_{1313}	3.3540	2.0193
c_{2323}	3.4330	3.9999

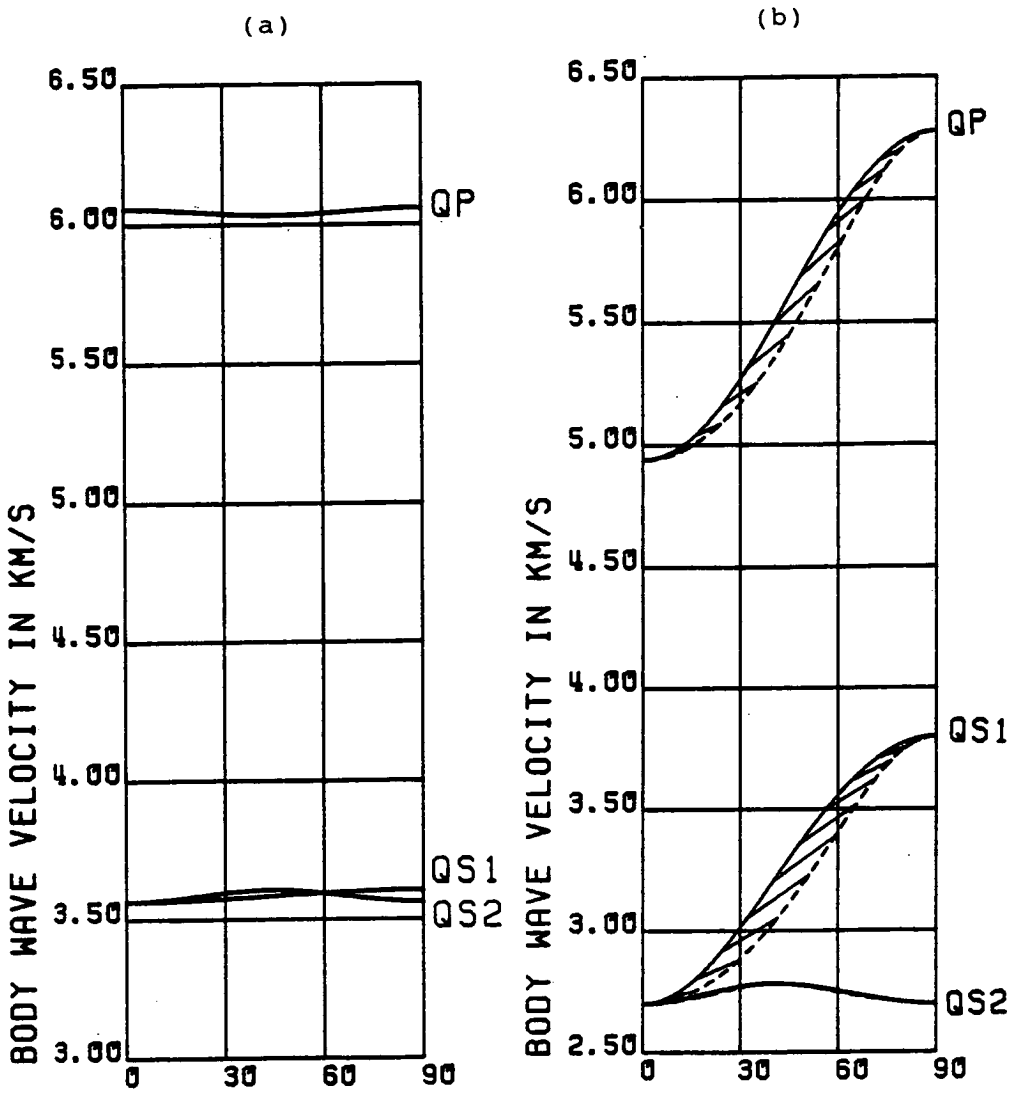

Fig. 3.10 Velocity variations of seismic waves in (a) cracked rock, (b) slate, used in synthetic seismograms. Elastic constants are listed in Table 3.5. In (a) propagation direction varies from normal (0°) to parallel (90°) to parallel liquid-filled microcracks with crack density 0.01 and aspect ratio 0.0001. The shear wave QS1 is polarized perpendicular, and QS2 parallel, to the plane of incidence normal to the crack plane. The uncracked rock matrix has velocities V_p = 6.3 km/s, V_s = 3.8 km/s. In (b) propagation direction varies from normal (0°) to parallel (90°) to the cleavage of slate from Poultney, Vermont, USA (Christensen 1965, 1966). The shear wave QS1 is polarized parallel, and QS2 perpendicular, to the plane of incidence normal to the cleavage plane. Solid lines are phase velocity, dashed lines, group velocity, and diagonal lines join corresponding phase and group velocities.

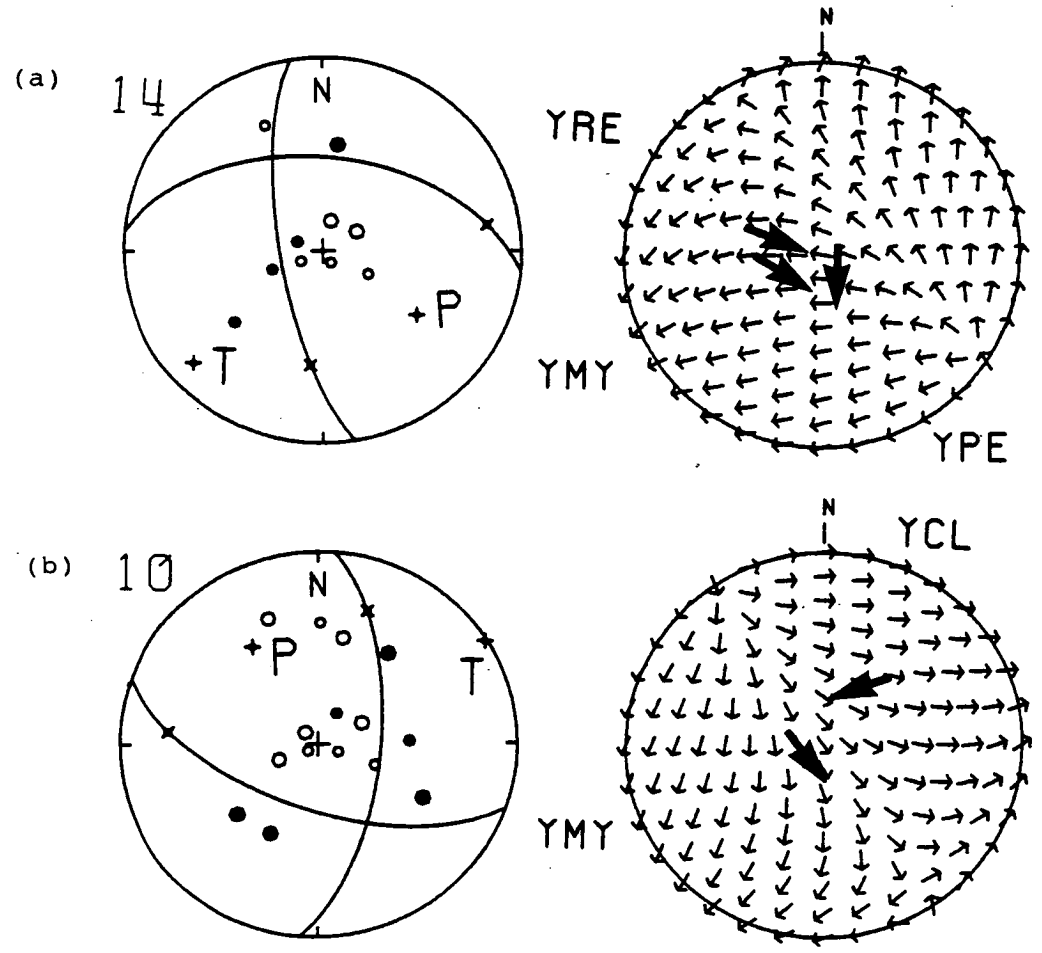

Fig. 3.11 Fault-plane solutions of the two events for which synthetic seismograms were calculated. Focal parameters are in Table 3.3. The nodal planes have been adjusted from those shown for these events in Fig. 3.7 to improve the fit of synthetic to observed seismograms. The corresponding shear-wave radiation patterns out to 45° incidence angle are shown: notation as in Fig. 3.7. Synthetic seismograms were calculated for event 14 at station YRE and event 10 at station YCL.

solutions and shear-wave radiation patterns are shown in Fig. 3.11 and listed in Table 3.3.

The parameters of the successful models for the two events are listed in Table 3.5. A model with water-filled cracks striking N 113°E and crack density 0.01 (Fig. 3.12) gives synthetic shear-wave polarizations and delay which match the observations at station YRE from event 14 (Fig. 3.11). The same model but with cracks striking east-west and symmetrical shear-wave sources produced the synthetic particle motions in Fig. 3.13, for azimuths between N 5° E and N -85° E and incidence angles within the shear-wave window. They show a first arrival polarized parallel to the strike of the cracks (arrowed) for all azimuth and incidence angles except those for which the source polarization is within 5° of perpendicular to the strike of the cracks.

For YCL I modelled the slate layer using elastic constants derived from the velocities quoted by Christensen (1965, 1966) for slate from Poultney, Vermont, USA (Fig. 3.10b; Table 3.4) since no velocity measurements exist for the Ordovician slates of the Lleyn Peninsula. I modelled the observed polarizations and delay between split shear-wave arrivals by altering only the thickness and cleavage orientation of the slate, and did not attempt to match exactly the observed depth of the earthquake or the absolute travel-times. The polarizations and delay of the split shear waves in the synthetic seismograms were determined by the slate layer alone; a thickness of 600 m and strike of 71° (Fig. 3.14b) gave the best match to the observed polarization diagrams (Fig. 3.14a). This strike is near to that of the unperturbed regional cleavage, and it is possible that the slate with perturbed cleavage, observed at the surface near YCL, does not extend far enough along the

Table 3.5 Parameters of models for synthetic seismograms.

	Event 14 at YRE	**Event 10 at YCL**	
Observed depth	23.22 km	23.45 km	
Azimuth to station	290°	31°	
Distance to station	4.2 km	6.2 km	
Observed S-wave polarization	113°	251°	
Focal mechanism:			
Strike Dip Rake	96° 50° -156°	185° 64° -31°	
Frequency of shear waves	8.5 Hz	11.0 Hz	
Velocity model			
Layer 1			
Thickness	2.0 km	0.6 km	
Type	Isotropic: HYPO71 model top layer	Anisotropic: Poultney slate, cleavage N 71° E	
Density	2.3 g/cm^3	2.77 g/cm^3	
V_p	5.4 km/s	see Fig. 3.10b	
V_s	3.2 km/s		
Layer 2			
Thickness	21.22 km	22.85 km	22.85 km
Type	Anisotropic: aligned cracks, crack density 0.01, strike N 113° E	Anisotropic: aligned cracks, crack density 0.01, strike N 113° E	Isotropic: same as halfspace
Density	2.64 g/cm^3	2.64 g/cm^3	2.64 g/cm^3
V_p	see Fig. 3.10a	see Fig. 3.10a	6.297 km/s
V_s			3.749km/s
Halfspace			
Type	Isotropic	Isotropic	
Density	2.64 g/cm^3	2.64 g/cm^3	
V_p	6.058 km/s	6.297 km/s	
V_s	3.606 km/s	3.749 km/s	

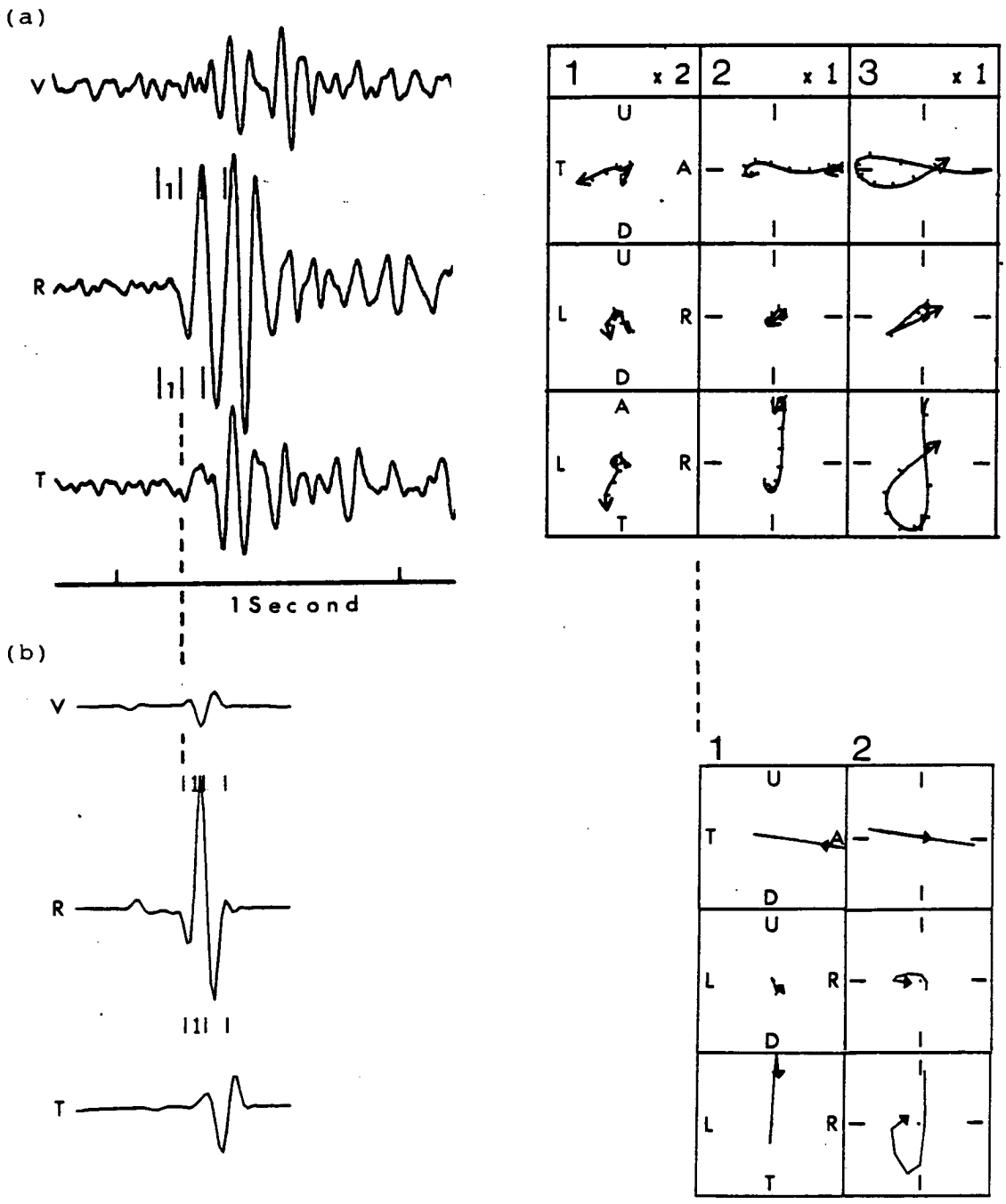

Fig. 3.12 (a) observed, and (b), synthetic seismograms and polarization diagrams for event 14 (Fig. 3.11) at station YRE. The model parameters are in Table 3.6. The seismograms are vertical (V), radial (R), and transverse (T) components. Notation as in Fig. 3.4. The window length of the polarization diagrams is 0.08 s.

Fig. 3.13 (a)

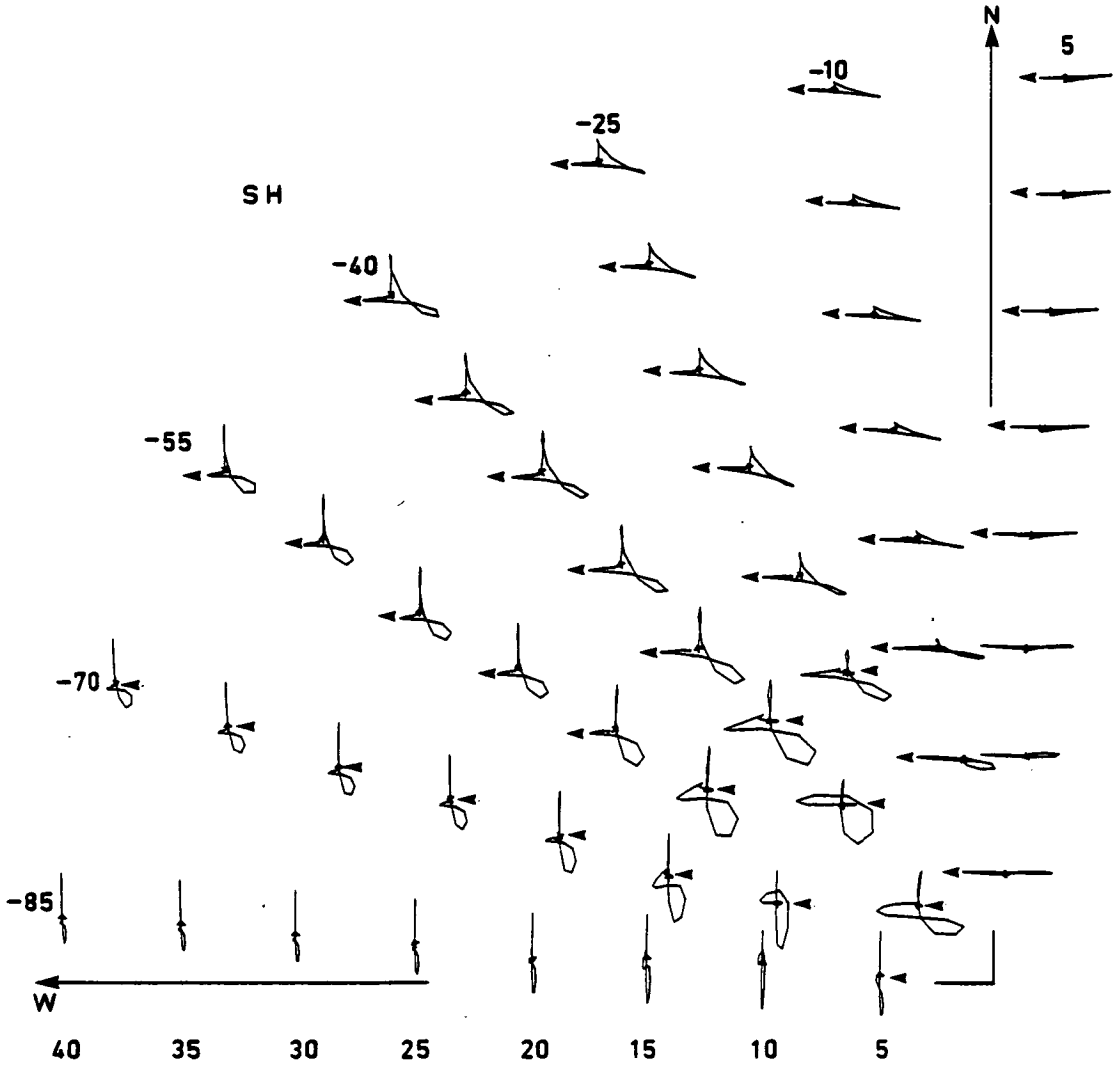

Fig. 3.13 Synthetic polarization diagrams in the horizontal plane for the marked azimuth and incidence angles from a point source at depth 23.22 km (corresponding to event 14, Table 3.3) through the model used for the synthetic seismogram for station YRE in Fig. 3.12 (parameters in Table 3.6) but with vertical parallel microcracks striking east-west. (a) Pure SH-wave source; (b) pure SV-wave source; (c) SH45SV source (a shear wave polarized at 45° to SH and SV). The polarization of the first shear-wave arrival is arrowed.

Fig. 3.13 (b)

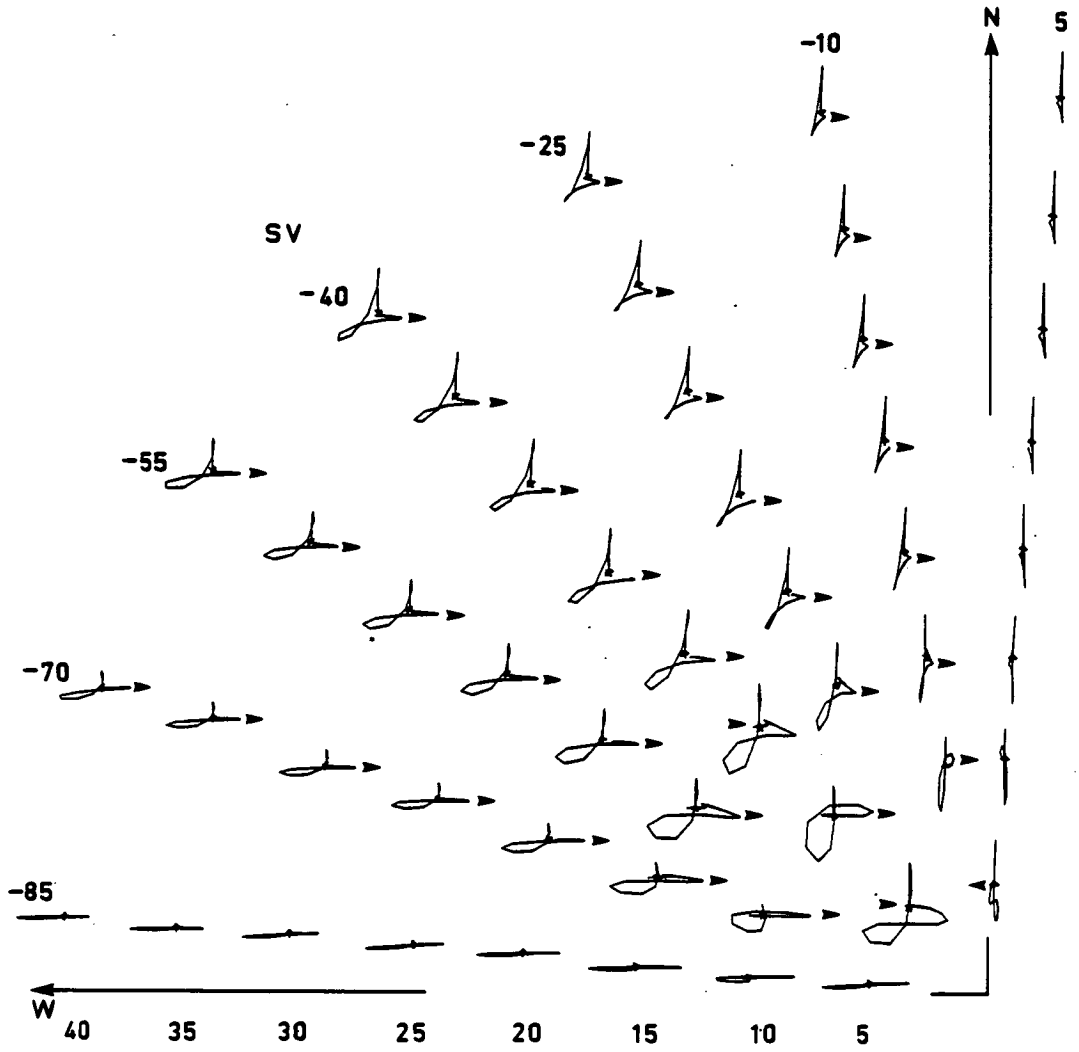

Fig. 3.13 (c)

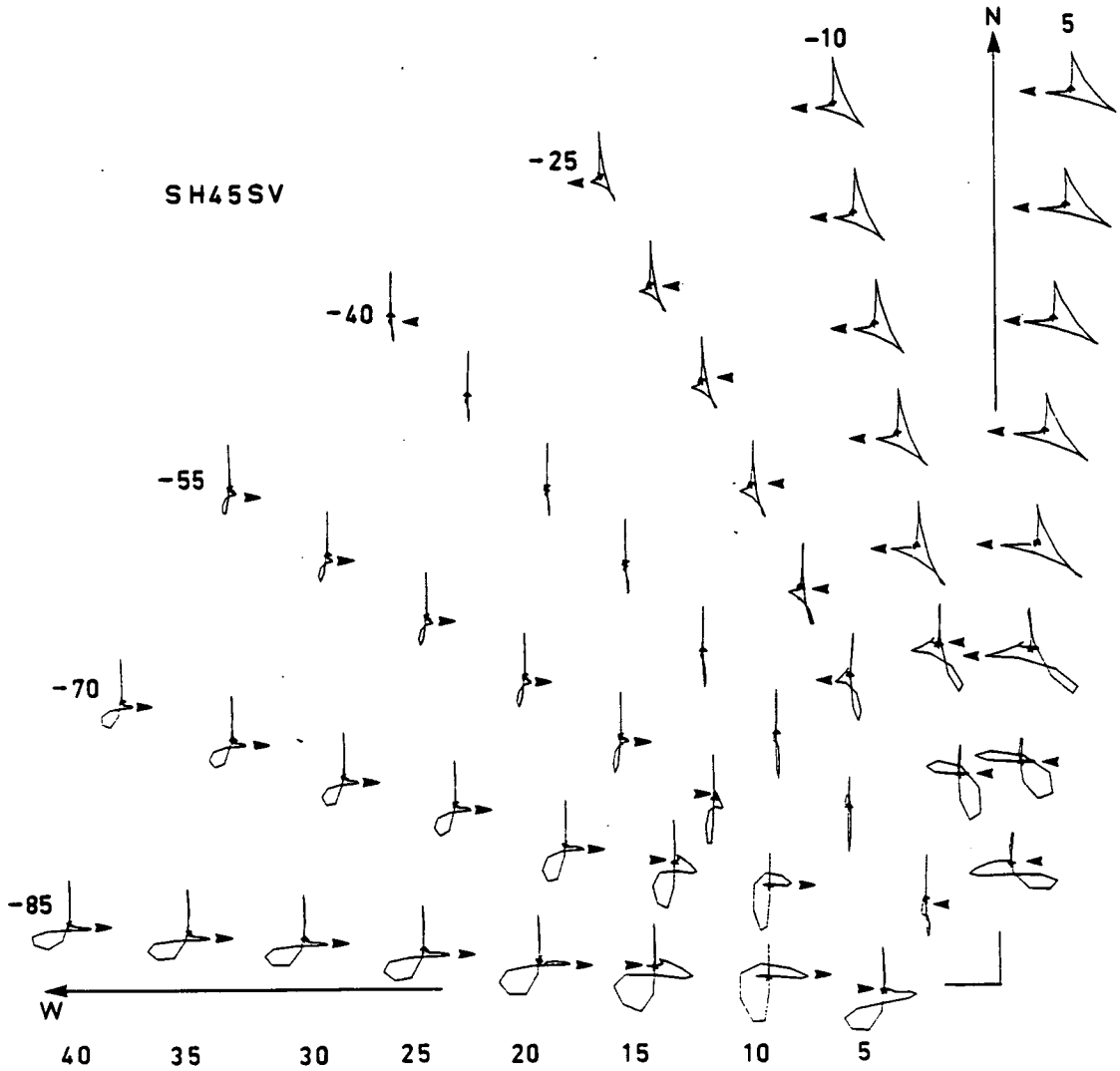

Fig. 3.14 (a) observed; and (b), (c) synthetic seismograms and polarization diagrams for event 10 (Table 3.3) at station YCL. Notation as in Fig. 3.4 and 3.12. The synthetic model in (b) is a layer of slate 600 m thick over a cracked layer which extends down to the source; in (c) the same layer of slate is over an uncracked isotropic layer (see Table 3.6 for details of model).

Fig. 3.14

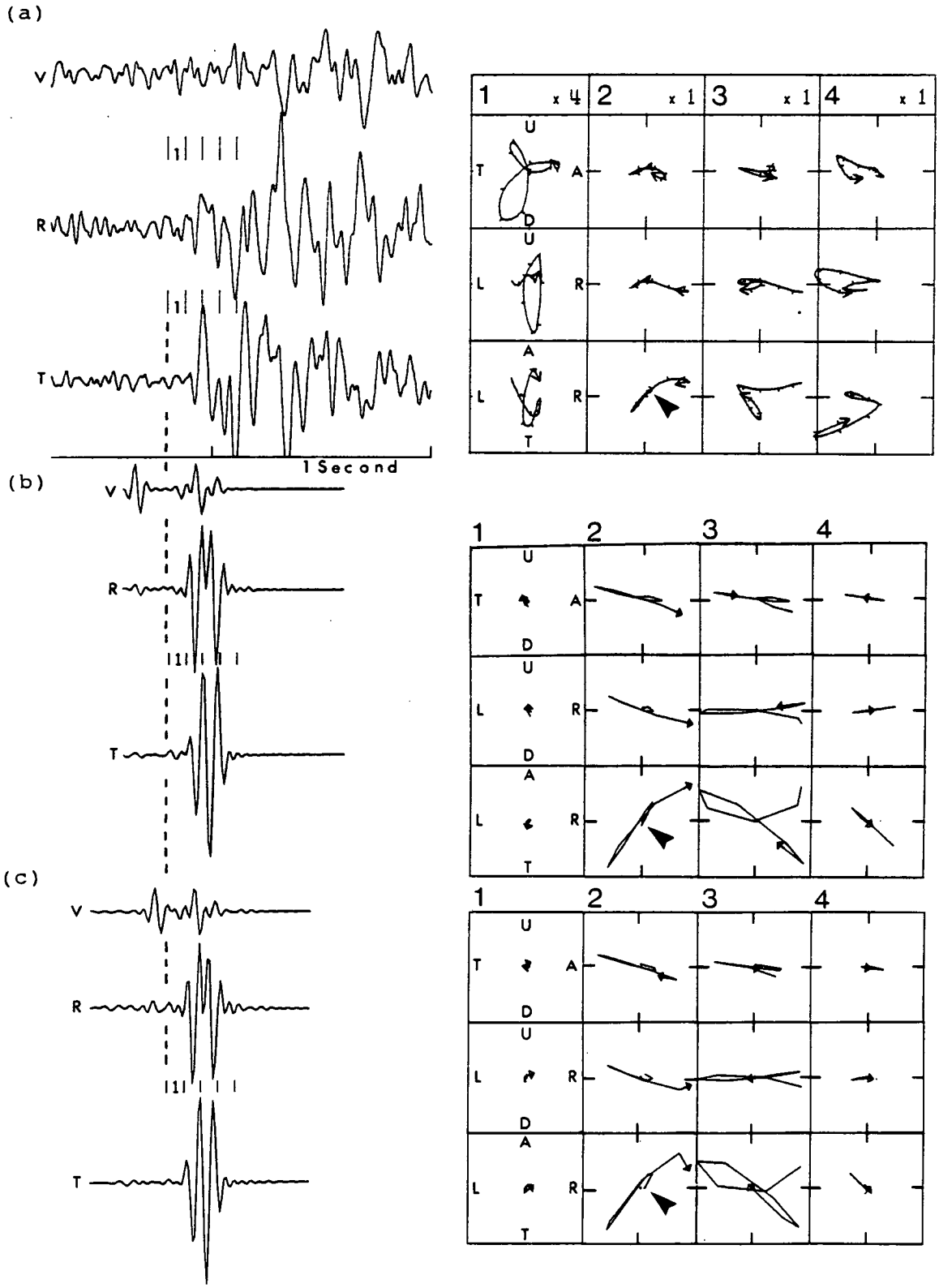

raypath from event 10 to affect the polarizations. Small differences between the velocities of the Vermont slate and the slate at YCL would not affect the polarizations of split shear waves incident near-parallel to the cleavage, but would affect the thickness of slate required in the synthetic model to match the observed delay between split shear-wave arrivals. The cracks have no effect at all (Figs. 3.14b, c) since the source polarization (110°; Fig. 3.11b) is near-parallel to the crack orientation (113°).

Although synthetic seismograms for both station YRE and station YCL match the observed seismograms reasonably well, the models of uniform cracked layers and slate are probably non-unique and oversimplified. They serve only to test the interpretation of the shear-wave polarizations, not to constrain the geological structure or extent of anisotropy beneath the stations: for that a joint inversion of hypocentral location and structure including anisotropy should be performed (Doyle *et al.* 1985).

3.7 Comparison with similar results from Japan

Shear-wave splitting with the leading shear wave polarized parallel to slaty cleavage in surface rocks has been observed at a seismic station at Yagi in the Kinki district of Honshu, Japan, by Kaneshima *et al.* (1986a). The polarizations at this station are approximately parallel to the compression direction of the regional stress field (deduced from earthquake focal mechanisms) and to polarizations at a nearby station on granite, which are probably caused by cracks aligned in the stress field; so the aligned polarizations at the station on slate could be caused by either

slaty cleavage or EDA or both. On the Lleyn Peninsula the slaty cleavage and regional stress field are approximately parallel at stations YRE and YCL, causing similar ambiguity.

At Yagi as at YCL, shear-wave arrivals are generally complicated and unclear, even when they are well within the shear-wave window. The topography around Yagi is relatively smooth, and it seems possible that the cause of the scatter at both stations is an irregular interface between the slate and underlying rock.

3.8 Delays between split shear-wave arrivals

Delays between the arrivals of split shear waves at each of the four stations are plotted against time in Fig. 3.15, to show any temporal change that might be caused by EDA responding to a change in stress. An observation of temporal change would prove that the shear-wave splitting is due to effective anisotropy caused by aligned cracks, since no other type of anisotropy in the cool, brittle crust can change so rapidly.

The difficulty in measuring delays between split shear-wave arrivals is in identifying the arrivals correctly. Once we have determined a significant mean polarization of the faster shear wave at a station we can reject from further analysis any first arrivals that are polarized perpendicular to the mean direction, since these are probably strong arrivals of the slower shear wave generated by a source polarization near-perpendicular to the polarization of the faster shear wave in the medium (Crampin *et al.* 1986a). My criterion for a slower shear-wave arrival was that the polarization should be further than 45° or two standard deviations (whichever was larger) from the mean direction at that station. Only one

Fig. 3.15 Equal-area projections out to incidence angle 20°, of the delays between split shear-wave arrivals at the four three-component stations, normalized by path length. The areas of the circular symbols are proportional to the delays. The graphs show the delays plotted against time.

Fig. 3.15

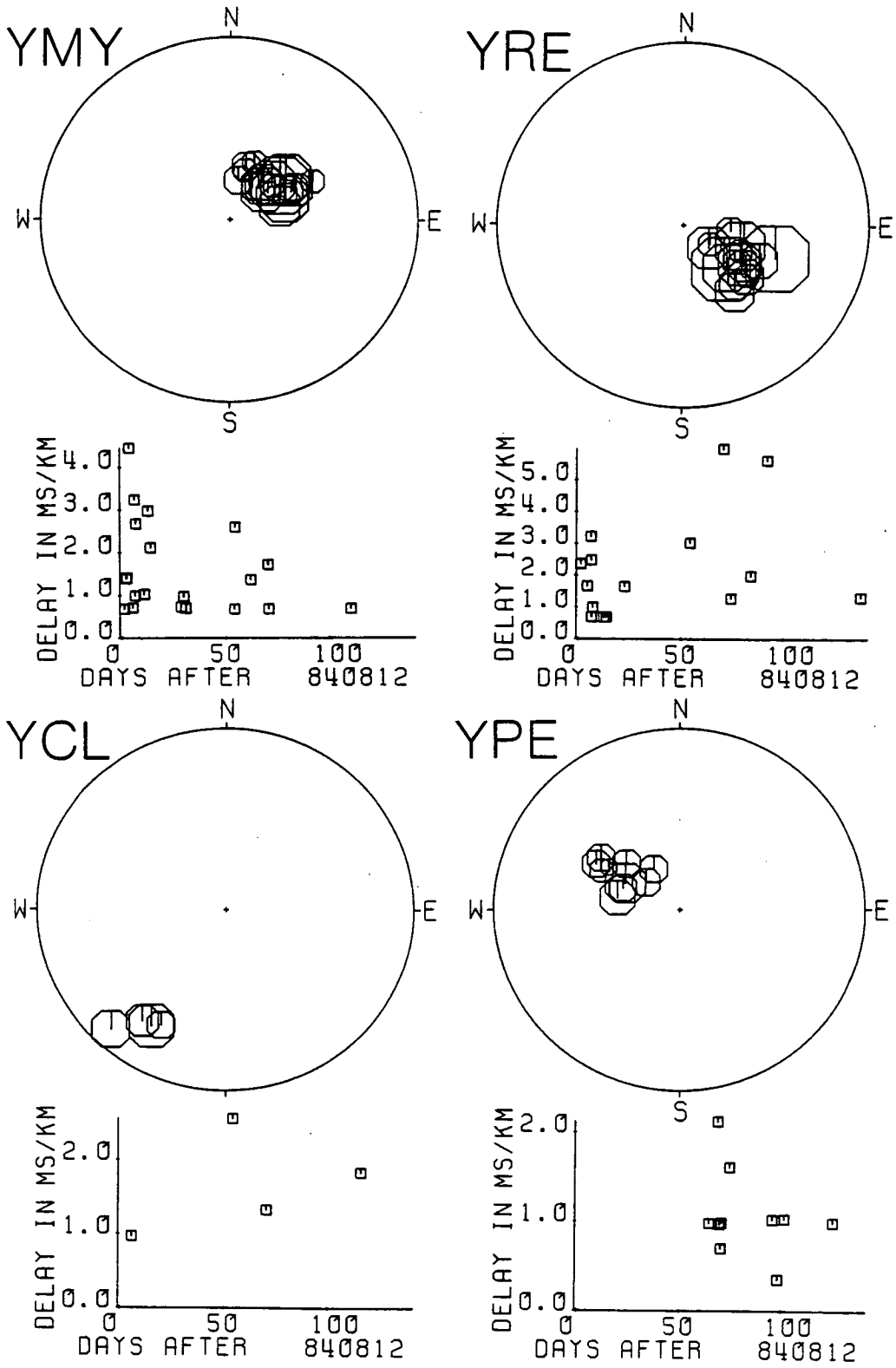
YMY
N
W
E
S
DELAY IN MS/KM
4.0
3.0
2.0
1.0
0.0
0
50
100
DAYS AFTER
840812
YRE
N
W
E
S
DELAY IN MS/KM
5.0
4.0
3.0
2.0
1.0
0.0
0
50
100
DAYS AFTER
840812
YCL
N
W
E
DELAY IN MS/KM
2.0
1.0
0.0
0
50
100
DAYS AFTER
840812
YPE
N
W
E
S
DELAY IN MS/KM
2.0
1.0
0.0
0
50
100
DAYS AFTER
840812

Table 3.6 Locations of earthquakes, polarizations of first-arriving shear wave and delays between split shear wave arrivals recorded at station YMY.

Date and Time						Location				Split shear wave	
Y	M	D	H	M	S	Latitude	Longitude	Depth	M_L	Polarization	Delay
Y	M	D	H	M	S	°N min	°E min	km		°	s
84	8	14	5	15	25.21	52 58.25	-4 24.52	22.87	0.05	70.	0.016
84	8	15	3	50	21.52	52 57.87	-4 23.97	21.39	-0.07	99.	0.031
84	8	15	8	41	45.69	52 57.76	-4 23.91	21.50	1.17	97.	0.031
84	8	16	13	44	57.89	52 57.89	-4 23.39	22.13	0.05	105.	0.102
84	8	18	7	42	30.06	52 57.83	-4 23.63	21.78	1.22	95.	0.016
84	8	19	2	58	32.92	52 57.97	-4 23.14	20.97	0.05	98.	0.070
84	8	19	3	34	1.37	52 58.23	-4 23.33	23.55	-0.05	127.	---
84	8	19	4	50	53.12	52 58.07	-4 23.46	23.37	0.58	-59.	---
84	8	19	9	10	29.97	52 57.83	-4 23.42	21.52	0.15	169.	---
84	8	19	11	33	36.88	52 58.07	-4 23.86	22.45	-0.05	70.	0.023
84	8	19	17	53	42.97	52 57.88	-4 23.63	22.85	-0.17	101.	0.062
84	8	20	2	13	31.76	52 58.48	-4 23.61	22.51	0.01	-56.	---
84	8	23	16	48	51.30	52 57.95	-4 24.77	21.73	0.05	-63.	0.023
84	8	25	12	12	4.18	52 57.76	-4 22.88	23.34	0.05	-69.	0.070
84	8	26	16	32	9.82	52 58.18	-4 23.18	22.60	0.05	-49.	---
84	8	26	17	7	2.60	52 57.37	-4 23.35	21.66	0.26	299.	0.047
84	9	5	14	37	10.73	52 58.25	-4 24.10	22.90	1.19	-11.	---
84	9	6	23	51	28.60	52 57.17	-4 23.30	23.28	0.50	57.	---
84	9	10	11	10	0.68	52 57.75	-4 22.96	21.75	0.20	97.	0.016
84	9	10	13	33	41.95	52 57.87	-4 22.42	23.26	0.87	209.	---
84	9	11	1	33	16.32	52 58.04	-4 23.72	21.78	1.40	154.	---
84	9	11	15	58	18.74	52 57.90	-4 22.71	23.43	1.33	82.	0.023
84	9	12	14	53	15.44	52 58.45	-4 24.24	22.78	0.20	108.	0.016
84	9	21	9	57	39.48	52 58.15	-4 24.79	21.62	0.84	91.	---
84	10	6	1	8	39.58	52 57.78	-4 23.79	22.78	1.13	143.	0.016
84	10	6	8	51	7.63	52 57.76	-4 23.62	22.54	0.93	-67.	0.060
84	10	13	20	37	7.87	52 57.81	-4 22.79	22.10	0.49	-37.	0.031
84	10	20	14	47	49.30	52 57.73	-4 23.11	21.52	1.03	88.	---
84	10	22	5	34	55.40	52 57.91	-4 23.78	22.02	0.46	121.	0.039
84	10	22	13	34	31.94	52 57.92	-4 22.14	22.74	1.13	124.	0.016
84	11	12	13	55	0.03	52 59.12	-4 26.82	20.35	0.13	42.	---
84	12	1	5	12	30.10	52 57.72	-4 23.06	22.93	0.58	-72.	0.016
84	12	15	21	15	19.86	52 58.16	-4 24.17	22.90	0.05	196.	---

arrival, at station YMY, met this criterion and was rejected from Fig. 3.15. I did not apply the rejection criterion to the results from station YCL since a single mean direction does not adequately represent the distribution of polarizations at this station (Fig. 3.6).

Identification of the second split shear wave is made difficult by the arrivals of phases caused by further shear-wave splitting at interfaces between anisotropic media along the raypath (Kaneshima *et al.* 1986a). The amplitudes of these secondary split shear waves depend on the source polarization and the contrast between the fixed polarizations in the media on either side of the interface (Keith and Crampin 1977a; Kaneshima *et al.* 1986a). In heterogeneous but intrinsically isotropic media pervaded by cracks and microcracks aligned in a uniform regional stress field, there will be little contrast in the alignment of the anisotropic symmetry, and hence the polarization directions, across an interface (Crampin 1985a). In an area of complex geology such as the Lleyn Peninsula, in which some of the rock types have anisotropy unrelated to the present stress field, secondary split shear waves may have large amplitudes, and this may account for the scatter in observed delays in Fig. 3.15.

The delays at YRE, YCL and YPE show no obvious temporal change, but at YMY (Table 3.6) there is slight evidence for a decrease in delay with time. Attempts to fit a straight line and an exponential decay curve to the data failed, because of the scatter of the earlier readings, and it is not certain whether the decrease is significant.

3.9 Conclusions

Shear-wave splitting and alignment of polarizations from aftershocks of the North Wales earthquake indicate seismic anisotropy probably due to two causes: weak anisotropy due to stress-aligned microcracks (EDA), and strong anisotropy due to aligned crystals, cleavage cracks and grain boundaries in slate. The microcracks are aligned in the present regional stress field of the British Isles; the slate minerals were aligned by the ancient stresses that caused metamorphism during the Caledonian orogeny. As slate with near-vertical cleavage has similar anisotropic symmetry to vertical or near-vertical parallel microcracks, the dominant polarization alignment caused by the strongly anisotropic slate could appear similar to that caused by EDA, and lead to false estimates of stress direction if the slate is not correctly identified. To interpret correctly the effects of EDA on shear waves, it seems necessary to treat with caution any records of wavetrains that may have passed through slate or any other rock showing intrinsic lithological or crystalline anisotropy (Crampin *et al.* 1984a) with similar symmetry to stress-aligned microcracks.

The tight clustering and great depth of the aftershock foci led to poor coverage of the shear-wave window by the four three-component stations, and spatial variations of shear-wave polarization and delay remain undetermined. Since there are no previous observations of a temporal change in EDA following an isolated intraplate earthquake such as this, we do not know what stress changes to expect. Results from station YMY suggest that if there was any temporal change in delay between split shear-wave arrivals, it might have been a non-linear decrease, which may be

associated with the closing and healing of cracks (Crampin *et al.* 1984b; Smith and Evans 1984). A valid statistical analysis to determine the parameters of the decrease would require more readings, especially from aftershocks within the first month of the mainshock. (Some of the BGS seismic stations were operating at this time, but the recording speed was lower (15/320 ips), causing appreciable loss of the high-frequency part of the shear-wave signal. The records were thus not suitable for delay analysis.)

As there was only one recorded foreshock (Blenkinsop *et al.* 1986), and no instruments within the shear-wave window to record polarization and velocity changes, we cannot say whether the North Wales earthquake was preceded by changes in EDA (Crampin *et al.* 1984b); but given that the estimated return period of an earthquake of this magnitude in Britain is approximately 100 years (Main 1985), stress accumulation and hence changes in crack parameters are probably extremely slow, and could be detected only after many years' monitoring, even if artificial sources were used to supplement the naturally occurring seismic activity.

CHAPTER 4

Shear-wave splitting in the Anza seismic gap, Southern California

4.1 Introduction

The extensive-dilatancy anisotropy (EDA) theory described in Chapters 1 and 3 (Crampin *et al.* 1984b) leads to two predictions about active fault zones: the stress field of an active fault zone causes alignment of fluid-filled microcracks in the surrounding rock; and changes in stress preceding an earthquake can cause changes in microcrack geometry. While evidence of seismic anisotropy interpreted as being due to stress-aligned microcracks has come from studies of shear waves in several active fault zones (see Chapter 3 for summary), and stress directions have been determined from shear-wave polarizations, until now no temporal change in EDA has been observed and related to stress changes. Evidence so far for the anisotropy of fault zones being due to EDA includes the agreement of stress directions predicted from shear-wave polarizations with those predicted by independent means (see e.g. Kaneshima *et al.* 1986a; Buchbinder 1985); the matching of observed shear wavetrains by synthetic seismograms of waves propagating through cracked media (Crampin and Booth 1985); joint inversion of earthquake hypocentres and geological structure including crack-induced anisotropy (Doyle *et al.* 1985); and the absence of other explanations such as source radiation patterns (Booth *et al.* 1985; Crampin *et al.* 1986a), or other types of anisotropy that can pervade all rock types in complex geological areas. This evidence, though compelling, is inconclusive: the most convincing indication of EDA would be the observation of a temporal change in anisotropy around a fault zone.

It is difficult to interpret changes in EDA for earthquake prediction since there are no "case histories" yet of continuous monitoring of EDA throughout the preparation and aftermath of a large earthquake, and stress changes preceding large earthquakes are poorly understood. The Anza seismic gap, along with the Izmit seismic gap on the North Anatolian Fault, Turkey (Crampin *et al.* 1985), the Garm area of Tadzhikistan, USSR (Crampin *et al.* 1986a), several areas in Japan (Kaneshima *et al.* 1986a, b) and other areas where large earthquakes are expected, are being monitored in the hope of building case histories on which future earthquake predictions could be based.

4.2 The Anza seismic gap

The 20 km long Anza seismic gap in the San Jacinto Fault, Southern California, shown in Fig. 4.1 (Thatcher *et al.* 1975; Sanders and Kanamori 1984) is thought to have potential for a magnitude 6.5 earthquake if all of the accumulated strain were released in one event. The fault is believed to be locked by compression normal to its plane at the trifurcation point near the town of Anza (Sanders and Kanamori 1984), where the Buck Ridge and Coyote Creek faults converge on the main San Jacinto Fault.

I examined shear wavetrains from local earthquakes (magnitude $M_L < 4$) recorded by the Anza seismic network of the University of California, San Diego (UCSD) and the U.S. Geological Survey (USGS) (Berger *et al.* 1984). The network consists of ten three-component sets of 2-Hz Geo Space HS10 seismometers, digitally telemetered and recorded at 250 samples per second per channel. The seismometers have a broadband response up to 100 Hz; their output is passed

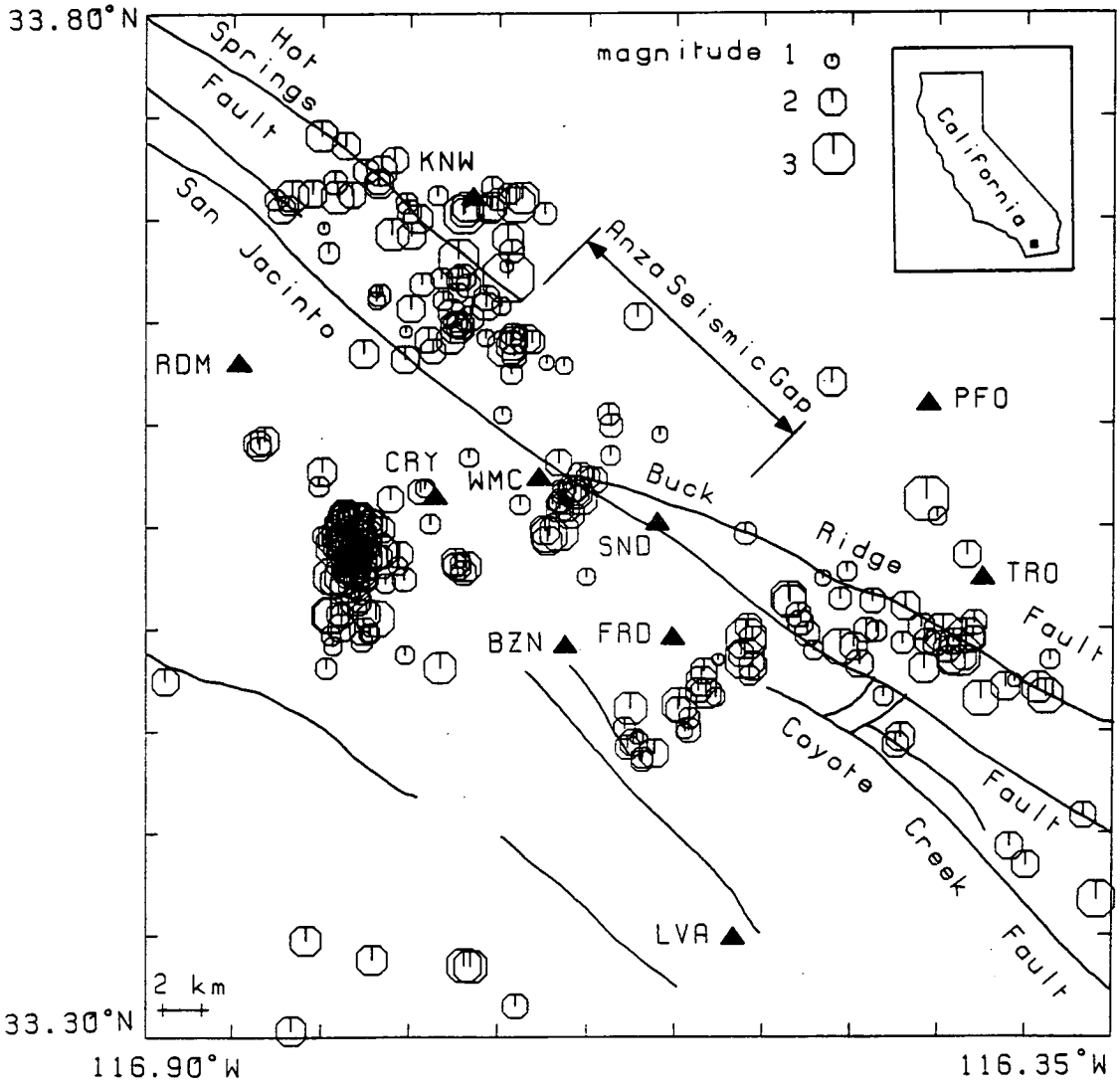

Fig. 4.1 Seismicity around the Anza seismic gap between June 1983 and October 1985. Earthquakes are shown as circles with radius proportional to magnitude. Triangles are stations of the UCSD-USGS Anza network.

through a low-pass filter with corner frequency 62.5 Hz before being digitized. The station positions are shown in Fig. 4.1. The stations are sited on outcrops of granite of the Southern California Batholith (Sharp 1967) which extends on both sides of the San Jacinto Fault.

Earthquake epicentres in this area for the period June 1983 to October 1985 are also shown in Fig. 4.1 (Fletcher *et al.* 1986a). They were located by USGS staff using HYPOINVERSE (Klein 1978) with the velocity model of Hartzell and Brune (1979), listed in Table 4.1. Estimated location errors are ±1.5 km in horizontal co-ordinates and ±1 to ±3 km in depth. Some earthquakes, especially those in the north of the seismic gap, are up to 20 km deep, indicating that conditions for brittle fracture extend to unusual depth for the San Andreas fault system. Fletcher *et al.* (1986a) suggest that localized low heat flow (as in North Wales, Chapter 3) or the mineral composition of the Southern California Batholith may be responsible for the brittleness of the rock at depth.

Almost all records of shear waves received within the shear-wave window (see Chapter 1) from these earthquakes showed splitting, typical of shear-wave propagation through anisotropic media. Sample seismograms are shown in Figs. 4.2 and 4.3. Following the examples of anisotropy in earthquake zones cited in Chapter 3, we start with the hypothesis that the shear-wave splitting is caused by EDA. The granite beneath the Anza network shows no obvious alignment of crystals, and although there are no velocity data for this granite, other uniform granites have shown no appreciable anisotropy in the absence of aligned cracks (Nur and Simmons 1969;

Table 4.1 (a) Velocity model used in hypocentre location.

Layer	P-wave velocity km/s	S-wave velocity km	Depth to top of layer km
1	2.50	1.44	0.0
2	5.50	3.14	1.0
3	6.30	3.63	5.0
4	6.80	3.92	28.4

(b) Station positions

station	latitude °N	longitude °E	height m
PFO	33.609	-116.456	1280
KNW	33.710	-116.715	1463
FRD	33.495	-116.602	1170
CRY	33.564	-116.736	1141
SND	33.551	-116.611	1390
BZN	33.491	-116.663	1311
RDM	33.629	-116.847	1394
TRO	33.524	-116.425	2657
WMC	33.573	-116.678	1224
LVA	33.348	-116.567	1451

Fig. 4.2 Typical three-component seismograms of P-wave and shear-wave arrivals at (a) station WMC, from an earthquake at 14.0 km depth, 9.4 km from the station at azimuth N 337°E; (b) station KNW, from an earthquake at 9.33 km depth, 8.4 km from the station at azimuth N 159°E. The polarization diagrams are numbered to correspond with the time intervals marked above the seismograms, and show P-wave and shear-wave first arrivals in three 0.08-second long "windows" of particle motion, in three orthogonal planes: from top to bottom, vertical radial, vertical transverse, and horizontal (labelled Up, Down, Towards and Away from the epicentre, and Left and Right of the radial direction away from the epicentre). Ticks on the particle displacements are every 0.004 s, and a gain factor (x 1, x 2, etc.) is shown above each set of polarization diagrams. Shear-wave splitting is seen in the horizontal plane; where the arrivals of both split shear-waves are marked with arrowheads.

Fig. 4.2 (a)

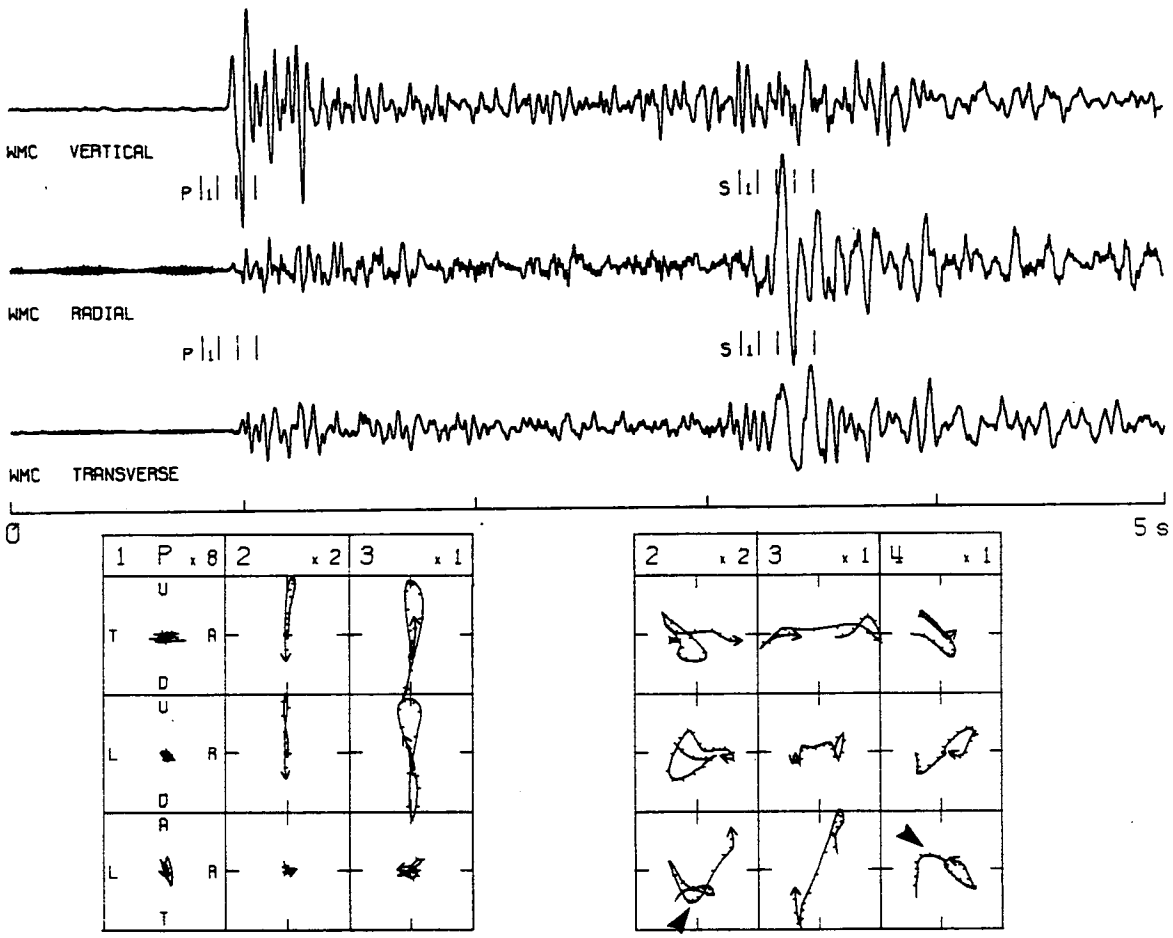
WMC VERTICAL
P
S
WMC RADIAL
P
S
WMC TRANSVERSE
0
5 s
1 P x 8
2 x 2
3 x 1
U
T
R
D
L
A
2 x 2
3 x 1
4 x 1

Fig. 4.2 (b)

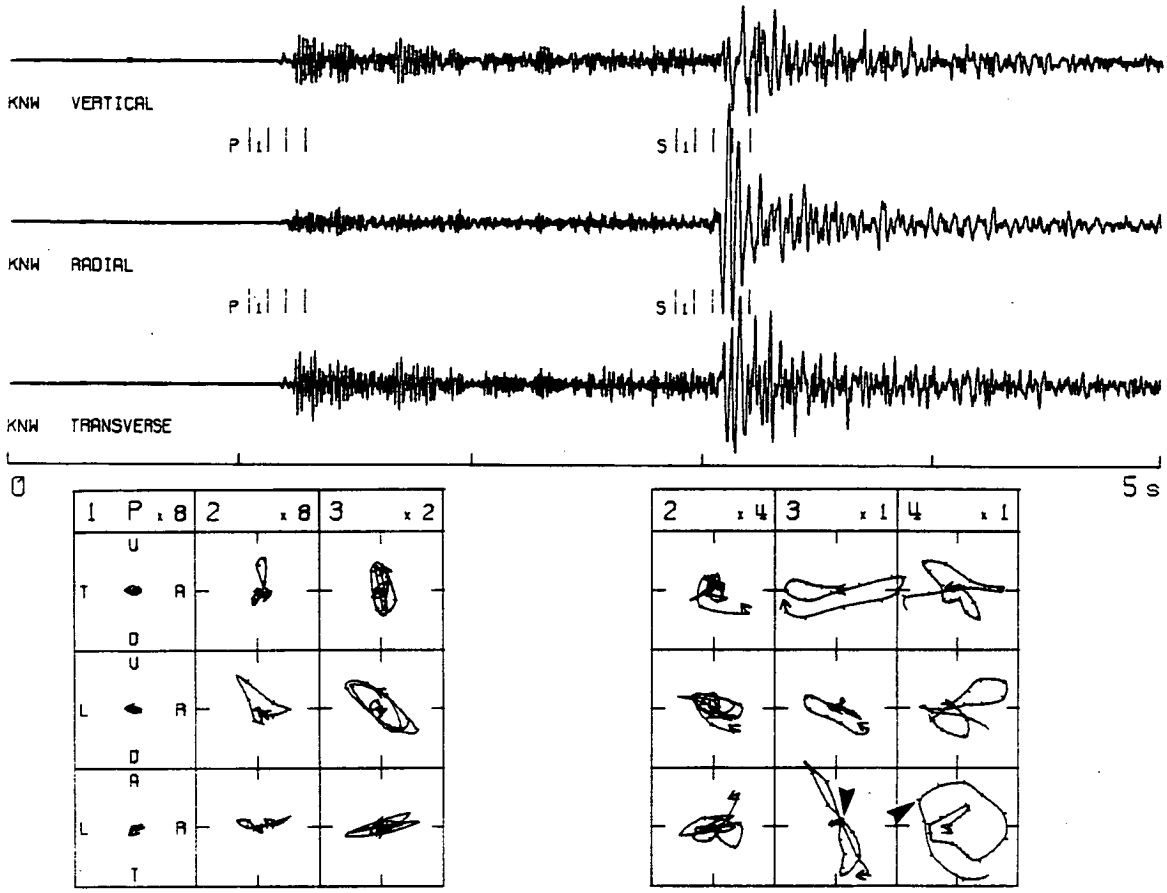
KNW VERTICAL
P
S
KNW RADIAL
P
S
KNW TRANSVERSE
0
5 s
1 P x 8
2 x 8
3 x 2
2 x 4
3 x 1
4 x 1
U
T
R
D
U
L
R
D
A
L
R
T

Fig. 4.3 Examples of split shear-waves within the shear-wave window at nine stations. Notation as in Fig. 4.2.

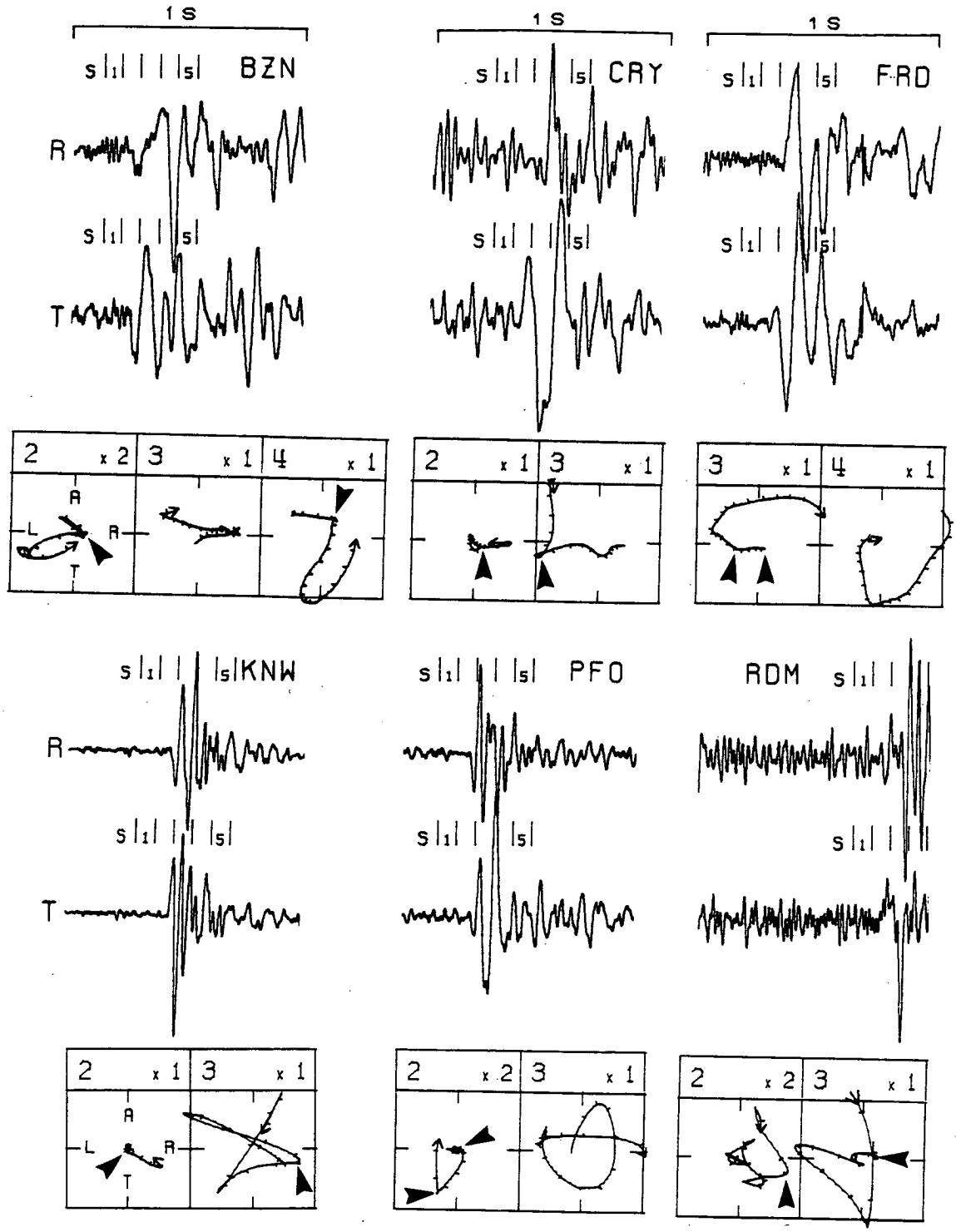

Fig. 4.3 (cont.)

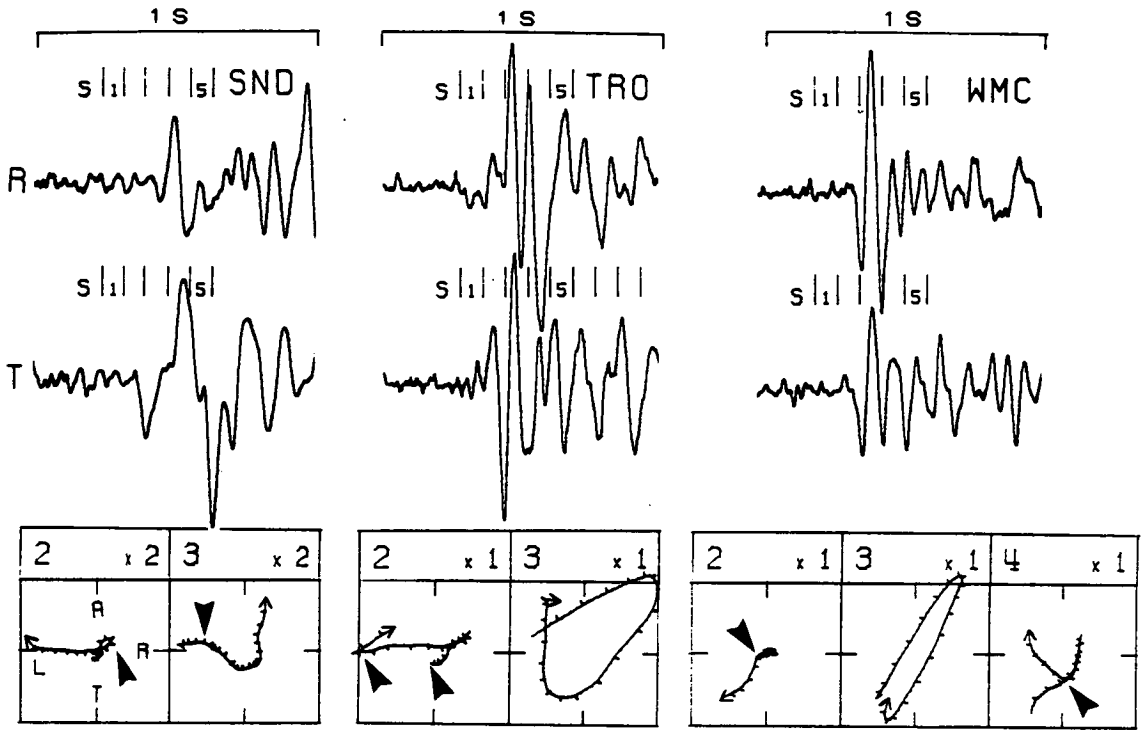

Babuška 1984); so it is unlikely that the observed shear-wave splitting is due to crystalline anisotropy. Heterogeneity along the raypaths should cause no more than ±10° scatter of the shear-wave polarizations (Cormier 1984).

Fig. 4.4 shows the theoretical behaviour of waves propagating through a rock containing vertical parallel microcracks with parameters appropriate to the behaviour of shear waves in the Anza area. Effective elastic constants for the cracked medium, calculated from the formulae of Hudson (1980, 1981; Crampin 1984b) are listed in Table 4.2. The uncracked rock matrix has the velocities of layer 3 of the Hartzell and Brune (1979) velocity model, and the crack density of 0.015 gives delays between split shear waves of up to 4 ms/km, similar to the observed values.

4.3 Processing

I inspected all records from stations within a nominal shear-wave window of 45°, to be certain of including all arrivals within the actual shear-wave window of each station. The velocity model of Hartzell and Brune (1979) includes a low-velocity surface layer, which could effectively widen the shear-wave window (Booth and Crampin 1985).

The shear-wave arrival from each three-component record was plotted as polarization diagrams in three mutually orthogonal sections, and the horizontal polarization of the first-arriving split shear wave and the delay between the two split shear waves were measured from the horizontal section. I rejected a number of arrivals within the nominal shear-wave window, which were irregular and emergent and did not show clear polarizations, probably owing

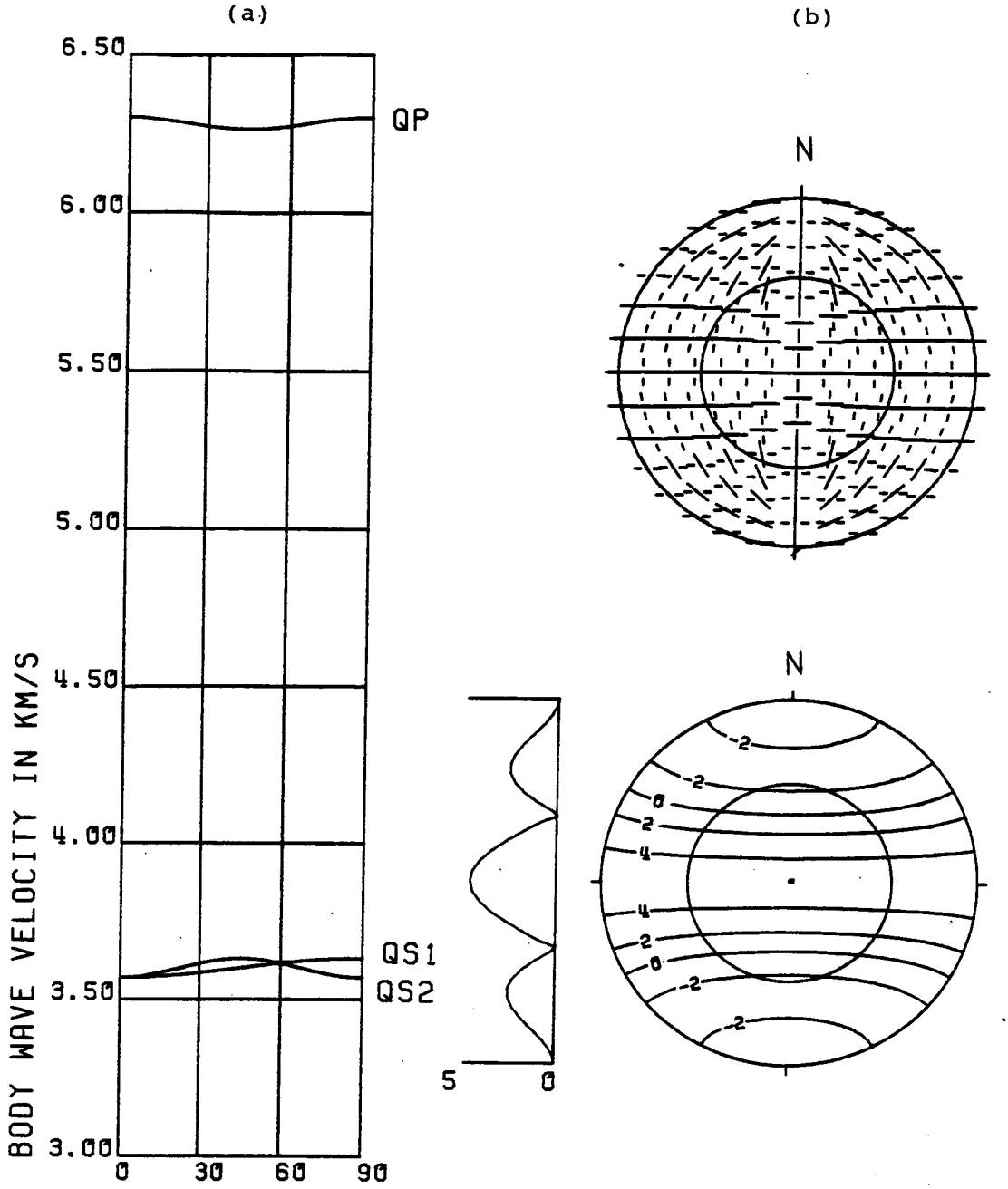

Fig. 4.4 Theoretical behaviour of seismic waves in rock containing parallel liquid-filled microcracks. (a) Velocity variations with propagation directions from normal (0°) to parallel (90°) to the cracks with crack density 0.015 and negligible aspect ratio (0.0001). The uncracked isotropic matrix has velocities V_p = 6.3 km/s and V_s = 3.63 km/s. The shear wave QS1 is polarized perpendicular, and QS2 parallel, to the plane of incidence through the crack normals. (b) Horizontal equal-area projections out to 90° of the polarizations (top) and time delays (bottom) of split shear waves passing through the cracked rock in (a), with the cracks striking east-west. The inner circle represents incidence angle 45°. The solid lines in the polarization plot are horizontal projections of the polarizations of the leading (faster) split shear waves; the broken lines are polarizations of the slower split shear waves. The delays are contoured in milliseconds per kilometre path length. To the left is a north-south section of the contour plot.

Table 4.2 Elastic parameters of cracked medium with crack density 0.015, aspect ratio 0.0001, used to calculate model velocities and polarizations in Fig. 4.3. The uncracked medium is isotropic with the velocities of layer 3, Table 4.1.

density=2.64g/cm^3	elastic constants (units 10^{10}N/m^2)
c_{1111}	10.4769
c_{3333}	10.4797
c_{1133}	3.5190
c_{1313}	3.3628
c_{2323}	3.4800

Table 4.3 Mean polarizations of shear-wave first arrivals at nine Anza stations, with standard deviations and mean resultant length (the mean resultant length is a measure of alignment of polarizations in one direction: values near 1 indicate strong unimodal alignment; values near 0 indicate no alignment i.e. a uniform (random) distribution of polarizations).

Station	Number of readings	Mean polarization degrees	Standard deviation degrees	Mean resultant length
BZN	7	10.8	18.8	0.81
CRY	9	175.0	30.8	0.56
FRD	4	12.5	9.9	0.94
KNW	41	141.3	12.6	0.91
PFO	1	125.0	----	----
RDM	6	152.0	29.8	0.58
SND	6	25.7	9.8	0.94
TRO	10	18.0	39.3	0.39
WMC	29	179.6	12.4	0.91

to interactions with the steep local topography, which can cause scatter up to ±20° (Booth *et al.* 1985). In some records, shear wave polarizations were obscured by the P-coda. In many records where the first shear-wave arrival was clear, the second was ambiguous and the delay was difficult to measure. This may be due to the multiple splitting described in Chapter 3, or may possibly be because the slower shear wave is generally attenuated more than the faster one (Crampin 1984b), or the source radiation did not excite the slower shear wave polarization as strongly as the faster.

When the polarizations were plotted on equal-area projections for each station, some at stations BZN, FRD, PFO, RDM, SND and TRO with large incidence angles clearly disagreed with the trend of those from small incidence angles, presumably because the arrivals were outside the actual shear-wave window of that station. Shear-wave windows of 35° - 37° were set for all stations except KNW, WMC and CRY to eliminate these readings. I rejected a total of 166 polarizations during processing, including all within the shear-wave window of station LVA.

4.4 Polarization results

The polarizations of 113 leading shear waves at nine Anza stations, from 93 events, are shown in Fig. 4.5, and as rose diagrams in Fig. 4.6. Coverage of the shear-wave window at each station is limited, but at all stations except PFO and TRO there is some consistent alignment. This alignment is approximately north-south for stations BZN, CRY, FRD and WMC, NNE-SSW for station SND and northwest-southeast for stations KNW and RDM. Circular mean polarizations, standard deviations and mean resultant lengths

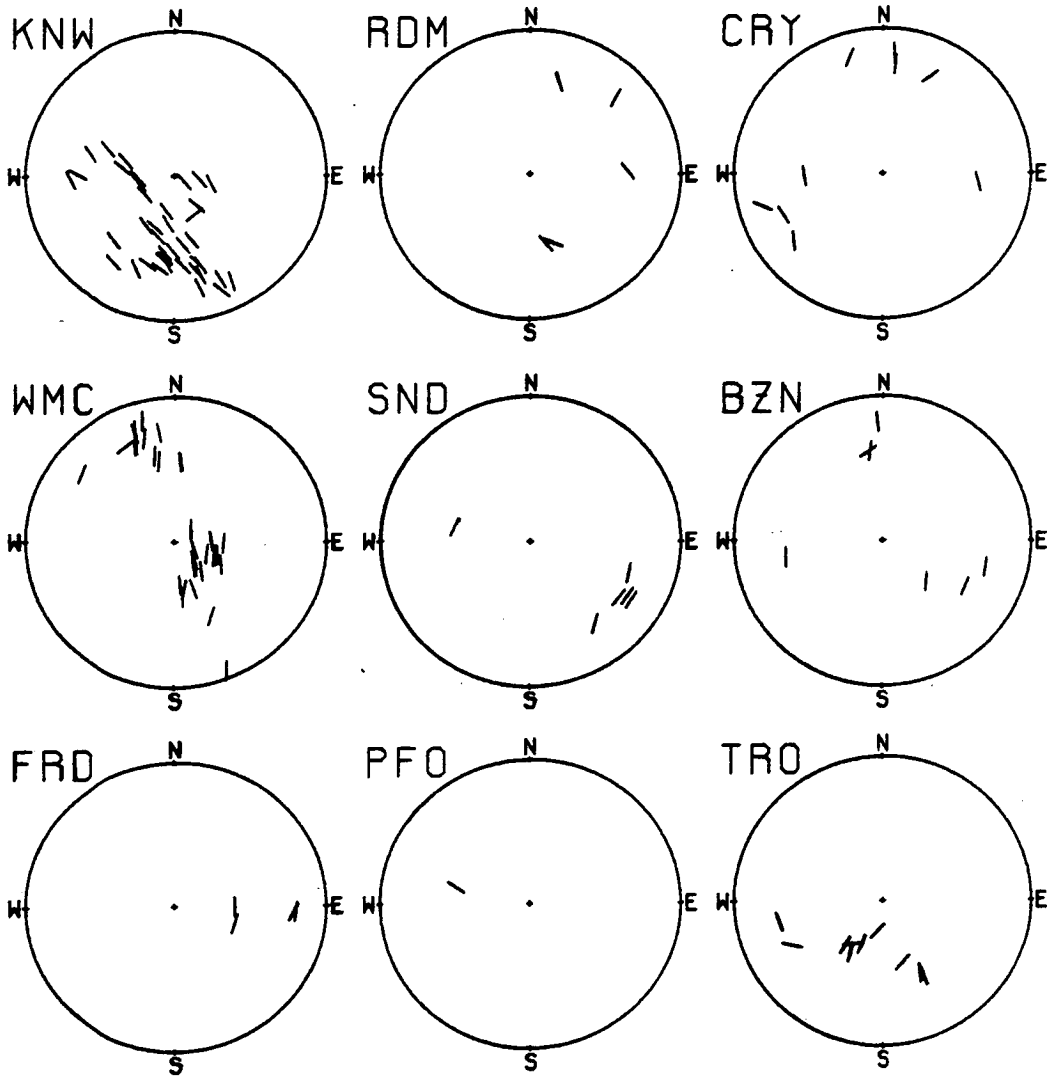

Fig. 4.5 Horizontal projections of the polarizations of shear-wave first arrivals at nine Anza stations, shown in equal-area projections of the lower hemisphere of directions out to 45° beneath each station.

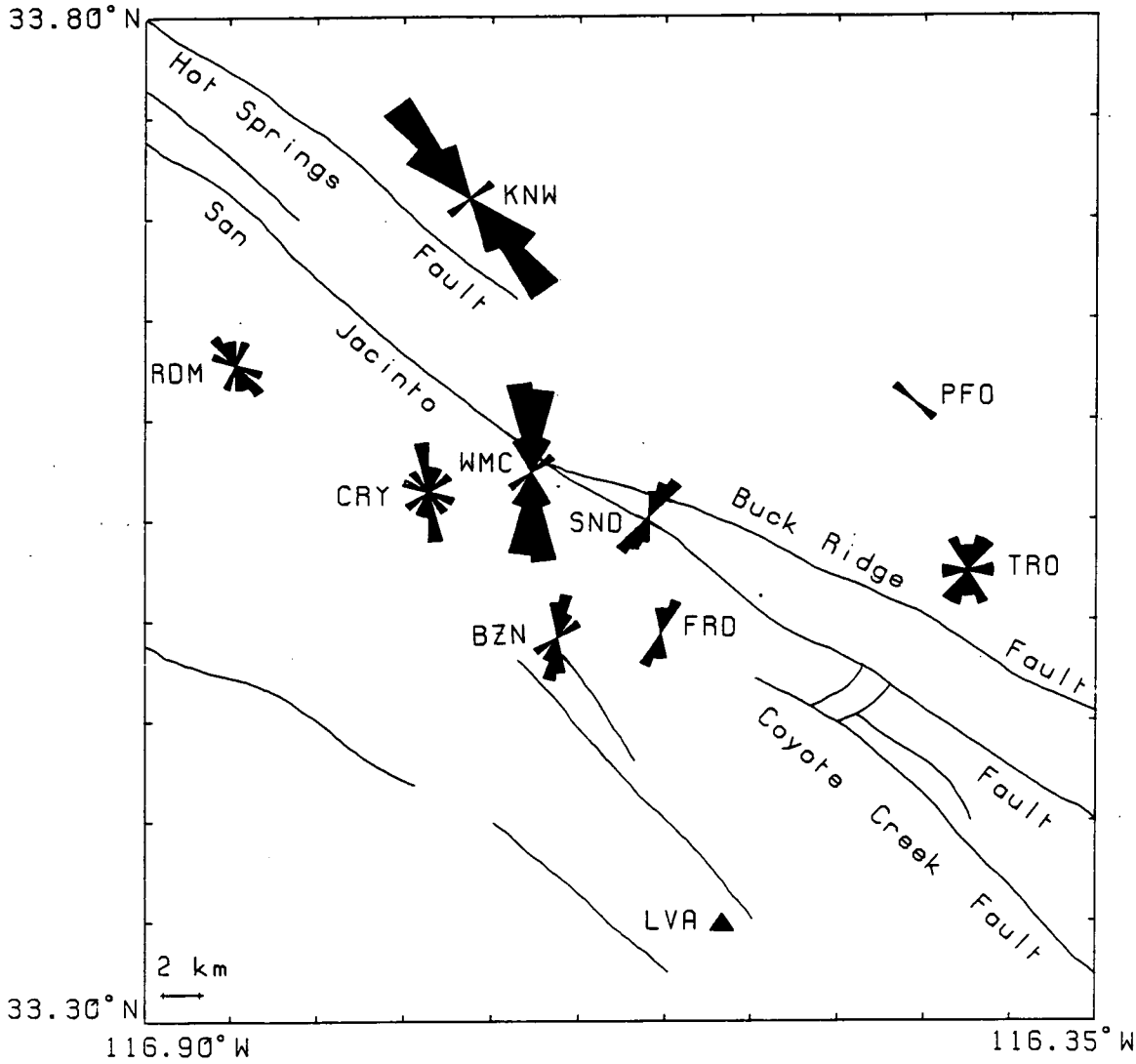

Fig. 4.6 Equal-area rose diagrams of the polarizations of shear-wave first arrivals at nine Anza stations.

for each station (Mardia 1972) are listed in Table 4.3.

4.5 Comparison with source polarizations

In an isotropic crust the observed shear-wave polarizations would be those radiated from the source mechanism, modified by interaction with internal interfaces (Cormier 1984) and topography. In an anisotropic crust any radiated polarization which is not perpendicular to the polarization of the faster shear wave will excite energy in the faster shear wave, which will be observed as a first arrival. I determined double-couple source mechanisms for 22 earthquakes from P-wave first motions recorded by the Anza network and nearby stations of the California Institute of Technology - USGS Southern California Network (SCARLET), and compared the theoretical and observed shear-wave polarizations. The locations and mechanisms of the events used are listed in Table 4.4 and mapped in Fig. 4.7, and the fault-plane solutions and corresponding theoretical shear-wave radiation patterns are shown in Fig. 4.8 with the observed polarizations superimposed.

I have not attempted to compare in detail the theoretical and observed polarizations because the unknown errors in both, mentioned in Chapter 3, might bias the results; but some general trends are clear. The observed polarization at each station (disregarding polarity) is almost always parallel to the dominant direction of shear-wave polarization at that station (Fig. 4.6). For events 1, 3, 12, 13, 14 and 17, and station KNW for event 22, the source polarization is approximately parallel to the observed polarization at each station. Most of the other observed polarizations deviate from the source polarizations towards the

Table 4.4 Focal parameters of 22 events, numbered to correspond to the fault-plane solutions in Fig. 4.7. Strike, dip and rake are after the convention of Aki and Richards (1980).

	Date and Time						Location						Mechanism		
							Latitude		Longitude		Depth	M_L	Strike	Dip	Rake
No	Y	M	D	H	M	S	°N	min	°E	min	km		N°E	°	°
1	83	10	2	13	23	21.17	33	38.89	-116	43.48	13.00	1.8	37	64	11
2	83	10	21	20	53	36.99	33	39.10	-116	42.96	14.00	1.9	102	70	90
3	83	10	23	10	57	4.68	33	38.99	-116	43.41	14.01	1.6	63	52	23
4	84	3	16	19	53	21.40	33	42.42	-116	41.46	16.80	2.8	317	89	-156
5	84	5	1	13	7	52.95	33	42.20	-116	43.16	17.51	2.2	160	60	-90
6	84	5	10	22	10	11.31	33	34.86	-116	40.00	11.95	2.0	300	89	-90
7	84	7	2	19	8	35.21	33	28.43	-116	35.11	10.72	2.3	36	64	-46
8	84	7	2	20	13	27.58	33	33.52	-116	39.96	10.75	2.1	62	90	-20
9	84	7	7	22	35	7.66	33	37.89	-116	45.17	14.51	2.1	121	90	-160
10	84	7	8	23	22	48.79	33	43.05	-116	46.09	16.59	2.2	16	80	80
11	84	7	23	9	6	44.01	33	29.45	-116	29.90	12.25	2.1	122	70	-169
12	84	8	15	9	14	56.14	33	38.88	-116	43.38	13.35	1.8	70	40	43
13	84	8	30	4	12	39.68	33	28.25	-116	23.59	11.75	2.4	34	80	31
14	84	8	30	4	21	11.60	33	27.99	-116	23.32	12.09	2.7	20	90	10
15	84	9	11	12	48	36.47	33	29.84	-116	26.83	10.04	2.9	113	60	90
16	84	10	30	16	42	4.49	33	40.30	-116	43.25	15.20	2.0	6	80	180
17	84	11	14	6	48	46.90	33	33.98	-116	39.42	11.00	2.0	260	80	90
18	84	12	1	8	6	39.05	33	32.74	-116	40.32	10.43	2.7	172	80	180
19	84	12	4	15	42	19.59	33	42.29	-116	42.33	17.21	2.1	260	40	158
20	85	1	27	1	58	8.18	33	30.86	-116	32.14	10.97	2.7	138	60	171
21	85	1	27	11	52	10.81	33	33.33	-116	39.61	11.19	2.1	173	90	180
22	85	1	27	20	2	57.46	33	38.21	-116	41.77	13.20	2.8	303	58	168

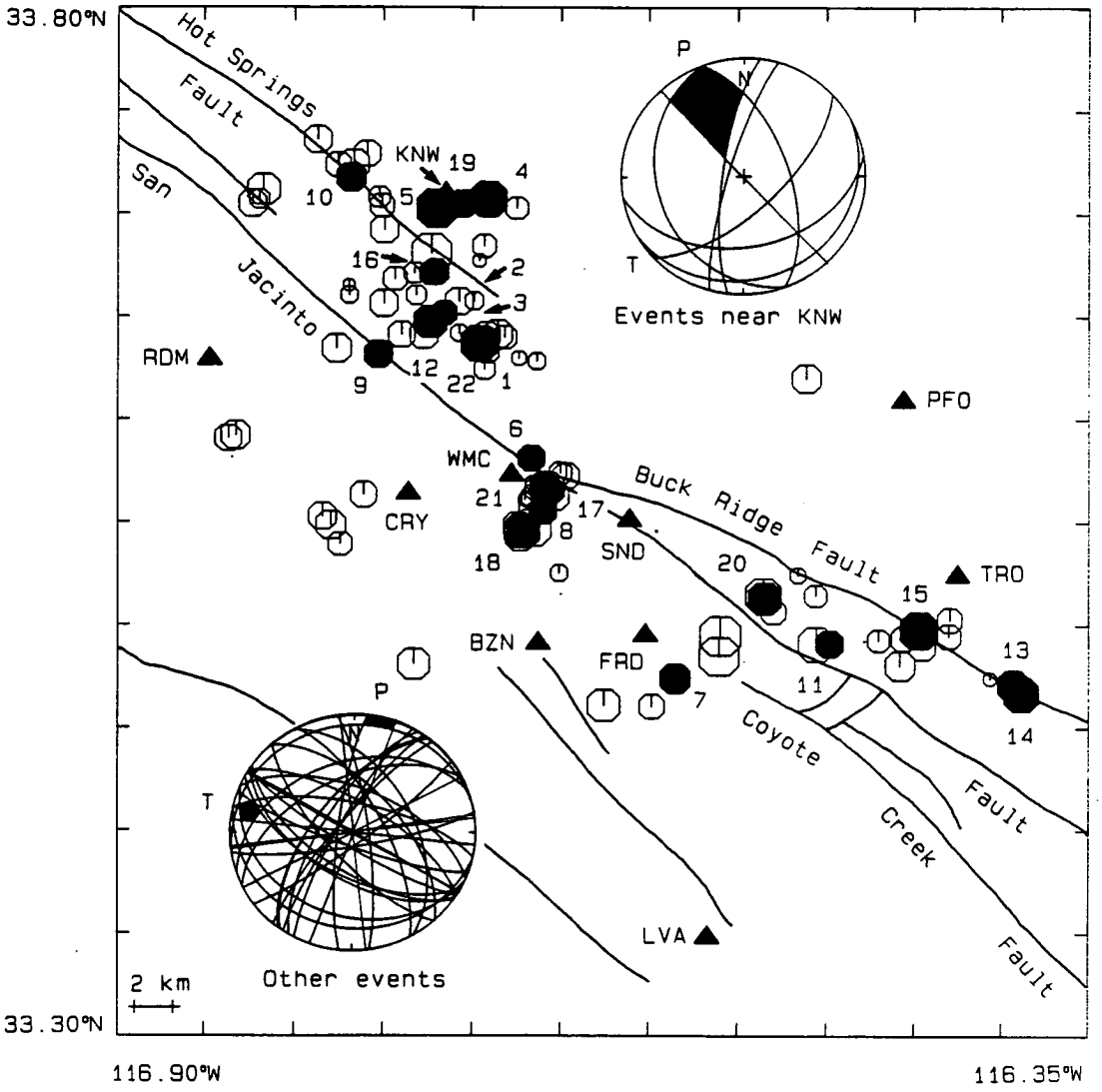

Fig. 4.7 Map of the Anza area showing earthquakes used in shear-wave analysis. Notation as in Fig. 4.1. Numbered shaded events correspond to numbered fault plane solutions in Fig. 4.8. The inserts are: top right, superimposed nodal planes of mechanisms of four earthquakes near station KNW (epicentres numbered 4, 5, 10 and 19); and bottom left, superimposed nodal planes of the remaining 18 earthquakes. The common areas of compression and tension in the inserts are shaded. Note the small common area of tension in a horizontal direction in the top right insert.

Fig. 4.8 Fault-plane solutions and theoretical shear-wave radiation patterns (out to incidence angle 45°) of 22 earthquakes in the Anza area, numbered to correspond with the epicentres on the map in Fig. 4.7. The observed polarizations of the first-arriving shear waves from these earthquakes at the named stations are shown as superimposed arrows. The plots are equal-area projections of the upper focal hemisphere, and in the fault-plane solutions, filled dots represent compressions, open dots dilatations, and crosses, P and T axes.

Fig. 4.8

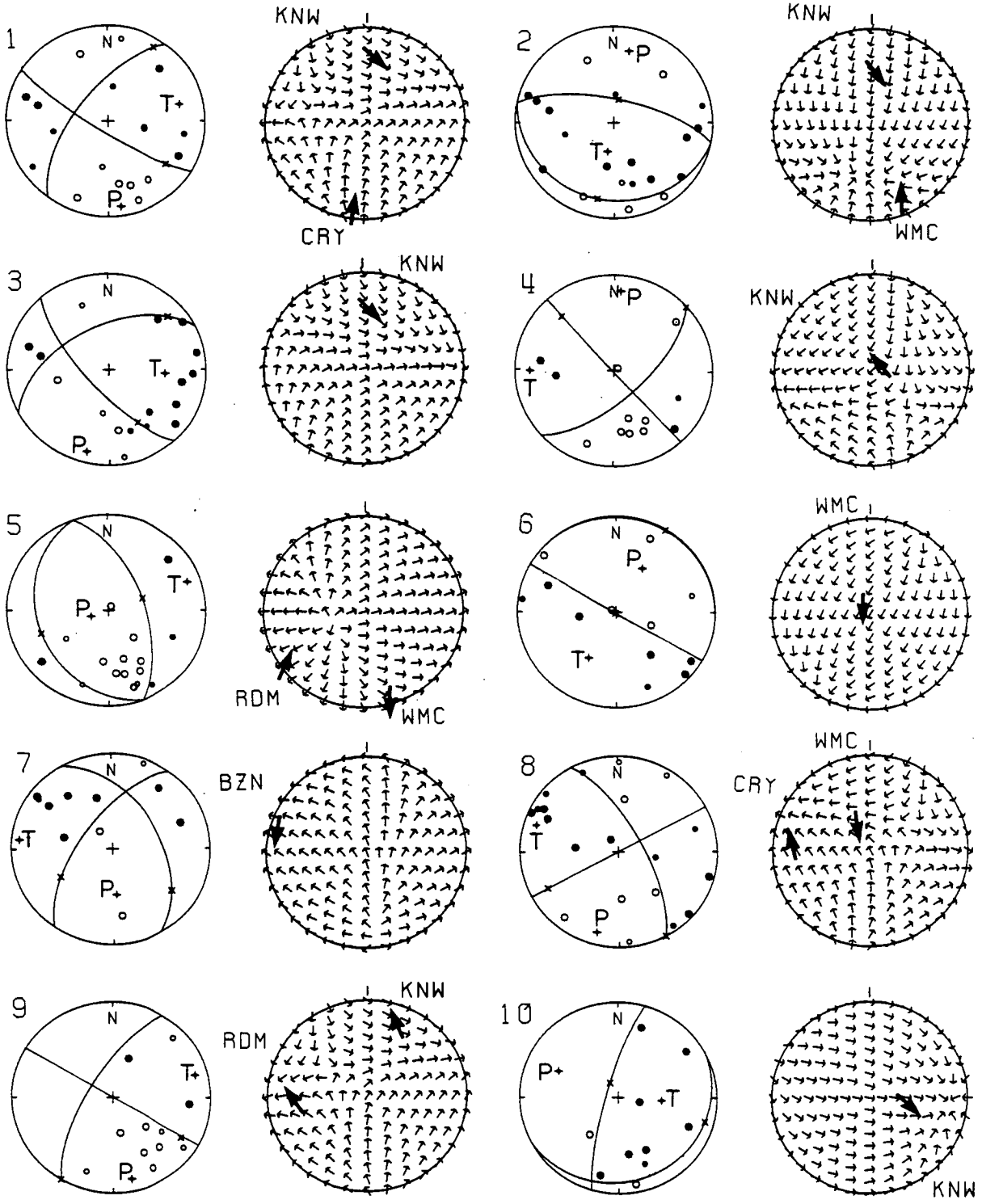
1
N
T
P
KNW
CRY
2
N
P
T
KNW
WMC
3
N
T
P
KNW
4
N
P
T
KNW
5
N
T
P
RDM
WMC
6
N
P
T
WMC
7
N
T
P
BZN
8
N
T
P
WMC
CRY
9
N
T
P
RDM
KNW
10
N
P
T
KNW

Fig. 4.8 (cont.)

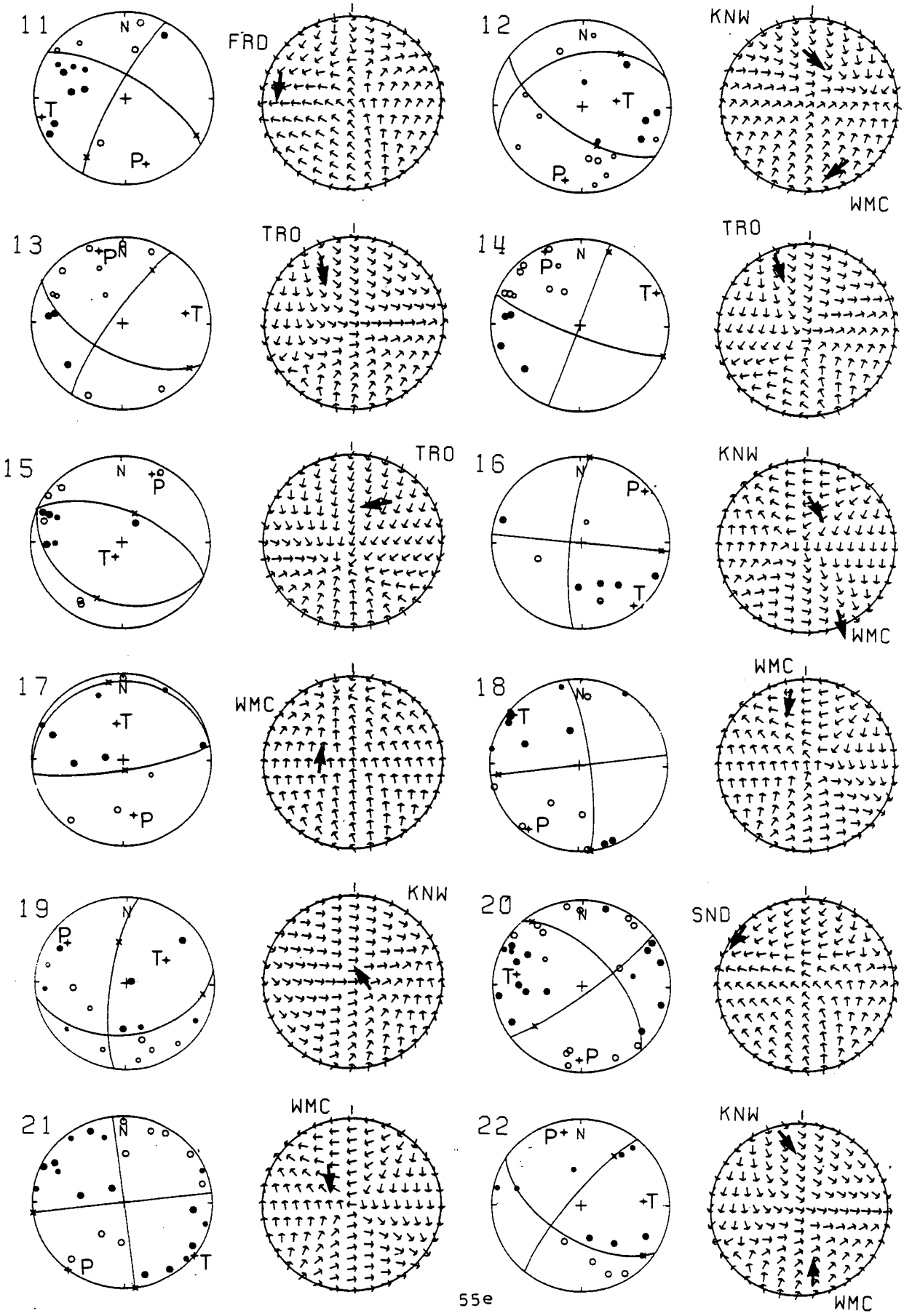
11
N
T
P
FRD
12
N
T
P
KNW
WMC
13
N
P
T
TRO
14
N
P
T
TRO
15
N
P
T
TRO
16
N
P
T
KNW
WMC
17
N
T
P
WMC
18
N
T
P
WMC
19
N
P
T
KNW
20
N
T
P
SND
21
N
P
T
WMC
22
N
P
T
KNW
WMC

dominant direction of shear-wave polarization at their respective stations (events 2, 4, 6, 7, 9, 10, 11, 16-21 and station WMC for events 5, 8 and 22). Station RDM for event 5 has an observed polarization near-parallel to the source but perpendicular to the (ill-defined) general trend of polarizations at that station (Fig. 4.6), while the observed polarization at station TRO for event 15 departs appreciably from the source polarization.

These results suggest that at least some of the observed polarizations are not those expected from an isotropic structure. The relation between the orientation of fault planes (and hence the source polarizations) and the overall stress field which aligns cracks is not straightforward, and some coincidence of source and observed polarization may be expected from a medium containing EDA.

For event 5, the source polarization is perpendicular to the probable polarization of the faster shear wave travelling to station RDM, so it is possible that the faster shear wave has not been excited and the observed first arrival is that of the slower, perpendicularly polarized shear wave. The observed polarization at station TRO from event 15 may have been scattered by the steep topography around the station site at the summit of Toro Peak.

Source and observed *polarities* disagree in many cases, probably because the shear-wave first break is small compared to the backswing in these records, and is obscured by the P-coda.

4.6 Interpretation of polarizations

The shear-wave splitting, polarization alignment and comparison with source polarizations have all given evidence of anisotropy beneath the Anza network, which we now interpret in terms of the

alignment of microcracks in the rock by local or regional stress fields. The regional stress field is north-south compression (Savage *et al.* 1981): microcracks in this stress field will be aligned vertically parallel and striking in the direction of compression (Crampin 1978, 1984b, 1985b). The observed polarizations at stations BZN, CRY, FRD and WMC show north-south alignment, probably caused by this regional stress field. Stations TRO and RDM are on mountaintops, surrounded by steep irregular topography which may be scattering the shear waves. Station RDM lies less than 100 m northeast of a contact between the granite and an older schist, which may add to the scattering. Although the northwest-southeast trend of shear-wave polarizations at RDM is approximately parallel to both the contact and the cleavage of the schist (Sharp 1967), it is unlikely that the polarizations are due to crystalline anisotropy in the schist since most raypaths to the station are from the east or northeast (Fig. 4.5), and may not cross the contact.

The polarization nearly normal to the San Jacinto Fault at station SND may be caused by microcracks aligned by the compression normal to the fault, which is presumed to be responsible for the seismic gap (Sanders and Kanamori 1984), though it is possible that macrofractures or gouge along the fault zone itself (Sharp 1967), or the topography of the fault scarp, are affecting the shear waves. Most of the arrivals are near the edge of the assumed shear-wave window of 35° and have polarizations transverse to the raypath, which may be a sign that they are outside the true shear-wave window of the station (Evans 1984a). More polarizations from a range of incidence angles within the shear-wave window would

be required to confirm this.

The uniform northwest-southeast polarizations at station KNW appear to be significantly different from those at other stations in the Anza network. This may be due to perturbation of the polarizations by topography (as at one station in the Turkish Dilatancy Project network, Chen *et al.* 1986; Booth *et al.* 1985; Booth and Crampin 1985; Crampin 1986a); local anisotropy caused by aligned fractures in the Hot Springs Fault zone, through which many of the raypaths to the station pass; or anisotropy caused by microcracks aligned in a northwest-southeast stress field over a larger region. The polarizations at KNW show very little scatter, suggesting that the cause is uniform anisotropy beneath the recording site rather than an isolated anomaly in the Hot Springs Fault zone or a topographic effect. Superimposed nodal planes (see Chapter 3) from four earthquakes near station KNW (Fig. 4.7, top) show a poorly-constrained common area of compression in the northwest quadrant, which may indicate that the dominant stress driving these events is northwest-southeast: in contrast to superimposed nodal planes from other locations (Fig. 4.7, bottom), which show north-south compression. The poorly defined northwest-southeast alignment of polarizations at station RDM may also be caused by this stress field, though a northwest-southeast stress field extending as far as RDM would be difficult to reconcile with the regional tectonics, right-lateral strike-slip with minor thrusting on a northwest-southeast trending fault (Sharp 1967).

4.7 Temporal changes

I looked for evidence of a change in stress affecting the crack geometry over the 29-month recording period. A change in stress direction would cause a change in crack orientation, which would affect shear-wave polarizations, while a change in stress intensity would cause a change in crack size or density, which would affect delays between split shear waves (Crampin *et al.* 1984b; Crampin and Booth 1985; Crampin 1986a). Since a change in stress direction is not necessary before an earthquake, it seems that a change in delay will be the more likely precursor.

Polarizations and delays are generally so scattered that statistical analysis of large numbers of readings, well-distributed over time, is necessary to give reliable indications of temporal change. Only stations KNW and WMC had enough readings to justify such analysis. A few readings of lesser quality, rejected from the polarization alignment analysis, were included here to increase the size of the dataset. One reading from KNW with polarization perpendicular to the general trend at that station was rejected as being the arrival of the slower shear-wave component. Delays were normalized by hypocentral distance, and polarizations and normalized delays were plotted against time. As a precaution against subjective bias, my readings of delay were checked by an independent observer. His results did not differ significantly from mine.

Over the 29-month recording period, neither station showed significant change in shear-wave polarizations, and WMC showed no significant delay change, but at KNW delays appeared to increase with time. I fitted a straight line to the readings by least

squares, and found the rate of increase to be $1.6 \pm 0.7 \times 10^{-3}$ ms/km day, significant at 95% (Fig. 4.9a).

Theoretical delays between split shear waves from a medium containing vertical parallel microcracks show a broad maximum across the centre of the focal hemisphere parallel to the strike of the cracks, with gradients on either side (Fig. 4.4b). In the previous section I inferred that vertical parallel microcracks strike north-south at station WMC and northwest-southeast at KNW (see Table 4.3). At WMC all of the observed shear waves arrive within the broad maximum of theoretical delays, but some of the KNW observations lie in the area of the focal sphere where the theoretical delay is changing appreciably with incidence angle (near the southwest edge of the circle in Fig. 4.9a). Although these observations show no decrease in delay with incidence angle, they show a much larger increase in delay with time (Fig. 4.9b) than all of the readings taken together (Fig. 4.9a), while the readings within the broad maximum of theoretical shear-wave delays show no significant change with time (Fig. 4.9c). The readings were divided into two sets according to the incidence angle of the straight raypath to a vertical plane approximately parallel to the cracks. I chose the strike of the plane and the limiting incidence angle to maximize the correlation coefficient of the increase in delay with time of the readings with smaller incidence angles. The strike of the plane is N 318°E, which is within one standard deviation of the mean polarization direction in Table 4.3. Polarizations and delays of split shear-waves from earthquakes on either side of the plane are listed in Table 4.5. The events with incidence angle less than 75.5° (measured from normal to the crack

Fig. 4.9 (a)

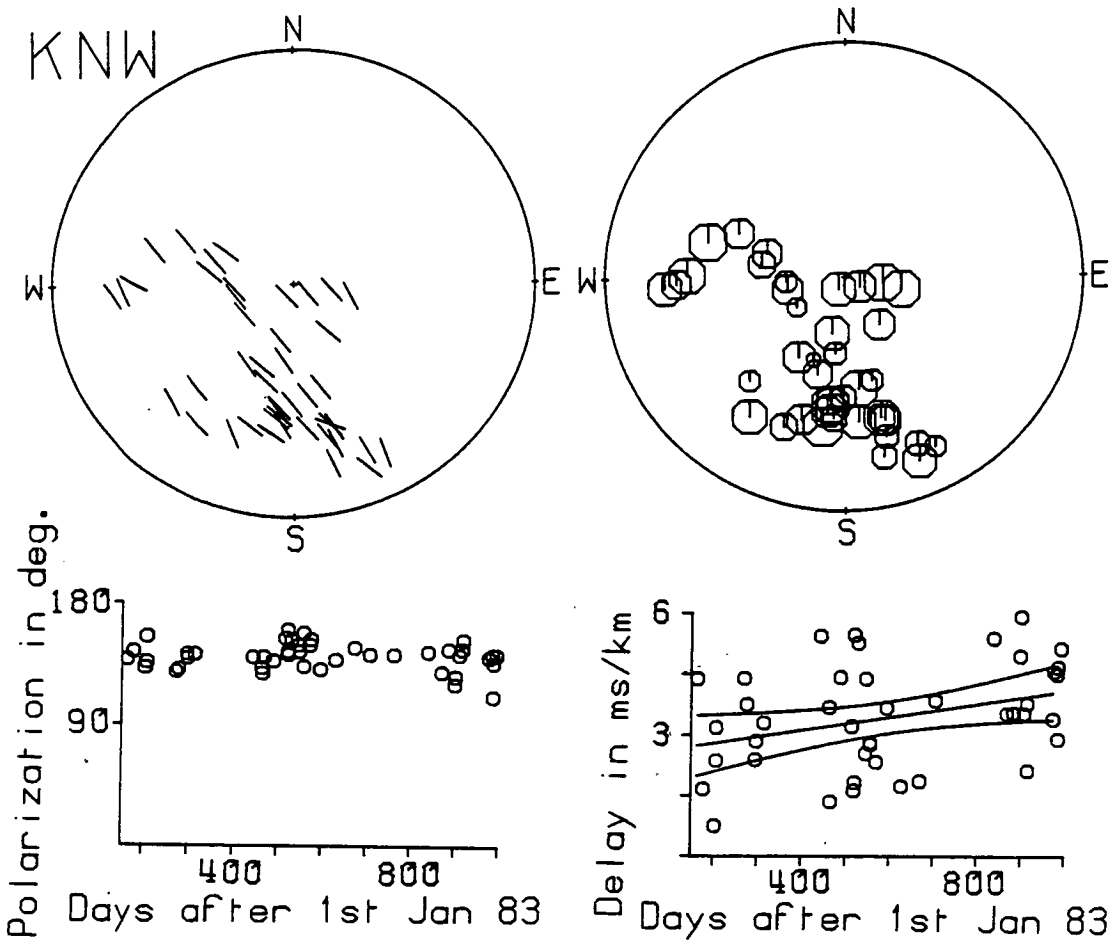

Fig. 4.9 Shear-wave polarizations and delays beneath station KNW from June 1983 to October 1985 from first arrivals from (a) all earthquakes with readable shear-wave delays at station KNW; (b) events with straight raypaths to KNW making incidence angles less than 75.5° from the normal to a vertical plane striking N 318°E; (c) events with straight raypaths to KNW making incidence angles greater than 75.5° from the normal to this plane. Upper figures show equal-area projections out to 45° of the lower hemisphere of directions beneath KNW for polarizations (left-hand figure) and time delays normalized by length of raypath (right-hand figure) with the area of the symbol proportional to the delay. Lower figures are graphs showing the corresponding quantities plotted against time with, for (a) and (b), the least squares fit and 95% confidence limits. The polarizations are measured in degrees East of North and the time delays are normalized in milliseconds per kilometre.

Fig. 4.9 (b)

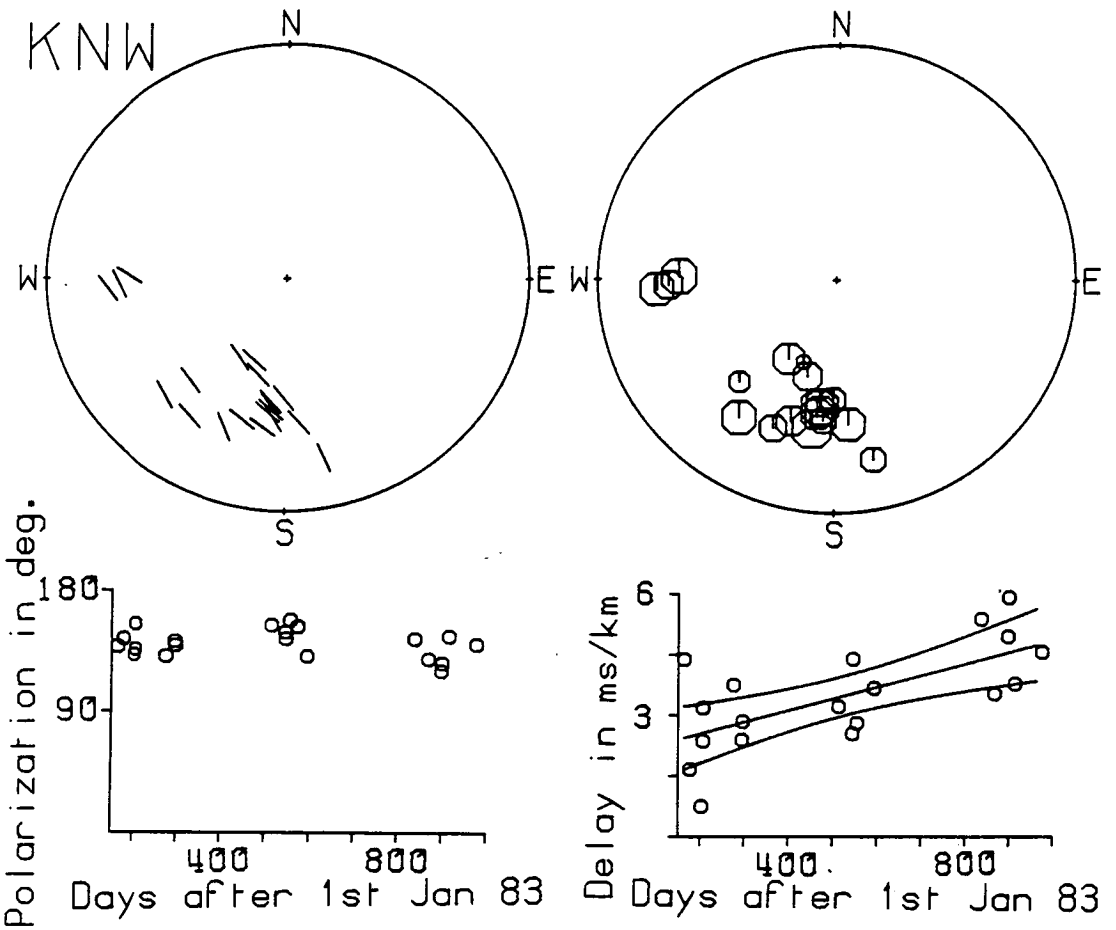
KNW
N
W
E
S
N
W
E
S
Polarization in deg.
180
90
400
800
Days after 1st Jan 83
Delay in ms/km
6
3
400
800
Days after 1st Jan 83

Fig. 4.9 (c)

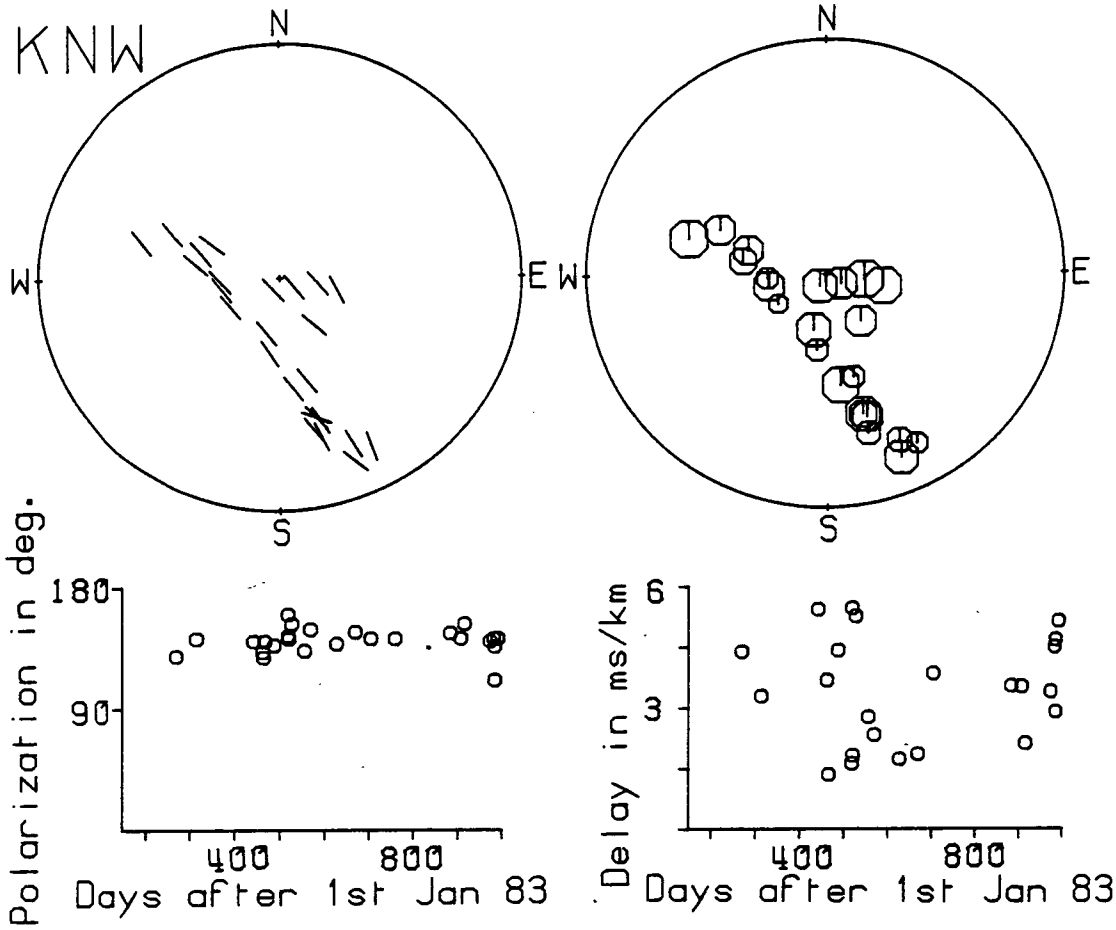
KNW
N
W
E
S
N
W
E
S
Polarization in deg.
180
90
400
800
Days after 1st Jan 83
Delay in ms/km
6
3
400
800
Days after 1st Jan 83

Table 4.5 Locations of earthquakes, polarizations of first-arriving shear waves and delays between split shear wave arrivals recorded at station KNW. The columns marked W show the weight assigned to the polarization or delay in the previous column: in the regression analysis those marked 2 were assigned 2/3 the weight of those marked 1.

(a) Events with raypaths to KNW making incidence angles *less* than 75.5° to the normal of the vertical plane striking N 318°E.

Date and Time						Location						Split shear wave			
						Latitude		Longitude		Depth	M_L	Polarization	W	Delay	W
Y	M	D	H	M	S	°N	min	°E	min	km		°		sec	
83	6	11	2129		20.21	33	38.51	-116	42.45	13.12	1.3	318.	1	0.072	1
83	6	25	1143		54.72	33	39.62	-116	46.15	13.68	1.3	144.	1	0.028	2
83	7	21	19	1	26.25	33	40.27	-116	43.95	14.03	1.6	312.	1	0.012	1
83	7	25		012	18.54	33	39.62	-116	43.89	15.21	1.5	316.	1	0.056	2
83	7	25		018	49.37	33	37.46	-116	41.59	12.43	1.6	155.	1	0.040	2
83	10	2	1323		21.17	33	38.89	-116	43.48	13.00	1.8	131.	1	0.060	1
83	10	21	2053		36.99	33	39.10	-116	42.96	14.00	1.9	142.	1	0.040	1
83	10	23	1057		4.68	33	38.99	-116	43.41	14.01	1.6	139.	1	0.048	1
84	5	27	1310		46.53	33	42.42	-116	49.17	14.52	1.5	154.	1	0.060	2
84	6	27	19	2	2.29	33	38.78	-116	43.27	12.59	1.6	329.	1	0.040	2
84	6	28	1356		22.25	33	42.29	-116	49.40	13.76	2.1	144.	2	0.080	2
84	7	7	2235		7.66	33	37.89	-116	45.17	14.51	2.1	338.	1	0.052	1
84	7	24		848	57.70	33	39.91	-116	46.16	10.11	0.9	333.	2	---	
84	8	15		914	56.14	33	38.88	-116	43.38	13.35	1.8	131.	1	0.060	1
85	4	15		6	2 47.55	33	38.84	-116	43.42	14.13	2.5	144.	1	0.092	2
85	5	16	1549		59.35	33	38.47	-116	44.39	13.56	2.0	129.	1	0.060	1
85	6	15	1935		51.01	33	42.70	-116	49.03	15.49	2.4	120.	1	0.096	2
85	6	16	2127		13.59	33	38.45	-116	43.64	12.78	2.1	126.	1	0.096	1
85	7	2		041	47.42	33	40.10	-116	44.61	15.73	1.8	146.	1	0.068	2
85	9	1		447	32.32	33	38.06	-116	46.57	14.94	2.2	320.	1	0.088	1

Table 4.5 (continued)

(b)Events with raypaths to KNW making incidence angles *greater* than 75.5° to the normal of the vertical plane striking N 318° E

Date and Time						Location				Depth	M_L	Split Shear Wave			
						Latitude		Longitude				Polar-ization	W	Delay	W
Y	M	D	H	M	S	°N	min	°E	min	km		°		sec	
83	9	26	14	1	26.79	33	38.39	-116	40.90	9.33	1.8	129.	1	0.060	1
83	11	9	2333		14.99	33	43.43	-116	46.00	17.32	2.3	322.	1	0.064	1
84	3	16	1953		21.40	33	42.42	-116	41.46	16.80	2.8	-40.	1	0.100	2
84	4	6	057		2.25	33	41.06	-116	41.60	16.67	1.8	132.	1	0.068	2
84	4	7	1420		2.77	33	43.74	-116	45.55	17.21	2.0	128.	2	---	
84	4	9	2135		29.78	33	41.53	-116	44.97	18.94	2.1	140.	1	0.028	1
84	5	1	13	7	52.95	33	42.20	-116	43.16	17.51	2.2	317.	2	0.084	2
84	6	1	19	1	27.68	33	37.69	-116	39.82	12.39	1.3	160.	1	0.028	1
84	6	1	2057		44.07	33	43.42	-116	46.53	10.37	1.9	324.	1	0.072	1
84	6	3	1111		50.86	33	39.45	-116	41.94	15.01	1.4	142.	1	0.032	2
84	6	10	524		19.76	33	42.16	-116	40.50	18.69	1.7	-27.	1	0.108	1
84	7	8	2322		48.79	33	43.05	-116	46.09	16.59	2.2	133.	1	0.052	2
84	7	22	840		23.07	33	37.78	-116	40.43	12.67	1.1	329.	1	0.040	2
84	9	18	334		51.42	33	42.48	-116	45.14	16.68	1.6	138.	1	0.032	1
84	10	30	1642		4.49	33	40.30	-116	43.25	15.20	2.0	147.	1	0.032	1
84	12	4	1542		19.59	33	42.29	-116	42.33	17.21	2.1	-38.	1	0.072	2
85	1	27	20	2	57.46	33	38.21	-116	41.77	13.20	2.8	142.	1	---	
85	6	1	011		36.54	33	38.44	-116	41.53	13.50	2.1	146.	1	0.060	2
85	6	25	323		36.85	33	42.23	-116	45.05	16.39	1.8	142.	1	0.064	1
85	7	3	1241		4.03	33	37.98	-116	41.50	13.07	1.8	153.	1	0.036	1
85	8	30	232		56.54	33	44.16	-116	47.21	17.22	2.1	140.	1	0.068	1
85	9	7	1924		37.56	33	40.85	-116	43.38	16.01	3.0	142.	1	0.080	1
85	9	10	122		33.02	33	38.27	-116	41.60	14.48	2.2	111.	2	0.084	2
85	9	10	122		48.16	33	38.48	-116	41.14	13.69	2.2	136.	1	0.052	2
85	9	16	1823		19.15	33	39.44	-116	42.45	13.79	2.1	142.	1	0.084	1

plane) showed an increase in delay with time of $2.9 \pm 0.8 \times 10^{-3}$ ms/km day, significant at 99%. Shear waves from some of these events were also received at stations WMC and CRY, but there was no significant temporal change in delay between split shear wave arrivals at these stations, though there is a slight indication of an increase at WMC (Fig. 4.10). Other arrivals within the shear-wave window of WMC show no significant change in delay with time.

One cause of apparent change in delay between split shear waves with time would be a systematically changing error in earthquake locations, and thus in the estimated path lengths to the station used to normalize the delays; another would be a systematic change in the incidence angle of the raypaths to the normal to the cracks. The path lengths to station KNW from the events in question showed no significant change with time (Fig. 4.11), so it seems unlikely that the error in path length changes systematically. There is a small decrease in the incidence angle of the raypaths to the crack normal (Fig. 4.12), which we should expect from Fig. 4.4b to cause a small decrease in delay with time, not the observed increase. Cross-sections and time sections of the hypocentres of the events recorded at station KNW in Fig. 4.13 show no obvious systematic migration of hypocentres.

4.8 Interpretation of temporal changes.

An increase in delay between split shear waves can have three possible causes under the EDA theory: a change in crack density (the dimensionless quantity Na^3/v where N is the number of cracks of radius a in volume v of rock); a change in crack aspect ratio;

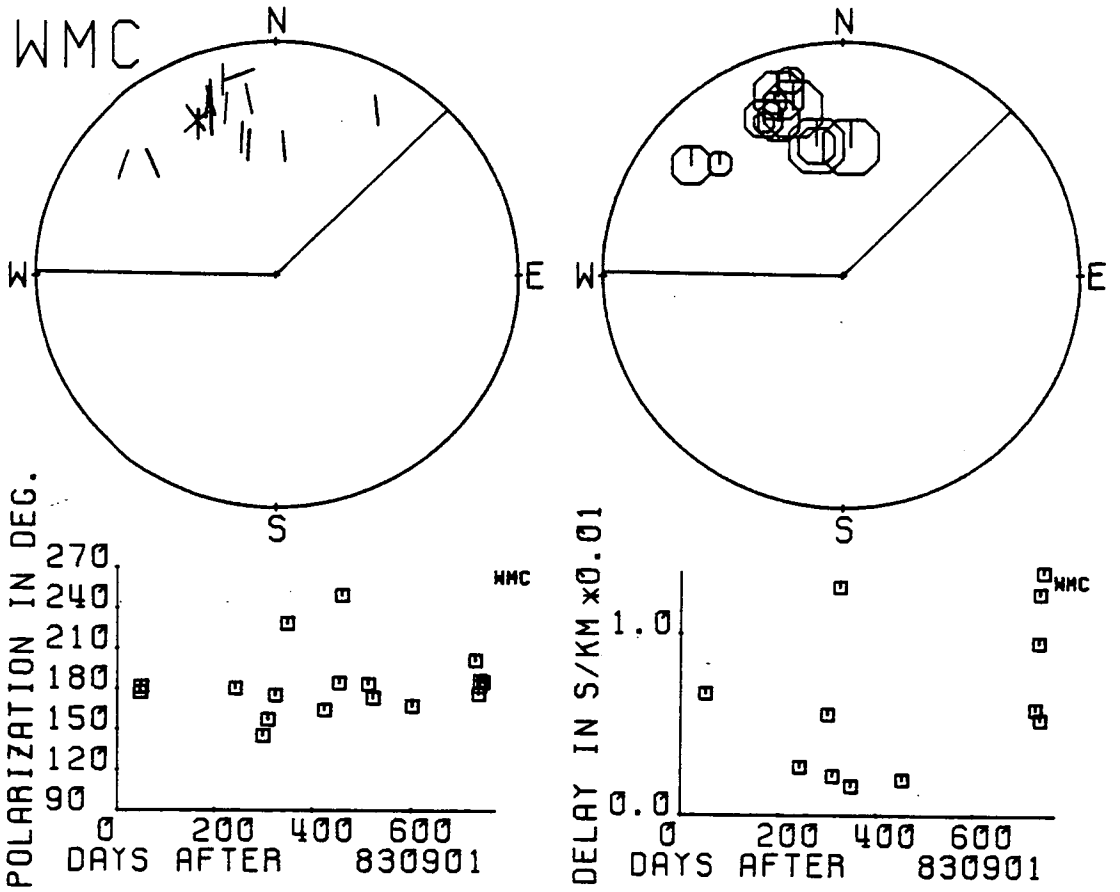

Fig. 4.10 Shear-wave polarizations (left) and delays (right) at station WMC for earthquakes within the shear-wave window of both KNW and WMC. Lower figures show the corresponding quantities plotted against time. Notation as in Fig. 4.9.

Fig. 4.11 Graphs of path length from the foci of the events shown in Fig. 4.9 to station KNW, plotted against time. (a) All paths; (b) paths with incidence angles less than 75.5° from the normal to the vertical plane striking N 318°E (approximately parallel to the strike of the aligned cracks); (c) paths with incidence angles greater than 75.5° from the normal to this plane.

Fig. 4.12 Graphs of incidence angle measured from normal to the vertical plane striking N 318°E (approximately the plane of the inferred cracks), of straight raypaths to KNW from the events shown in Fig. 4.9. (a) All paths; (b) paths with incidence angles less than 75.5° to the normal; (c) paths with incidence angles greater than 75.5° to the normal.

Fig. 4.11

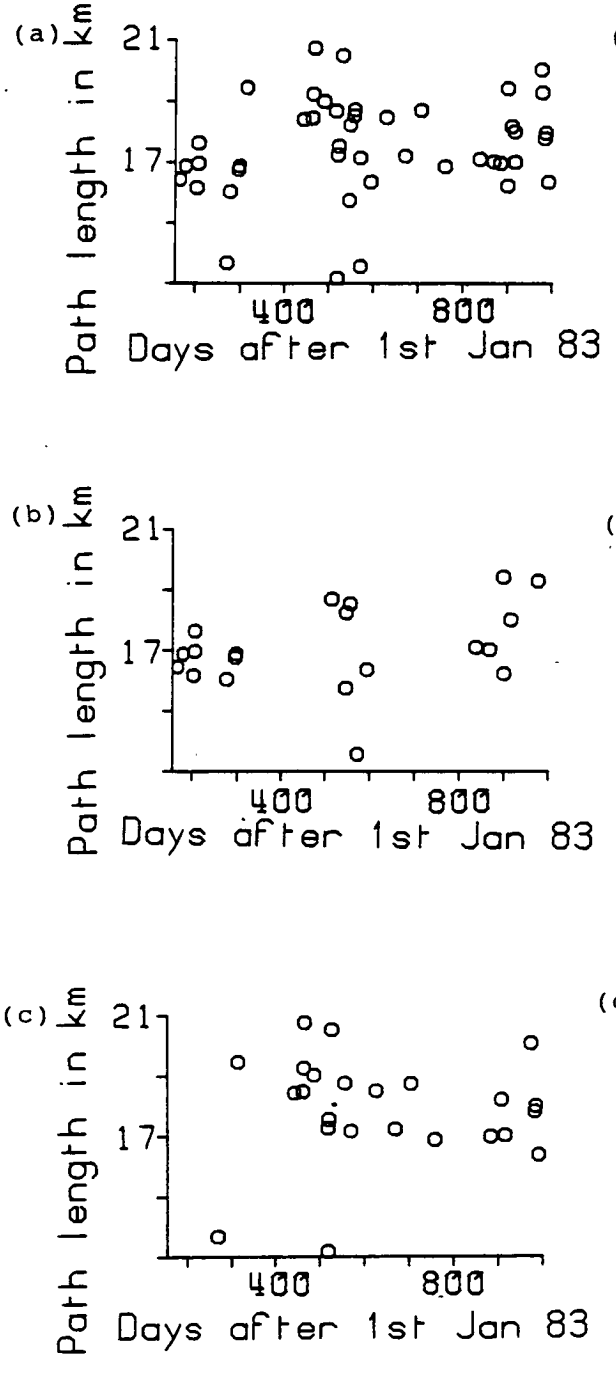

Fig. 4.12

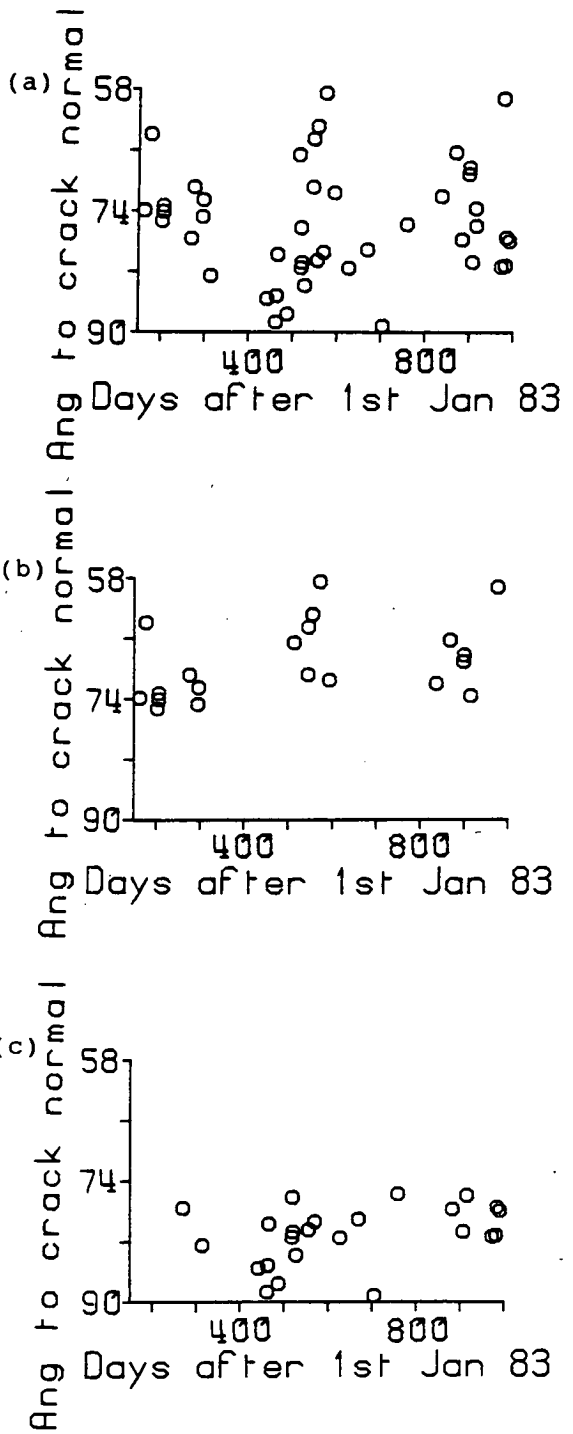

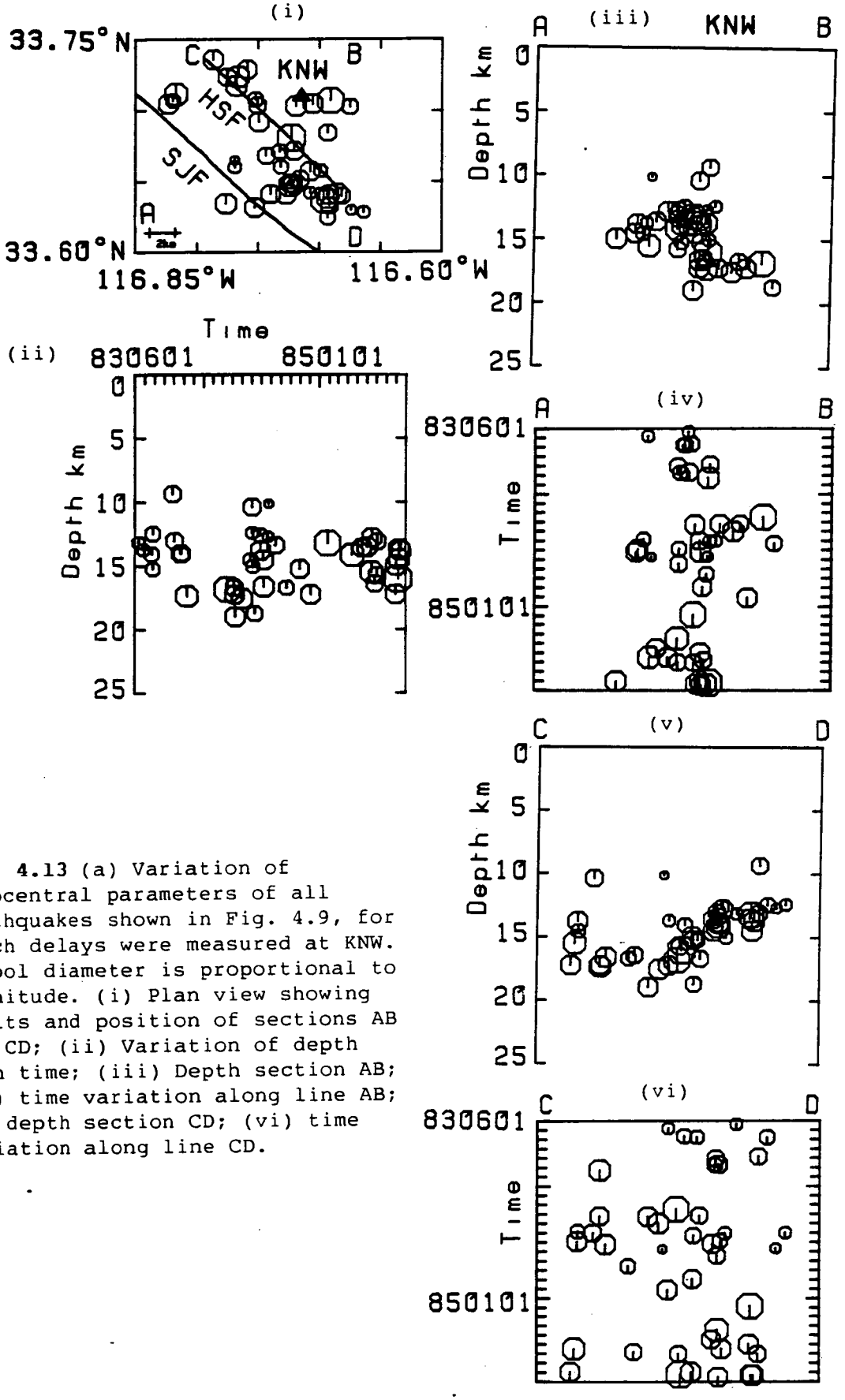

Fig. 4.13 (a) Variation of hypocentral parameters of all earthquakes shown in Fig. 4.9, for which delays were measured at KNW. Symbol diameter is proportional to magnitude. (i) Plan view showing faults and position of sections AB and CD; (ii) Variation of depth with time; (iii) Depth section AB; (iv) time variation along line AB; (v) depth section CD; (vi) time variation along line CD.

Fig. 4.13 (b) Variation of hypocentral parameters of earthquakes with raypaths to KNW making incidence angles less than 75.5° to the normal of the vertical plane striking N 318°E (approximately the inferred strike of the cracks). Notation as in Fig. 4.13(a).

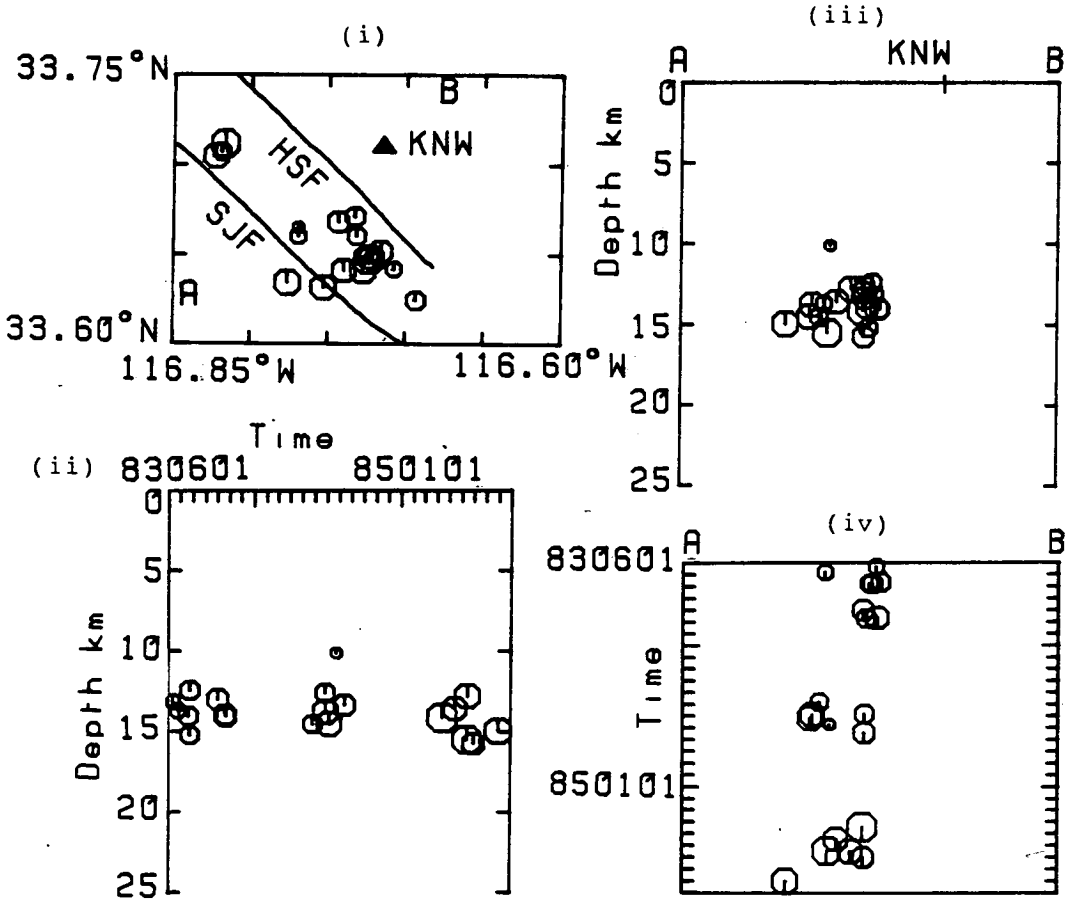

Fig. 4.13 (c) Variation of hypocentral parameters of earthquakes with raypaths to KNW making incidence angles greater than 75.5° to the normal of the vertical plane striking N 318°E. Notation as in Fig. 4.13(a).

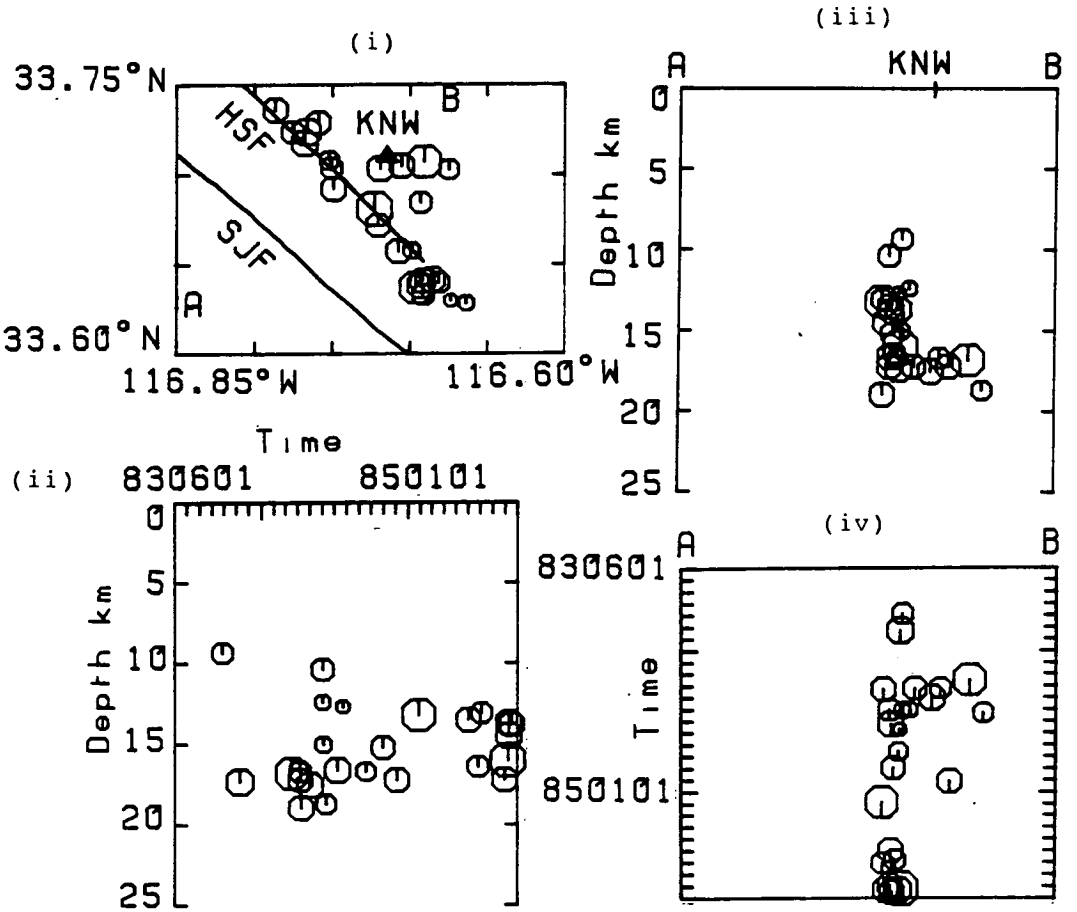

or a change in the contents of the cracks, by their losing fluid, for example (Crampin 1986a). The effects of these changes are shown in Fig. 4.14 (Crampin 1984b; Crampin *et al.* 1986b; Crampin and Booth 1985). An increase in density of uniformly distributed cracks beneath the station increases most the delays between split shear-wave arrivals with large incidence angles to the crack normal (Fig. 4.14b) while an increase in aspect ratio (Fig. 4.14c) or decrease in saturation (Fig. 4.14d) has more effect on waves with smaller incidence angles.

4.8.1 Possible changes in crack geometry at KNW

If the crack geometry beneath KNW is uniform and has been uniformly changed, the restriction of the observed increase in delay with time to waves incident with smaller angles to the crack normal suggests that the crack aspect ratio or fluid saturation, rather than the density, has changed. However, it is likely that the crack geometry beneath KNW is not uniform, since there is no sign of a spatial pattern of delay similar to that for a uniform distribution of cracks (Fig. 4.4b, bottom). The apparently random spatial distribution of delays could be explained by crack density increasing with distance southwest of the station, causing an increase in delay with decreasing incidence angle which might offset the decrease expected for smaller incidence angles to the crack normal. The division of events according to incidence angle to the crack plane is by coincidence approximately equivalent to the division of the epicentres by the Hot Springs Fault, and it is possible that the crack density around or southwest of the fault is larger than that directly beneath the station. An increase in

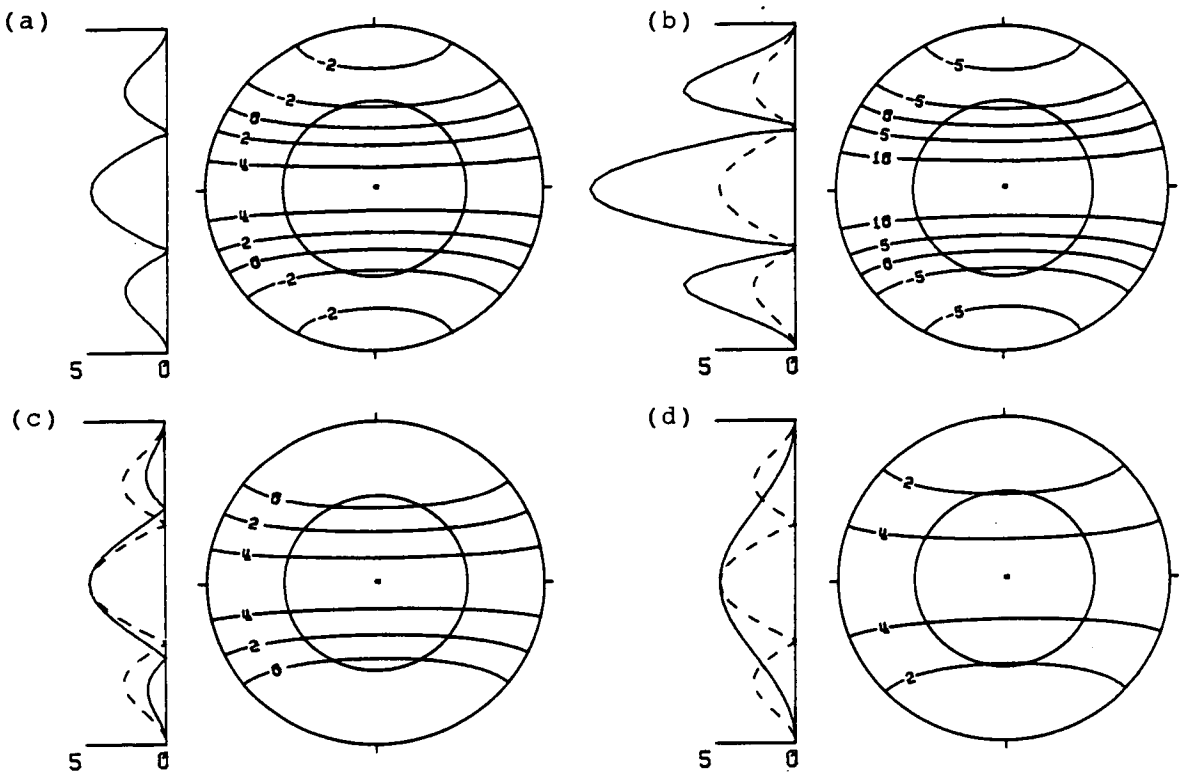

Fig. 4.14 Equal-area projections of theoretical delays between split shear waves passing through a medium containing microcracks aligned east-west with a range of parameters. The delays are contoured in milliseconds per kilometre path length, in equal area projections out to 90°. The inner circle represents 45° incidence angle. On the left of each projection is a north-south section of the contoured delays (solid line), superimposed on the delay (dashed line) for a "reference" model. (a) the "reference" model (see Fig. 4.4): liquid-filled cracks, crack density 0.015, aspect ratio 0.0001; (b) liquid-filled cracks, crack density 0.04, aspect ratio 0.0001; (c) liquid-filled cracks, crack density 0.015, aspect ratio 0.02; (d) dry cracks, crack density 0.015, aspect ratio 0.0001.

crack density restricted to this zone could cause the observed increase in delay with time.

I determined by trial and error some values of changes in crack density and aspect ratio that could cause the observed change in delay at station KNW. A single model does not fit all the observations because of the apparently non-uniform crack density, so models were derived to fit the observed increase in delay from 2.4 to 4.8 ms/km, at incidence angles of 75° and 60° to the crack normal. At incidence angle 75° a small increase in a small crack density (0.011 to 0.021) causes the observed change (Fig. 4.15). This change in crack density must be restricted to the southwest of the station, so as to cause no change in delay at larger incidence angles (75° to 90°) where none was observed. No realistic increase in aspect ratio of these thinly distributed cracks can cause the observed change in delay without change in crack density. At incidence angle 60° the observed change in delay could be modelled by either a larger increase in a larger crack density (0.06 to 0.09, Fig. 4.16), or an increase in aspect ratio from 0.0001 to 0.01 of cracks with constant density 0.06, (Fig. 4.17). The larger crack density is required since the incidence angle, 60°, is near to the crossover point of the qS-wave velocity sheets (Crampin 1981), where the differences in velocities, and hence in delay between split shear-wave arrivals, are small.

The variation of the velocity ratios V_p/V_s for the two split shear waves are shown for the three models of crack change, in Figs. 4.15(c), 4.16(c) and 4.17(c). Observed values of V_p/V_s will generally be calculated from the arrival time of the faster shear wave, and will correspond to the lower of the two values shown for

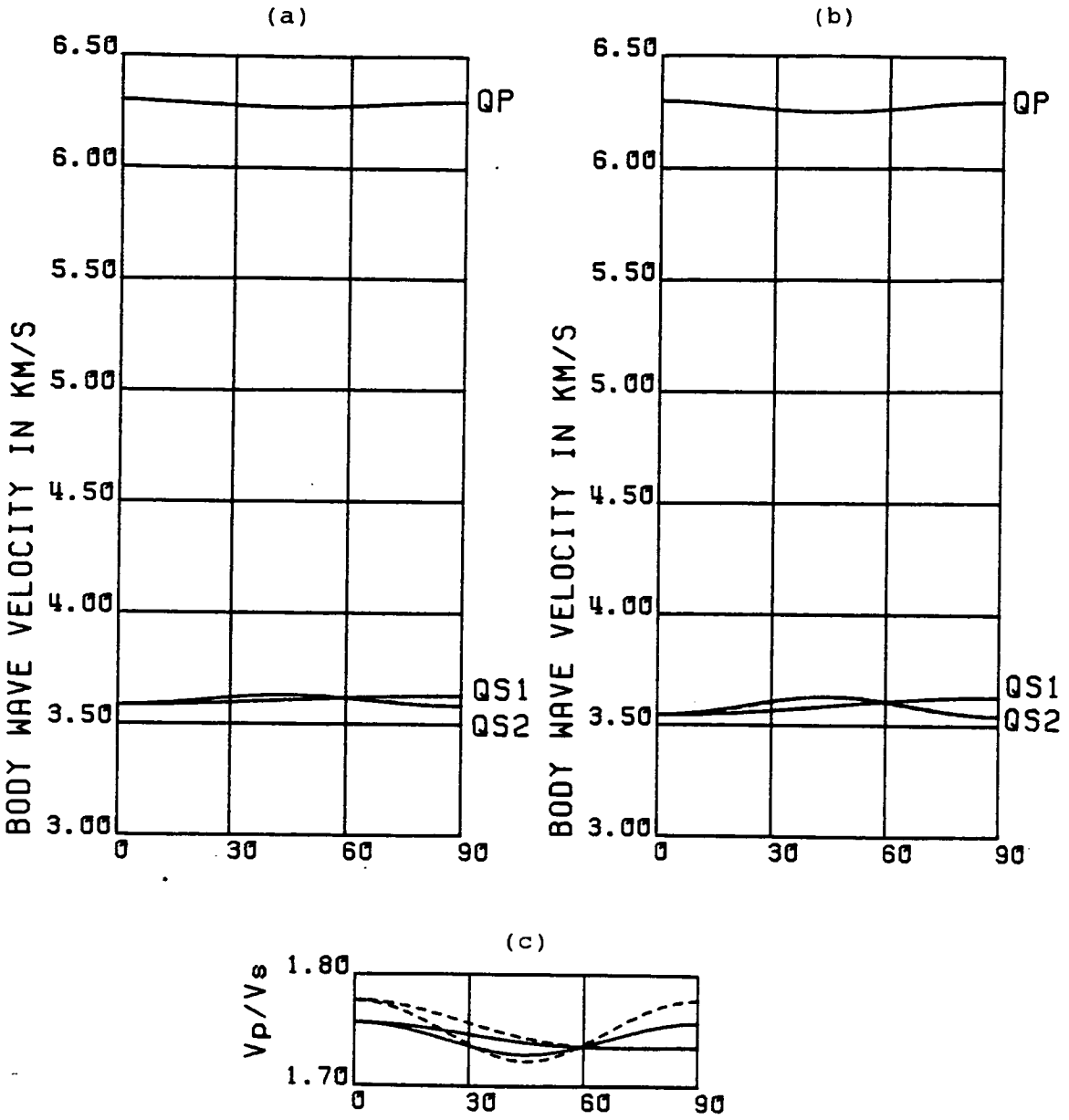

Fig. 4.15 Velocity variations with incidence angle from normal (0°) to parallel (90°) to the plane of vertical parallel microcracks with parameters appropriate to the observed changes in shear-wave splitting at Anza station KNW. The uncracked rock matrix has V_p = 6.3 km/s and V_s = 3.63 km/s. These models correspond to the observed delay change between split shear-wave arrivals at 75° to the crack normal. (a) Crack density 0.011; (b) crack density 0.021; (c) V_p/V_s ratios for the two split shear waves from crack density 0.011 (solid line) and 0.021 (dashed line).

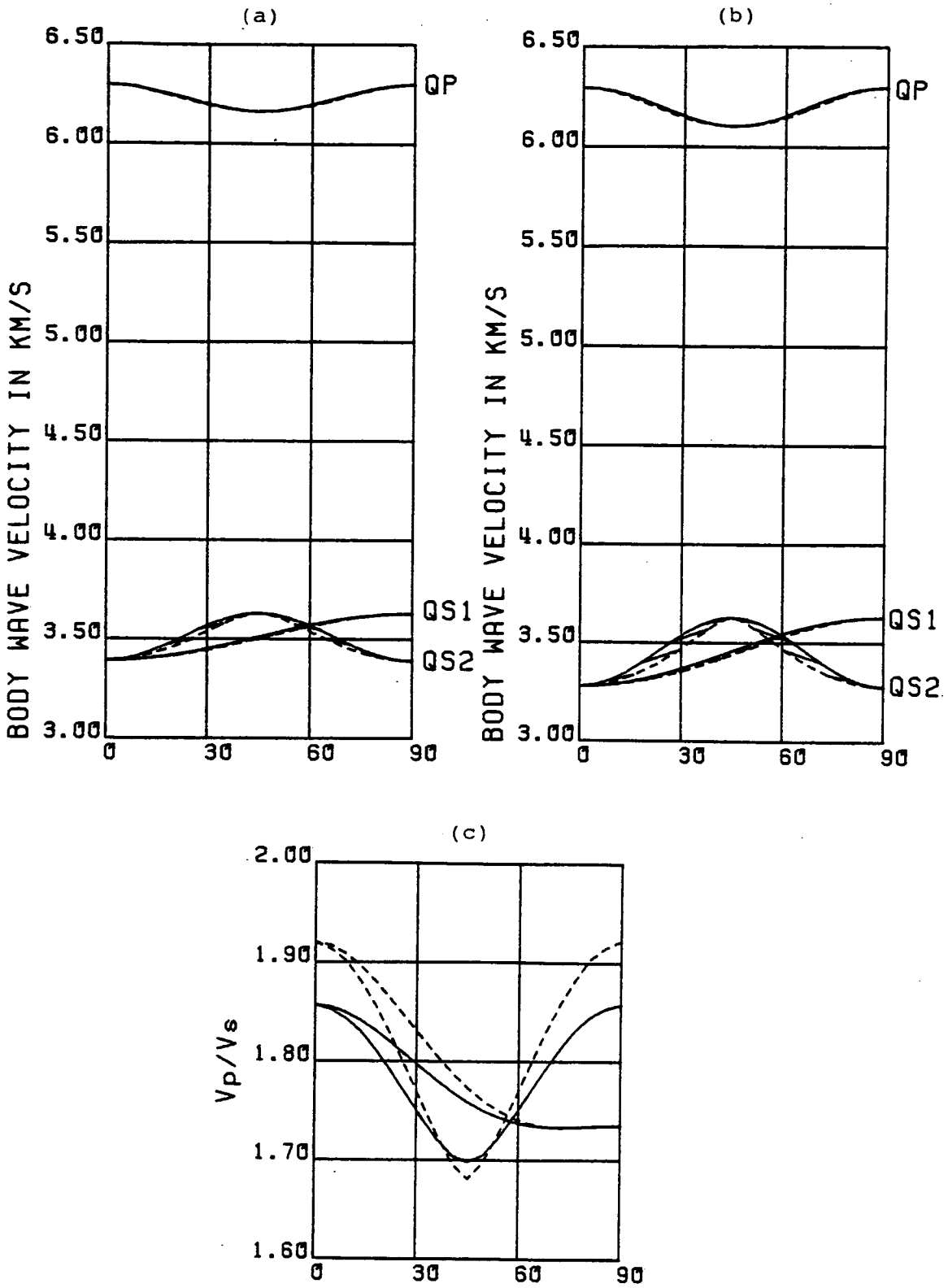

Fig. 4.16 As for Fig. 4.15, but for (a) Crack density 0.06; (b) crack density 0.09; (c) V_p/V_S ratios for the two split shear waves from crack density 0.06 (solid line) and 0.09 (dashed line). Diagonal lines join corresponding phase and group velocities. These models correspond to the observed delay change between split shear-wave arrivals at 60° to the crack normal.

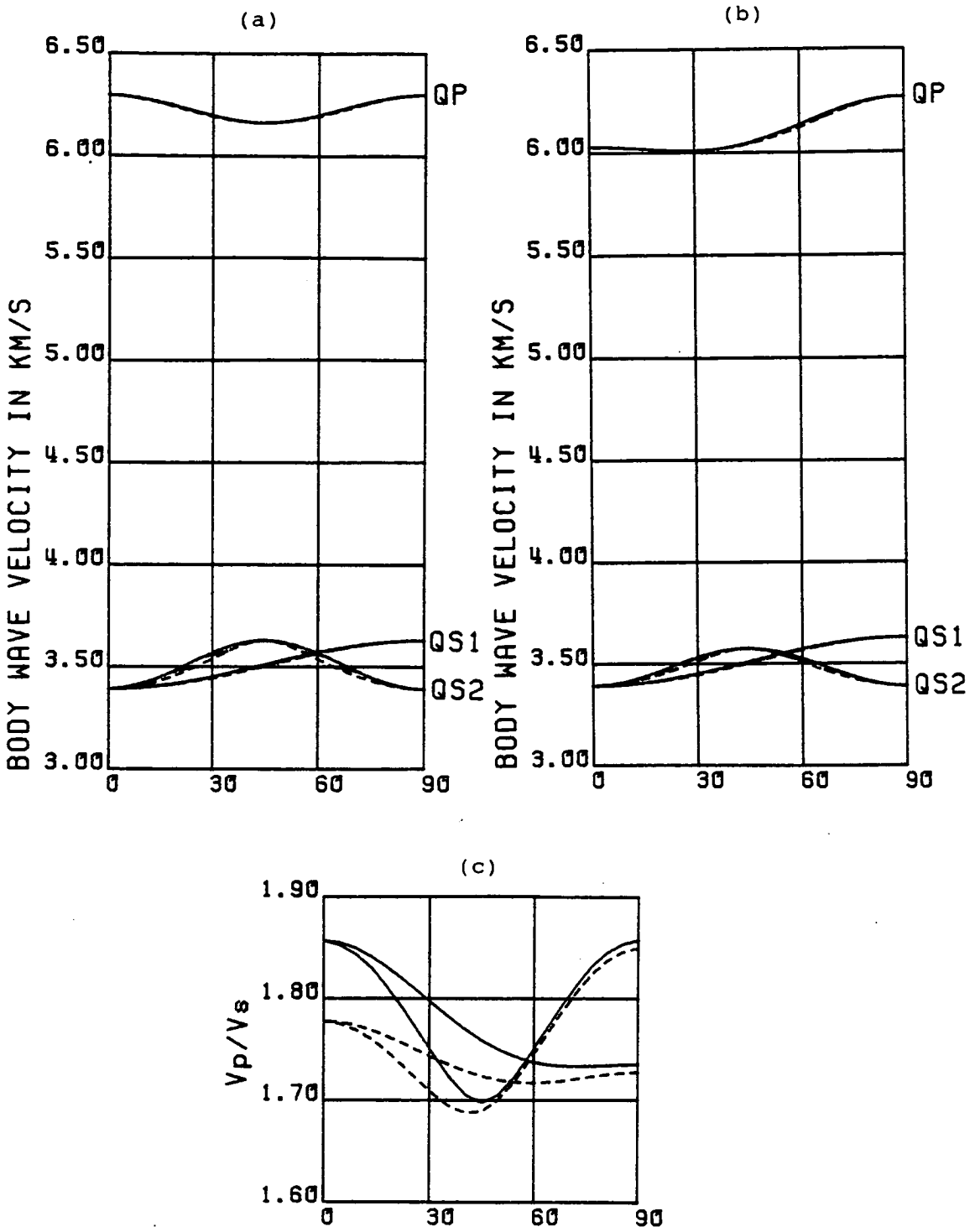

Fig. 4.17 As for Fig. 4.15 but for (a) Crack density 0.06, aspect ratio 0.0001; (b) crack density 0.06, aspect ratio 0.01; (c) V_P/V_S ratios for the two split shear waves from crack density 0.06, aspect ratio 0.0001 (solid line) and crack density 0.06, aspect ratio 0.01 (dashed line). These models correspond to the observed delay change between split shear-wave arrivals at 60° to the crack normal.

each crack geometry.

V_p/V_s changes caused by changes in crack parameters vary with incidence angle to the crack plane. An increase in crack density (Figs. 4.15 and 4.16) causes V_p/V_s to increase for most incidence angles, while an increase in aspect ratio causes V_p/V_s to decrease, largely because V_p decreases. V_p/V_s in directions in the plane of the cracks suffers least change, since both the P- and faster shear wave are polarized parallel to the cracks, and are little affected by changes in crack size or density.

4.8.2 Causes of change in crack geometry

As there is no prior knowledge of the effects of stress changes on EDA cracks in earthquake zones, we can only speculate on which of the above changes in crack parameters has occurred at Anza. Studies of stress drops on the San Jacinto Fault and surrounding areas in the Anza seismic gap (Frankel 1984; Sanders and Kanamori 1984; Fletcher *et al.* 1986b) suggest that stress is concentrated on asperities or barriers on the fault itself, and it is unlikely that the high stress required to cause conventional dilatancy by the opening of new (dry) cracks and increase of aspect ratio of these cracks (Brace *et al.* 1966) exists beyond the immediate vicinity of these stress concentrations. The uniformity and absence of temporal change of the aligned polarizations at KNW (Fig. 4.9a) imply a uniform, unchanging stress orientation not compatible with high stress acting on a small volume of highly fractured rock (Brady 1974, 1975). An increase of a much lower stress could cause subcritical growth of existing cracks rapid enough to lead to appreciable changes in crack density over the 29-month recording

period (Crampin *et al.* 1984b). The observed temporal variation could be due to such crack growth in the rock southwest of KNW; but a more direct cause might be a purely elastic increase in aspect ratio of existing cracks, which would occur immediately on any increase of stress.

With observations restricted to the shear-wave window it is difficult to distinguish between the effects of crack aspect ratio change and fluid saturation change (Figs. 4.14c and d). Since EDA cracks are probably isolated, Crampin (1986a) suggests that fluid is not lost from them, and as the fluid may be at near-lithostatic pressure (Crampin *et al.* 1984b), a small increase in crack aspect ratio and hence volume will probably be accompanied by an increase in volume of the decompressed fluid, so that the cracks will remain saturated (S. Crampin, personal communication). One possible cause of an apparent change in saturation of liquid-filled cracks is an increase in heat flow raising the temperature above the critical point of the liquid. The cracks would then be filled with supercritical vapour, which would make their seismic properties intermediate between those of dry (vacuum-filled) and liquid-filled cracks (Crampin *et al.* 1986b). This seems unlikely in the Anza area, which does not have high heat flow (Frankel 1984) or recent geothermal or volcanic activity.

4.9 Conclusions

The splitting and aligned polarizations of shear waves incident within the shear-wave window at nine Anza network stations indicate effective anisotropy in the underlying rock. Since the rock (granite) shows no obvious alignment of mineral grains, I suggest,

following numerous observations elsewhere, that the anisotropy is caused by water-filled microcracks aligned by the stress field of the San Jacinto Fault. This interpretation is supported by the observation of temporal changes in delay between split shear wave arrivals at one station, KNW, which indicate (geologically) rapid changes in anisotropy incompatible with all other causes except stress-aligned cracks (Crampin 1978; Crampin *et al.* 1984b; Crampin and Booth 1985). These results are the strongest support yet found for the EDA theory of Crampin *et al.* (1984b).

The stress field in the Anza seismic gap is dominantly north-south compression, causing north-south alignment of microcracks which affects shear-wave polarizations. At two stations, SND and KNW, there is evidence that the stress field is locally perturbed: at SND the stress appears to be normal to the fault and may be responsible for the slip resistance of the fault in the seismic gap (Sanders and Kanamori 1984); while at KNW the stress is parallel to the fault.

The changes in crack parameters causing the observed change in delay between split shear-wave arrivals at station KNW, though significant, are not well determined. More observations, well-distributed over time and the focal sphere, are required to distinguish between changes in crack density, aspect ratio and saturation; but I suggest that the changes are caused by stress accumulation in preparation for a larger earthquake. As there are no previous case histories to compare with my results, I cannot predict the magnitude of this hypothetical earthquake or whether it will rupture the entire Anza seismic gap. The whole length of the San Jacinto Fault in the seismic gap is highly stressed (Sanders

and Kanamori 1984), and it seems possible that a rupture initiated at one end of the gap could propagate to the other end even if the stress on the rest of the gap has not changed sufficiently to cause observable precursors. Station WMC, near to the fault, showed no increase in delay with time, and none of the other stations near to the gap had enough delay readings for a temporal change indicating stress accumulation to be detected.

Further investigations of temporal changes in split shear waves require three-component vertical seismic profiles (VSPs) with artificial sources of accurate, repeatable radiation patterns, so that small changes in crack parameters can be monitored (Crampin 1986a). Besides station KNW, a likely site for temporal changes in crack parameters may be the Cahuilla earthquake swarm, southwest of station CRY (Fig. 4.1), which Sanders and Kanamori (1984) suggest may act as a "stress meter" of the nearby San Jacinto Fault. The swarm earthquakes at Cahuilla are shallow, around 5 km (Fletcher *et al.* 1986a), and few are within the shear-wave window of CRY, the nearest station. Three-component records from stations installed immediately above the swarm, combined with repeated VSPs, would be necessary to detect any temporal change. There may be enough similarity among the waveforms of the swarm earthquakes to allow cross-correlation methods to detect temporal changes more accurately (Poupinet *et al.* 1985; Logan 1986).

CHAPTER 5

Conclusions, discussion and speculation

5.1 Introduction: conclusions from Chapters 2, 3 and 4

I have presented results in Chapters 2-4 that show the value of shear-wave analysis for investigating anisotropy, and the importance of recognizing all the effects of anisotropy on shear wavetrains. The outstanding conclusions from each chapter are:

Chapter 2

1. In transversely isotropic media with a vertical axis of symmetry, such as horizontally bedded shale, shear waves are split into SH and SV polarizations, and shear-wave splitting is best observed with a source of mixed polarity shear waves.
2. The deviation of the SV polarization from perpendicular to the raypath in transversely isotropic media can be misinterpreted as an effect of a velocity gradient.

Chapter 3

1. Cracks and microcracks aligned in the regional stress field of the British Isles (extensive-dilatancy anisotropy or EDA) pervade the crust beneath the Lleyn Peninsula, North Wales, possibly to depths of 20 km or more.
2. Strongly anisotropic slate splits incoming shear waves, obliterating any polarizations caused by aligned cracks. The faster shear wave in the slate is generally polarized parallel to the cleavage.

1. EDA in the Anza seismic gap, Southern California, is aligned in the regional stress field or by local stress anomalies.
2. A gradual change in crack geometry, possibly an increase in aspect ratio of aligned cracks, is occurring near one end of the seismic gap. This is the first recorded observation of a change in EDA possibly caused by a strain increase preceding an earthquake.

A theme common to all three chapters is the use of polarization diagrams of shear-wave particle motion in three dimensions to identify the effects of anisotropy. These particle motions can be reproduced by synthetic seismograms from anisotropic models, which sometimes give essential support for speculative interpretations (for instance in North Wales, Chapter 3). Shear waves may carry more than three times as much information as P-waves about material properties such as anisotropy, but the information is complex and occasionally ambiguous. Since there are no direct inversion procedures for detailed particle motion, forward modelling at present gives the closest constraint on the interpretation of shear-wave records (Crampin *et al.* 1986c).

The shear-wave investigations in North Wales (Chapter 3) and the Anza seismic gap (Chapter 4) revealed EDA, which appears to be inevitable in the stressed rocks of the Earth's brittle crust (Crampin 1986a). The change in delay between arrivals of split shear waves at Anza (Chapter 4) is the most conclusive evidence yet that aligned cracks cause anisotropy in earthquake zones which changes in response to the changing stress field.

EDA is possibly the most widespread type of anisotropy in the crust, but other types of anisotropy, such as the lithological anisotropy of shale (Chapter 2) and the crystalline anisotropy of slate (Chapter 3) also cause shear-wave splitting and distinctive polarizations, sometimes (Chapter 3) confusingly similar to those caused by EDA.

In this chapter I turn to the implications of these conclusions for the investigation of anisotropy and especially the prediction of earthquakes.

5.2 The need to recognize anisotropy

Crampin and Radovich (1982) and Doyle *et al.* (1982) have emphasized that misleading results can arise from assuming isotropy when interpreting data from anisotropic media. Chapters 2 and 3 contain instances where misinterpretation was possible even when anisotropy had been recognized. The velocity measurements of Robertson and Corrigan (1983) revealed the transverse isotropy of the shale, but the ambiguity between increase in velocity with depth and deviation of SV polarization from perpendicular to the group-velocity direction was resolved only after detailed modelling. This result proves the point of Crampin (1986c) that it is impossible to determine accurately the orientation of three-component borehole seismometers from relative amplitudes of shear-wave arrivals on the components without thorough prior knowledge of the velocity structure and anisotropy of the host rock. Transverse isotropy, as shown by shale, would cause errors in the measured dip of the seismometer components, while azimuthal anisotropy, such as that shown by vertical parallel microcracks,

causes ambiguity in the azimuths of the components. If crack-induced anisotropy is to be monitored using vertical seismic profiles (Crampin 1986a, c), component orientations must be determined either by non-seismic means or by using P-waves (DiSiena *et al.* 1984), which show only a small deviation of polarization from group-velocity direction (Crampin *et al.* 1982).

5.3 Is the anisotropy intrinsic or is it EDA?

Analysis of shear waves may yield accurate parameters of anisotropy, but can give only indirect evidence of its cause. In North Wales (Chapter 3) and Anza (Chapter 4) we were looking for EDA, but in North Wales at least, EDA was not the only type of anisotropy present. Many rocks are intrinsically anisotropic (with lithological or crystalline anisotropy - see Chapter 1) at the scale of microscopic or hand specimens; a few, including sedimentary rocks such as shale, and metamorphic rocks such as slate, schist and gneiss, are anisotropic on the scale of seismic wavelengths (tens or hundreds of metres). The effect of these rocks depends on the orientation of their bedding or cleavage planes: horizontally bedded shale, being transversely isotropic, is unlikely to be confused with EDA in seismic interpretation, but rocks with intrinsic azimuthal anisotropy, such as vertical or dipping beds of shale, or slate, schist or gneiss with non-horizontal cleavage or foliation, may have effects on seismic waves similar to those of aligned microcracks. Any rock with vertical or near-vertical bedding or cleavage planes has hexagonal symmetry about a horizontal or near-horizontal axis, similar to the observed symmetry of EDA (Crampin and Booth 1985). Some rocks of

this type are highly anisotropic (Christensen 1965, 1966; Kaarsberg 1968), and even a thin layer could cause appreciable shear-wave splitting, with the leading shear wave generally polarized parallel to the cleavage or foliation. As anisotropy caused by small concentrations of aligned cracks in otherwise isotropic rock is often weak in comparison (Crampin and Booth 1985; Crampin and Bush 1986; see Chapter 3), the waves must subsequently pass through a much greater thickness of cracked rock with cracks not parallel to the cleavage before the polarization of the leading shear wave is detectably influenced by the cracks. Hidden layers of highly intrinsically anisotropic rocks could therefore give misleading results in investigations of EDA.

One possible sign of intrinsic anisotropy may be that polarizations are difficult to read, as observed in North Wales (Chapter 3) and Japan (Kaneshima *et al.* 1986a) because mode conversions at the interfaces of strongly intrinsically anisotropic layers (see Chapter 1) may have large amplitudes which cause complexity in the seismogram.

Slate and other metamorphic rocks with stress-aligned crystals, and tilted and folded formations of bedded rocks such as shale, which show azimuthal anisotropy, are found in former orogenic or subduction zones where horizontal compression was high. Present earthquake zones are often associated with these zones of past compression, and intrinsic anisotropy may be encountered frequently in surveys of EDA for stress monitoring and earthquake prediction. Earthquake zones often have complex geology in which the intrinsically anisotropic layers may be hidden by other intrinsically isotropic rocks. The danger of not recognizing the

presence of intrinsic anisotropy is especially high in surface recordings of shear waves from depths for which no direct geological information can be obtained.

5.4 . . . . or both?

It is not known whether rocks with strong alignment of crystals or grains can support suites of aligned microcracks in planes other than the plane of bedding, cleavage or foliation. The combination of aligned microcracks and aligned rock fabric in different planes would generally cause anisotropy with orthorhombic or monoclinic symmetry, or triclinic symmetry in the extreme case of an intrinsically anisotropic rock pervaded by two or more non-orthogonal sets of aligned cracks (Crampin 1978).

Robertson and Corrigan (1983) found no significant difference between the velocities for corresponding incidence angles on the North and East shot lines in the shale at Sulphur Springs, Texas. The regional stress field in Texas, determined from *in-situ* stress measurements summarized by Zoback and Zoback (1980), is approximately east-west or ESE-WNW compression. If this stress field exists at Sulphur Springs, it has apparently not caused appreciable alignment of microcracks in the shale sampled by the experiment. It is possible that cracks are aligned in a local stress field at an azimuth midway between the North and East shot lines, giving identical velocities along both. Another explanation might be that at the shallow depth of the Sulphur Springs geophone (53 m) the stress field is affected by the free surface, which causes the dominant stress to be lithostatic and vertical, giving rise to vertical cracks with random strike and horizontal coplanar

normals (S. Crampin, personal communication). Shale containing this crack geometry has the same anisotropic symmetry as uncracked shale, vertical transverse isotropy (Crampin and Radovich 1982), and would be indistinguishable from uncracked shale to seismic waves.

Anisotropic slate probably affected shear-wave arrivals at two or more stations in North Wales. The number and distribution of aftershocks was insufficient to determine the spatial distribution of shear-wave polarization and delay, from which the form of anisotropic symmetry of the slate, and hence the effect of any aligned cracks, could be determined. I speculate that because slate is weak along cleavage planes, any compressive stress oriented within approximately 45° of the cleavage will open cracks parallel to the cleavage rather than the direction of compression.

5.5 EDA, V_p/V_s changes and earthquake prediction

Changes in the ratio of P- and shear-wave velocities (V_p/V_s) have been observed before several large earthquakes (summarized in Rikitake 1976). The usual form of these changes is a decrease in V_p/V_s, followed by an increase to a value equal to or greater than the original value; the duration of the episode of change increases with the magnitude of the eventual earthquake. The two original theories for this behaviour agree that the initial decrease in V_p/V_s is caused by the opening and growth of dry (vacuum-filled) cracks under high stress, but they differ in explaining the subsequent increase in V_p/V_s (Mjachkin *et al.* 1975). In the dilatancy-diffusion model (Scholz *et al.* 1973) water flows into the initially dry cracks as they lengthen and interconnect, reducing

the pore pressure in existing water-filled cracks and thus causing stress hardening so that rapid crack growth ceases. Pore pressure then rises again, reducing the shear strength along the fault plane until rupture occurs. In the dilatancy-instability model (Mjachkin *et al.* 1975), after the initial opening of cracks in a large volume of rock, stress is concentrated on the eventual rupture zone causing unstable deformation there and partial release of stress (and closure of cracks) further away.

Crampin (1978) demonstrated that in theory, changes in geometry of aligned dry cracks, and their subsequent filling with water, could cause the observed V_p/V_s precursors, depending on the source mechanism and source-receiver paths with respect to the crack alignment. Crampin *et al.* (1984b) suggest that V_p/V_s changes are caused at least in part by subcritical growth and elastic change in aspect ratio of isolated water-filled cracks and microcracks in large volumes of rock under much lower stress. They point out that water-filled cracks probably occur throughout the crust (see Chapter 1), but do not discuss possible mechanisms for the observed pattern in V_p/V_s change.

Dry cracks, as postulated in the two conventional-dilatancy models of earthquake precursors, can occur only when crack growth is faster than fluid diffusion (Scholz *et al.* 1973). Fluid diffusion into opening cracks is apparently rapid (Bonner 1975), so dry cracks are unlikely to persist except in small zones of high stress at earthquake foci, where they are being opened continually. The increase in aspect ratio of fluid-filled microcracks may explain decreases in V_p/V_s without the necessity for dry cracks. Crampin *et al.* (1986b) show that increasing the aspect ratio of

fluid-filled cracks causes the velocity variations with direction in the medium to approach those due to dry cracks in the same medium; and in Chapter 4 (Fig. 4.17) it was shown that an increase in aspect ratio of fluid-filled cracks causes a decrease in V_p/V_s in certain directions.

5.5.1 Comparison of my results with previous V_p/V_s precursors

The increase in crack aspect ratio postulated to explain the increase in delay between split shear-wave arrivals at Anza station KNW (Chapter 4) causes a decrease in V_p/V_s in most directions not parallel to the plane of the cracks (Fig. 4.17). Similar decreases in V_p/V_s have been observed at Garm, USSR (Semenov 1969; Wyss 1975); Blue Mountain Lake, New York, USA (Aggarwal *et al.* 1973); San Fernando, California, USA (Whitcomb *et al.* 1973); before two shallow earthquakes in Japan (Ohtake 1973); and elsewhere (Rikitake 1976). An elastic increase in aspect ratio could be the mechanism of V_p/V_s decrease at all these sites. The duration of the V_p/V_s anomalies and other precursors has been related to the magnitude of the eventual earthquake (Whitcomb *et al.* 1973; Scholz *et al.* 1973). The 29-month (minimum) duration of the increase in delay between split shear-wave arrivals at KNW is comparable to the 3.5 year period of anomalous V_p/V_s before the magnitude 6.4 San Fernando earthquake (Whitcomb *et al.* 1973) and the 1 year period before the magnitude 6.5 North Miyagi earthquake in Japan (Ohtake 1973), and longer than the few months or days of anomalous V_p/V_s preceding the smaller (magnitude 2 - 5) earthquakes in the other investigations. As the magnitude of the earthquake required to rupture the Anza seismic gap (6.5, Thatcher *et al.* 1975) is similar to those of the San

Fernando and Miyagi earthquakes, it is tempting to speculate that the change in delay at KNW is a precursor to this earthquake; but direct comparison of the Anza results with other precursory sequences may not be appropriate. Precursory V_p/V_s changes are probably different in the different stress regimes and rock types at the three sites; and observed changes in V_p/V_s and split shear-wave delays may have different sensitivities to stress change. Finally, V_p/V_s changes measured at San Fernando and elsewhere are biased by the source-receiver arrangement with respect to the (unknown) crack geometry. Confident prediction of earthquake magnitude at Anza or anywhere else should be based mostly on comparison with well-documented precursors of previous earthquakes at the same site.

5.5.2 Changes of crack aspect ratio in earthquake zones

The increase in aspect ratio of cracks in an earthquake zone causes an expansion of the rock in directions perpendicular to the direction of maximum compression, which may contribute to anomalous tilt, strain and level changes before earthquakes. Many such changes have been observed (Rikitake 1976; Thatcher 1981), some at distances of hundreds of kilometres from the eventual earthquake (Dobrovolsky *et al.* 1979). They are probably due in part to plastic deformation in the lower crust (Thatcher 1981) as well as dilatancy in the upper crust (Scholz *et al.* 1973).

If elastic changes in aspect ratio of fluid-filled cracks are the main cause of precursory decreases in seismic velocities and V_p/V_s, the subsequent return of V_p/V_s to approximately its original value immediately before an earthquake, observed in almost all

cases, may be due to a decrease in crack aspect ratio caused by the de-stressing of rock away from the fault as stress is concentrated on the point of eventual rupture, as described by the dilatancy-instability model.

In aftershock sequences, such as that in North Wales, changes in aspect ratio seem unlikely to be important. If precursory changes in crack aspect ratio are purely elastic, most cracks will immediately return to approximately their "original" aspect ratio when the stress is released by the main shock. Changes in aspect ratio during an aftershock sequence will probably be small and restricted to patches of the fault where stress has not been entirely released (Das and Scholz 1981), unless stress is building up appreciably for another large earthquake in the same area. Cracks opened by critical or subcritical crack growth before and during an earthquake can heal rapidly, depending on temperature and fluid saturation (Smith and Evans 1984), but healing may be slow enough, especially in the coolest uppermost level of the crust, to cause an observable decrease in crack density over time during an aftershock sequence. This is possibly the cause of the slight decrease in delay between split shear-wave arrivals with time at station YMY in North Wales (Chapter 3 Fig. 3.15).

5.5.3 The future of EDA in earthquake prediction and elsewhere

The EDA theory of earthquake prediction places V_p/V_s anomalies in the wider context of regular and quantifiable directional variations of elastic properties of the crust in response to growth and change of stress-aligned cracks. Future investigations of earthquake precursors will have to be planned to take this spatial

variation into account. Surface recordings of natural earthquakes are subject to constraints including the effects of the free surface (see Chapter 1); restrictions of station distribution; topographic and geological effects; and the random occurrence, unrepeatability and inaccurate location of sources. All of these factors lead to a high rejection rate of data and large uncertainties, as seen in Chapters 3 and 4. Downhole recording of artificial sources overcomes most of these restrictions. Vertical seismic profiling or cross-hole shooting using P- and shear-wave sources firing to three-component receivers could give velocity, attenuation and polarization data which would allow evaluation of crack parameters in three dimensions to depths of 10 km or more. These results can now be modelled with versatile synthetic seismogram routines (Crampin *et al.* 1986c; Taylor 1986); and borehole cores or logs may reveal any intrinsic anisotropy present, allowing more reliable interpretation of EDA. A knowledge of crack orientation is useful to oil and gas exploration and reservoir exploitation; geothermal energy extraction; groundwater flow studies; and site investigation for mining, quarrying and nuclear waste disposal. Repeated surveys could lead to rapid and accurate detection of changes in crack parameters, which may be valuable in predicting rockbursts in mines and monitoring the effects of hydraulic fracturing (Crampin 1986a) as well as in earthquake prediction.

REFERENCES

Aggarwal, Y. P., Sykes, L. R., Armbruster, J., and Sbar, M. L., 1973. Premonitory changes in seismic velocities and prediction of earthquakes, *Nature*, **241**, 101-104.

Aki, K., and Richards, P. G., 1980. *Quantitative seismology, theory and methods*, Freeman, San Francisco.

Ansell, J., Aspinall, W., King, G., and Westaway, R., 1986. The 1984 July 19 North Wales earthquake - a lower crustal continental event indicating brittle behaviour at an unusual depth, *Geophys. J. R. astr. Soc.*, **84**, 201-206.

Atkinson, B. K., 1979. A fracture mechanics study of subcritical tensile cracking of quartz in wet environments, *Pure appl. Geophys.*, **117**, 1011-1024.

Atkinson, B. K., 1982. Subcritical crack propagation in rocks: theory, experimental results and applications, *J. struct. Geol.* **4**, 41-56.

Atkinson, B. K., 1984. Subcritical crack growth in geological materials, *J. geophys. Res.*, **89**, 4077-4114.

Ave'Lallemant, H. G., and Carter, N. L., 1970. Syntectonic recrystallization of olivine and modes of flow in the upper mantle, *Bull. geol. Soc. Am.*, **81**, 2203-2220.

Babuška, V., 1984. P-wave velocity anisotropy in crystalline rocks, *Geophys. J. R. astr. Soc.*, **76**, 113-119.

Bamford, D., 1977. P_n velocity anisotropy in a continental upper mantle, *Geophys. J. R. astr. Soc.*, **49**, 29-48.

Banik, N. C., 1984. Velocity anisotropy of shales and depth estimation in the North Sea Basin, *Geophysics*, **49**, 1411-1419.

Bentley, C. R., 1971. Seismic anisotropy in the West Antarctic ice sheet, in *Antarctic Research Series*, **16**, *Antarctic snow and ice studies II*, 131-177, ed. A. P. Crary, Amer. Geophys. Union, Washington D. C.

Berger, J., Baker, L. M., Brune, J. N., Fletcher, J. B., Hanks, T. C., and Vernon, F. L., 1984. The Anza array: a high-dynamic-range, broadband, digitally radiotelemetered seismic array, *Bull. seism. Soc. Am.* **74**, 1469-1481.

Blenkinsop, T. G., Long, R. E., Kusznir, N. J.,and Smith, M. J., 1986. Seismicity and tectonics in Wales, *J. Geol. Soc. London.*, **143**, 327-334.

Blundell, D. J., 1985. Nature of reflections from the continental crust and upper mantle, paper presented at the 23rd General Assembly of the International Association of Seismology and Physics of the Earth's Interior, Tokyo, August 1985.

Bonner, B. P., 1975. V_p/V_s in saturated granodiorite loaded to failure, *Pure Appl. Geophys.*, **113**, 25-29.

Boore, D. M., McEvilly, T. V., and Lindh, A., 1975. Quarry blast sources and earthquake prediction: the Parkfield, California, earthquake of June 28th, 1966. *Pure appl. Geophys.*, **113**, 293-296.

Booth, D. C., and Crampin, S., 1983a. The anisotropic reflectivity technique: theory, *Geophys. J. R. astr. Soc.*, **72**, 755-766.

Booth, D. C., and Crampin, S., 1983b. The anisotropic reflectivity technique: anomalous arrivals from an anisotropic upper mantle, *Geophys. J. R. astr. Soc.* **72**, 767-782.

Booth, D. C., and Crampin, S., 1985. Shear-wave polarizations on a curved wavefront at an isotropic free surface, *Geophys. J. R. astr. Soc*, **83**, 31-45.

Booth, D. C., Crampin, S., Evans J. R., and Roberts, G., 1985, Shear-wave polarizations near the North Anatolian Fault - I. Evidence for anisotropy-induced shear-wave splitting, *Geophys. J. R. astr. Soc.*, **83**, 61-73.

Booth, D. C., Crampin, S., Chesnokov, E. M., and Krasnova, M. A., 1986. The effects of near-vertical parallel cracks on shear-wave polarizations, *Geophys. J. R. astr. Soc.*, **87**, 583-594.

Brace, W. F., Paulding, B. W., and Scholz, C., 1966. Dilatancy in the fracture of crystalline rocks, *J. geophys. Res.*, **71**, 3939-3953.

Brady, B. T., 1974. Theory of earthquakes I. A scale independent theory of rock failure, *Pure appl. Geophys.*, **112**, 701-725.

Brady, B. T., 1975. Theory of earthquakes II. Inclusion theory of crustal earthquakes, *Pure appl. Geophys.*, **113**, 149-168.

Brodov, L. Y., Evstifeyev, V. I., Karus, E. V., and Kulichikhina, T. N., 1984. Some results of the experimental study of seismic anisotropy of sedimentary rocks using different types of waves, *Geophys. J. R. astr. Soc.*, **76**, 191-200.

Browitt, C. W. A., Turbitt, T., and Morgan, S. N., 1985. Investigation of British earthquakes using the national monitoring network of the British Geological Survey, *Earthquake engineering in Britain*, 33-47, Thomas Telford, London.

Brown, L., DeVoogd, B., and Wille, D., 1985. Seismic "bright spots" and deep crustal fluids, paper presented at the 23rd General Assembly of the International Association of Seismology and Physics of the Earth's Interior, Tokyo, August 1985.

Buchbinder, G. G. R., 1985. Shear-wave splitting and anisotropy in the Charlevoix seismic zone, Quebec, *Geophys. Res. Lett.*, **12**, 425-428.

Burley, A. J., and Edmunds, W. M., 1978. Catalogue of geothermal data for the land area of the United Kingdom, *Inst. Geol. Sci. Report*, published by the Department of Energy.

Butler, R., 1985. Anisotropic propagation of *P*- and *S*-waves in the western Pacific lithosphere, *Geophys. J. R. astr. Soc.*, **81**, 89-101.

Carlson, R. L., Schaftenaar, C. H., and Moore, R. P., 1984. Causes of compressional-wave anisotropy in carbonate-bearing deep-sea sediments. *Geophysics*, **49**, 525-532.

Chen, T-C., Booth, D., and Crampin, S., 1986. Temporal variations in shear-wave splitting: observations near the North Anatolian Fault, 1979-1984, *Geophys. J. R. astr. Soc.*, in preparation.

Christensen, N. I., 1965. Compressional wave velocities in metamorphic rocks at pressures to 10 kilobars, *J. geophys. Res.*, **70**, 6147-6164.

Christensen, N. I., 1966. Shear wave velocities in metamorphic rocks at pressures to 10 kilobars, *J. geophys. Res.*, **71**, 3549-3556.

Christensen, N. I., 1984. The magnitude, symmetry and origin of upper mantle anisotropy based on fabric analysis of ultramafic tectonites. *Geophys. J. R. astr. Soc.*, **76**, 89-111.

Cormier, V. F., 1984. The polarization of S waves in a heterogeneous isotropic Earth model, *J. Geophys.*, **56**, 20-23.

Crampin, S., 1978. Seismic wave propagation through a cracked solid: polarization as a possible dilatancy diagnostic, *Geophys. J. R. astr. Soc.*, **53**, 467-496.

Crampin, S., 1981. A review of wave motion in anisotropic and cracked elastic-media, *Wave motion* **3**, 343-391.

Crampin, S., 1984a. Anisotropy in exploration seismics, *First Break*, **2**, 19-21.

Crampin, S., 1984b. Effective anisotropic elastic constants for wave propagation through cracked solids, *Geophys. J. R. astr. Soc.* **76**, 135-145.

Crampin, S., 1984c, An introduction to wave propagation in anisotropic media, *Geophys. J. R. astr. Soc.*, **76**, 17-28.

Crampin, S., 1984d. The behaviour of shear waves at the free surface, *British Geological Survey Global Seismology Unit Report 215.*

Crampin, S., 1985a. Evaluation of anisotropy by shear-wave splitting, *Geophysics*, **50**, 142-152.

Crampin, S., 1985b. Evidence for aligned cracks in the Earth's crust, *First Break*, **3**, 12-15.

Crampin, S., 1986a. The geological and industrial implications of extensive-dilatancy anisotropy, *Nature*, in preparation

Crampin, S., 1986b. Anisotropy and transverse isotropy, *Geophys. Prosp.*, **34**, 94-99.

Crampin, S., 1986c. Crack porosity and alignment from shear-wave VSPs, in *Shear wave exploration*, ed. Danbom, S. H., and Domenico, S. N., SEG Special Publication, in press.

Crampin, S., and Atkinson, B. K., 1985. Microcracks in the Earth's crust, *First Break*, **3**, 16-20.

Crampin, S., and Booth, D. C., 1985. Shear-wave polarizations near the North Anatolian Fault - II. Interpretation in terms of crack-induced anisotropy, *Geophys. J. R. astr. Soc.*, **83**, 75-92.

Crampin, S., and Bush, I., 1986. Shear waves revealed: extensive-dilatancy anisotropy confirmed, *Expanded abstracts with biographies, 1986 technical program, 56th annual international SEG meeting*, 481-484, Society of Exploration Geophysicists, Houston, Texas, USA.

Crampin, S., and Radovich, B. J., 1982. Interpretation of synthetic common-depth-point gathers for a single anisotropic layer, *Geophysics*, **47**, 323-335.

Crampin, S., Evans, J. R., Üçer, S. B., Doyle, M., Davis, J. P., Yegorkina G. V., and Miller, A., 1980. Observations of dilatancy-induced polarization anomalies and earthquake prediction, *Nature*, **286**, 874-877.

Crampin, S., Stephen, R., and McGonigle, R., 1982. The polarization of P-waves in anisotropic media, *Geophys. J. R. astr. Soc.*, **68**, 477-485.

Crampin, S., Chesnokov, E. M., and Hipkin, R. G., 1984a. Seismic anisotropy - the state of the art: II, *Geophys. J. R. astr. Soc.*, **76**, 1-16.

Crampin, S., Evans, J. R., and Atkinson, B. K., 1984b. Earthquake prediction: a new physical basis, *Geophys. J. R. astr. Soc.* **76**, 147-156.

Crampin, S., Evans, J. R., and Üçer, S. B., 1985. Analysis of records of local earthquakes: the Turkish Dilatancy Projects (TDP1 and TDP2), *Geophys. J. R. astr. Soc.*, **83**, 1-16.

Crampin, S., Booth, D. C., Krasnova, M. A., Chesnokov, E. M., Maximov, A. B., and Tarasov, N. T., 1986a. Shear-wave polarizations in the Peter the First range indicating crack-induced anisotropy in a thrust-fault regime, *Geophys. J. R. astr. Soc.*, **84**, 401-412.

Crampin, S., McGonigle, R., and Ando, M., 1986b. Extensive-dilatancy anisotropy beneath Mount Hood, Oregon, and the effect of aspect ratio on seismic velocities through aligned cracks, *J. geophys. Res.*, **91**, 12703-12710.

Crampin, S., Bush, I., Naville, C., and Taylor, D. B., 1986c. Estimating the internal structure of reservoirs with shear-wave VSPs, *The Leading Edge*, 5, no. 11, 35-39.

Croudace, I. W., 1982. The geochemistry and petrogenesis of the Lower Paleozoic granitoids of the Lleyn Peninsula, North Wales, *Geochim. Cosmochim. Acta* , **46**, 609-622.

Das, S., and Scholz, C. H., 1981. Theory of time-dependent rupture in the Earth, *J. Geophys. Res.*, **86**, 6039-6051.

Davis, E. E., and Clowes, R. M., 1986. High velocities and seismic anisotropy in Pleistocene turbidites off Western Canada, *Geophys. J. R. astr. Soc.*, **84**, 381-399.

DiSiena, J. P., Gaiser, J. E., and Corrigan, D., 1984. Horizontal components and shear wave analysis of three-component VSP data, in *Vertical Seismic Profiling, part B: Advanced Concepts*, 177-188, ed. Toksöz, M. N., and Stewart, R. R., *Handbook of Geophys. Exp.*, **14B.**, Geophys. Press, London.

Dobrovolsky, I. P., Zubkov, S. I., and Miachkin, V. I., 1979. Estimation of the size of earthquake preparation zones, *Pure appl. Geophys.*, **117**, 1025-1044.

Douglas, T. H., Richards, L. R., and O'Neill, D., 1977. Site investigation for main underground complex - Dinorwic pumped storage scheme, in *Field measurements in rock mechanics*, **2**, 551-567, ed. Kovári, K., A. A. Balkema, Rotterdam.

Doyle, M., McGonigle, R., and Crampin, S., 1982. The effects of crack anisotropy on the hypocentral locations of local earthquakes, *Geophys. J. R. astr. Soc.*, **69**, 137-157.

Doyle, M., Crampin, S., McGonigle, R., and Evans, J. R., 1985. Inversion of arrival-times in a region of dilatancy anisotropy, *Pure appl. Geophys.*, **123**, 375-387.

Drummond, B. J., 1985. Seismic *P*-wave anisotropy in the subcrustal lithosphere of north-west Australia, *Geophys. J. R. astr. Soc.*, **81**, 497-519.

Edwards, J. W. F., and Blundell, D. J., 1984. Summary of seismic refraction experiments in the English Channel, Celtic Sea and St. George's Channel, *British Geological Survey, Marine Surveys Directorate, Marine Geophysics Research Programme, report no. 144.*

Evans, J. R., 1984a. Effects of the free surface on shear wavetrains, *Geophys. J. R. astr. Soc.*, **76**, 165-172.

Evans, J. R., 1984b. Anisotropy: a pervasive feature of fault zones?, *Geophys. J. R. astr. Soc.*, **76**, 157-163.

Fletcher, J. B., Haar, L. C., Vernon, F. L., Baker, L. M., Berger, J., Hanks, T. C., and Brune, J. N., 1986a. The digital array at Anza, CA: processing and initial interpretation of source parameters, *J. Geophys. Res.*, in press.

Fletcher, J. B., Haar, L. C., Vernon, F. W., Brune, J. N., Hanks, T. C., and Berger, J., 1986b. The effects of attenuation on the scaling of source parameters for earthquakes at Anza, California, *Proceedings of the fifth Ewing symposium, Arden House, N.Y.*, Amer. Geophys. Union monograph.

Francis, T. J. G., 1969. Generation of seismic anisotropy in the upper mantle along the mid-ocean ridges, *Nature*, **221**, 162-165.

Frankel, A., 1984. Source parameters of two M_l ~ 5 earthquakes near Anza, California, and a comparison with an Imperial Valley aftershock, *Bull. seism. Soc. Am.*, **74**, 1509-1527.

Fyfe, W. S., Price, N. J., and Thompson, A. B., 1978. Fluids in the Earth's crust, *Developments in geochemistry*, 1, Elsevier, Amsterdam.

Garbin, H. D., and Knopoff, L., 1973. The compressional modulus of a material permeated by a random distribution of circular cracks, *Q. Appl. Math*, **30**, 453-464.

Garbin, H. D., and Knopoff, L., 1975(a). The shear modulus of a material permeated by a random distribution of free circular cracks, *Q. Appl. Math.*, **33**, 296-300.

Garbin, H. D., and Knopoff, L., 1975(b). Elastic moduli of a medium with liquid-filled cracks, *Q. Appl. Math.*, **33**, 301-303.

Gilbert, F., and Knopoff, L., 1961. The directivity problem for a buried line source, *Geophysics*, **26**, 626-634.

Gold, T., and Soter, S., 1980. The deep-earth-gas hypothesis, *Sci. Am.*, **242**, no. 6., 130-137.

Gough, D. I., 1986. Seismic reflectors, conductivity, water and stress in the continental crust, *Nature*, **323**, 143-144.

Greiner, G., and Illies, J. H., 1977. Central Europe: active or residual stresses, *Pure appl. Geophys.*, **115**, 11-26.

Hadley, K., 1975. Azimuthal variation of dilatancy, *J. geophys. Res.*, **80**, 4845-4850.

Harker, A., 1950. *Metamorphism*, 3rd edition, Chapman and Hall, London.

Hartzell, S., and Brune, J. N., 1979. The Horse Canyon earthquake of August 2, 1975 - two-stage stress release process in a strike-slip earthquake, *Bull. seism. Soc. Am.* **69**, 1161-1173.

Helbig, K., 1984. Anisotropy and dispersion in periodically layered media, *Geophysics*, **49**, 364-373.

Hess, H. H., 1964. Seismic anisotropy of the uppermost mantle under oceans, *Nature*, **203**, 629-631.

Hudson, J. A., 1980. Overall properties of a cracked solid, *Math. Proc. Camb. Phil. Soc.*, **88**, 371-384.

Hudson, J. A., 1981. Wave speeds and attenuation of elastic waves in material containing cracks. *Geophys. J. R. astr. Soc*, **64**, 133-150.

Kaarsberg, E. A., 1968. Elasticity studies of isotropic and anisotropic rock samples, *Trans. Soc. Min. Engrs.*, **241**, 470-475.

Kaneshima, S., Crampin, S., and Ando, M., 1986a. Shear-wave splitting above small earthquakes in the Kinki District of Japan, *Phys. Earth Planet. int.*, in press.

Kaneshima, S., Ito, H., and Sugihara, M., 1986b. S-wave polarization anisotropy observed in the rift valley of Japan, paper presented at the Second International Workshop on Seismic Anisotropy, Moscow, May 1986.

Kawasaki, I., Suzuki, Y., and Sato, R., 1973. Seismic waves due to a shear fault in a semi-infinite medium. Part I: point source, *J. Phys. Earth,* **21**, 251-284.

Keith, C. M., and Crampin, S., 1977a. Seismic body waves in anisotropic media: reflection and refraction at a plane interface, *Geophys. J. R. astr. Soc.,* **49**, 181-208.

Keith, C. M., and Crampin, S., 1977b. Seismic body waves in anisotropic media: propagation through a layer, *Geophys. J. R. astr. Soc.,* **49**, 209-223.

Keith, C. M., and Crampin, S., 1977c. Seismic body waves in anisotropic media: synthetic seismograms, *Geophys. J. R. astr. Soc.,* **49**, 225-243.

Klein, F. W., 1978. Hypocenter location program HYPOINVERSE Part 1: user's guide to versions 1, 2, 3, and 4, *U.S. Geol. Surv. open-file report 78-694.*

Klein, R. J., and Brown, E. T., 1983. The state of stress in British rocks, *Rep. Dept. Environ.,* DOE/RW/83.060.

Kohler, W. M., Healy, J. H., and Wegener, S. S., 1982. Upper crustal structure of the Mount Hood, Oregon, region as revealed by time term analysis, *J. geophys. Res.,* **87**, 339-355.

Koslovsky, Ye. A., 1984. The world's deepest well, *Sci. Am.,* **251**, no. 6, 106-112.

Kranz, R. L., 1983. Microcracks in rocks: a review. *Tectonophys.* **100**, 449-480.

Lee, W. H. K., and Lahr, J. C., 1975. HYPO71 (revised): a computer program for determining hypocenter, magnitude, and first motion pattern of local earthquakes, *U.S. Geological Survey Open-file report 75-311.*

Levin, F. K., 1978. The reflection, refraction, and diffraction of waves in media with elliptic velocity dependence, *Geophysics*, **43**, 528-537.

Liu, H-S., 1983. A dynamical basis for crustal deformation and seismotectonic block movements in central Europe, *Phys. Earth Planet. int.*, **32**, 146-159.

Logan, A. L. L., 1986. Accurate relative location of similar earthquakes, *PhD thesis*, University of Edinburgh.

Main, I. G., 1985. Seismotectonics and seismic hazard in areas of differing crustal deformation rates. *PhD thesis*, University of Edinburgh.

Mardia, K. V., 1972. *Statistics of directional data*, Academic Press, London.

Marrow, P., and Walker, A., 1986. Lleyn earthquake of 19th July 1984: aftershock sequence and focal mechanism, *Geophys. J. R. astr. Soc.*, in preparation.

Melia, P. J., and Carlson, R. L., 1984. An experimental test of P-wave anisotropy in stratified media, *Geophysics*, **49**, 374-378.

Mjachkin, V. I., Brace, W. F., Sobolev, G. A., and Dieterich, J. H., 1975. Two models of earthquake forerunners, *Pure appl. Geophys.*, **113**, 169-181.

Nur, A., and Simmons, G., 1969. Stress-induced velocity anisotropy in rock: an experimental study, *J. geophys. Res.*, **74**, 6667-6674.

Nuttli, O., 1961. The effect of the Earth's surface on the S wave particle motion, *Bull. seism. Soc. Am.*, **51**, 237-246.

Ohtake, M., 1973. Change in the V_p/V_s ratio related with occurrence of some shallow earthquakes in Japan, *J. Phys. Earth.*, **21**, 173-184.

Peacock, S., and Crampin, S., 1985. Shear-wave vibrator signals in transversely isotropic shale, *Geophysics*, **50**, 1285-1293.

Peacock, S., Crampin, S., and Fletcher, J. B., 1986. Shear-wave splitting in the Anza seismic gap, Southern California: temporal changes at one station - a possible precursor? *J. geophys. Res.*, submitted.

Postma, G. W., 1955. Wave propagation in a stratified medium, *Geophysics*, **20**, 780-806.

Poupinet, G., Fréchet, J., Ellsworth, W. L., Frémont, M. J., and Glangeaud, F., 1985. Doublet analysis: improved accuracy for earthquake prediction studies, *Earthq. Predict. Res.*, **1**, 147-159.

Puzyrev, N. N., Obolentseva, I. R., Trigubov, A. V., and Gorshkalev, S. B., 1984. On the anisotropy of sedimentary rocks from shear-wave analysis. *Geophys. J. R. astr. Soc.*, 76, 243-252.

Raitt, R. W., Shor, G. G., Francis, T. J. G., and Morris, G. B., 1969. Anisotropy of the Pacific upper mantle, *J. geophys. Res.*, **74**, 3095-3109.

Rikitake, T., 1976. *Earthquake Prediction*, Developments in solid earth geophysics, **9**, Elsevier, Amsterdam.

Roberts, B., 1967. Succession and structure in the Llwyd Mawr syncline, Caernarvonshire, North Wales, *Geol. J.*, **5**, 369-390.

Roberts, B., 1979. *The geology of Snowdonia and Llŷn: an outline and field guide*, Adam Hilger, Bristol.

Roberts, G., and Crampin, S., 1986. Shear wave polarizations in a Hot Dry Rock geothermal reservoir: anisotropic effects of fractures, *Int. J. Rock. Mech. Min. Sci & Geomech. Abstr.*, **23**, 291-302.

Robertson, J. D., and Corrigan, D., 1983. Radiation patterns of a shear-wave vibrator in near-surface shale, *Geophysics*, **48**, 19-26.

Sanders, C. O., and Kanamori, H., 1984. A seismotectonic analysis of the Anza seismic gap, San Jacinto fault zone, Southern California, *J. geophys. Res.* **89**, 5873-5890.

Sato, H., 1986. Temporal change in attenuation intensity before and after the Eastern Yamanashi earthquake of 1983 in Central Japan, *J. geophys. Res.*, **91**, 2049-2061.

Savage, J. C., Prescott, W. H., Lisowski, M., and King, N. E., 1981. Strain accumulation in Southern California, 1973-1980, *J. geophys. Res.*, **86**, 6991-7001.

Scholz, C. H., Sykes, L. R., and Aggarwal, Y. P., 1973. Earthquake prediction: a physical basis, *Science*, **181**, 803-810.

Semenov, A. M., 1969. Variation in the travel-time of transverse and longitudinal waves before violent earthquakes (in Russian), *Izv. Akad. Nauk., SSSR, Fiz. Zemli.* **4**, 72-77; 245-248 of Amer. Geophys. Union English edition.

Shankland, T. J., and Ander, M. E., 1983. Electrical conductivity, temperatures, and fluids in the lower crust, *J. geophys. Res.*, **88**, 9475-9484.

Sharp, R. V., 1967. San Jacinto Fault Zone in the Peninsular Ranges of Southern California, *Bull. geol. Soc. Am.*, **78**, 705-730.

Shearer, P., and Orcutt, J., 1985. Anisotropy in the oceanic lithosphere - theory and observations from the Ngendei seismic refraction experiment in the south-west Pacific, *Geophys. J. R. astr. Soc.*, **80**, 493-526.

Simmons, G., and Richter, D., 1976. Microcracks in rocks, in *Physics and chemistry of minerals and rocks*, 105-137, ed. Strens, R. G. J., J. Wiley and Sons, New York.

Smith, D. L., and Evans, B., 1984. Diffusional crack healing in quartz, *J. geophys. Res.*, **89**, 4125-4135.

Smith, W. D., 1986. Evidence for precursory changes in the frequency-magnitude *b*-value, *Geophys. J. R. astr. Soc.*, **86**, 815-838.

Taylor, D. B., 1986. *Aniseis Manual*, Macroc Ltd., Edinburgh.

Thatcher, W., 1981. Crustal deformation studies and earthquake prediction research, in *Earthquake Prediction, an international review*, 394-410, ed. Simpson, D. W., and Richards, P. G., Maurice Ewing series, **4**, Amer. Geophys. Union, Washington D. C.

Thatcher, W., Hileman, J. A., and Hanks, T. C., 1975. Seismic slip distribution along the San Jacinto fault zone, Southern California, and its implications, *Bull. geol. Soc. Am.*, **86**, 1140-1146.

Tremlett, W. E., 1962. The geology of the Nefyn-Llanaelhaiarn area of North Wales, *Lpool Manchr. Geol. J.*, **3**, 157-176.

Tremlett, W. E., 1964. The geology of the Clynnog-fawr district and Gurn Ddu hills of northeast Lleyn, *Geol. J.*, **4**, 207-223.

Tremlett, W. E., 1965. The geology of the Chwilog area of southeastern Lleyn (Caernarvonshire), *Geol. J.*, **4**, 435-448.

Trodd, H., Warburton, P., and Pooley, C. I., 1985. The great British earthquake of 1984 seen from afar, *Geophys. J. R. astr. Soc.*, **83**, 809-812.

Turbitt, T., and Stewart, D. A., 1982. Calibration of the Willmore Mk IIIa/Geostore seismic recording system, *Inst. Geol. Sci. Global Seismology Unit report no. 158.*

Turbitt, T., Barker, E. J., Browitt, C. W. A., Howells, M., Marrow, P. C., Musson, R. M. W., Newmark, R. H., Redmayne, D. W., Walker, A. B., Jacob, A. W. B., Ryan, E., and Ward, V., 1985. The North Wales earthquake of 19 July 1984, *J. Geol. Soc. London* **142**, 567-571.

Whitcomb, J. H., Garmany, J. D., and Anderson, D. L., 1973. Earthquake prediction: variation of seismic velocities before the San Fernando earthquake, *Science*, **180**, 632-635.

White, R. S., and Whitmarsh, R. B., 1984. An investigation of seismic anisotropy due to cracks in the upper oceanic crust at 45°N, Mid-Atlantic Ridge, *Geophys. J. R. astr. Soc.*, **79**, 439-467.

Wyss, M., 1975. Precursors to the Garm earthquake of March 1969, *J. geophys. Res.*, **80**, 2926-2930.

Young, R. P., Hill, J. J., and Bryan, I. R., 1984. Seismic anisotropy in coal measures strata (abstract), *Geophys. J. R. astr. Soc.*, **77**, 318.

Zoback, M. L., and Zoback, M., 1980. State of stress in the conterminous United States, *J. Geophys. Res.*, **85**, 6113-6156.

Zykov, Y. D., Lyakhovitskiy, F. M., and Chervinskaya, O. P., 1984. Experimental investigation of transverse isotropy in ice/clay thin-layered periodic models, *Geophys. J. R. astr. Soc.*, **76**, 269-272.

GEOPHYSICS, VOL. 50, NO. 8 (AUGUST 1985); P. 1285–1293, 10 FIGS., 2 TABLES.

Shear-wave vibrator signals in transversely isotropic shale

Sheila Peacock* and Stuart Crampin‡

ABSTRACT

The experiments of Robertson and Corrigan (1983) on shale are among the first three-component field observations of shear waves in transversely isotropic media to be published. Their data are reprocessed to highlight the effects of the shale's anisotropy on shear waves. Two results emerge. First, shear-wave splitting in a transversely isotropic substrate is most easily observed when the vibrator baseplate is oriented so that both *SH*- and *SV*-waves reach the geophone. Second, the *SV*-wave polarization deviates significantly from perpendicular to the raypath. Both results may significantly affect the interpretation. Both are found to agree with theoretical results and are modeled successfully by synthetic seismograms.

INTRODUCTION

A shear-wave vibrator used with a three-component well geophone is a powerful tool for detecting and quantifying anisotropy in near-surface rock formations. Three reasons for this are: (1) three-component records of shear wavetrains, from which polarizations can be determined, can give more than three times as much information about the raypath as equivalent recordings of *P* wavetrains (Crampin, 1985); (2) the signal from the shear-wave vibrator shows these polarizations relatively uncontaminated by *P*-waves; and (3) downhole recording avoids the complicated interactions of shear waves with the free surface (Evans, 1984).

Robertson and Corrigan (1983) demonstrated use of a shear-wave vibrator in deriving elastic constants and shear-wave surfaces in shales, in an experiment aimed originally at determining the radiation patterns of the vibrator. We present two results of reprocessing their data: (1) shear-wave splitting can be easily recognized in a single three-component record when the vibrator baseplate is oriented at angles other than parallel or perpendicular to the shot-borehole line; and (2) deviations of the *SV*-wave polarization and group-velocity directions from the phase-velocity direction are significant, and must be recognized if the data are to be interpreted correctly.

Finally, we model both these results with synthetic seismograms of plane waves passing through a homogeneous transversely isotropic layer.

SHEAR WAVES IN TRANSVERSELY ISOTROPIC MEDIA

Shear-wave splitting

The shale at both experiment sites studied by Robertson and Corrigan is transversely isotropic, that is, it has hexagonal anisotropic symmetry about a vertical axis. A shear wave entering such a medium splits into two components with fixed polarizations, *SH* and *SV*, and with generally different velocities, which vary with the angle of incidence of the wave to the symmetry axis. Shear-wave splitting (shear-wave birefringence or double refraction) can be observed when shear waves of mixed polarity have passed through the medium in a direction in which the *SH* and *SV* velocities differ. Waves of one polarity travel faster than waves of the other, and the difference in arrival times of the *SH* and *SV* components increases with the path length through the anisotropic medium. The waveform of the original signal is lost, and three-component records show abrupt changes in particle-motion direction as the two shear waves with different polarizations arrive separately.

Polarization and group-velocity directions

Particle-motion polarizations of the three different body waves in anisotropic media also vary with incidence angle (Crampin, 1981). The three body waves traveling in a given phase-velocity direction (defined as the direction normal to the surfaces of constant phase) have mutually orthogonal polarizations, but the *P*-wave polarization is not in general parallel to, nor are the *S*-wave polarizations perpendicular to, the phase-velocity direction. In a transversely isotropic medium, the vertical plane is always a plane of mirror symmetry, so that the *SH*-wave polarization is always horizontal and perpendicular to the phase-velocity direction. *P* and *SV* polarizations lie in the vertical plane containing the propaga-

Manuscript received by the Editor August 15, 1984; revised manuscript received January 30, 1985.
*Department of Geophysics, University of Edinburgh, James Clark Maxwell Building, Mayfield Road, Edinburgh EH9 3JZ, Scotland, U.K.; and British Geological Survey, Murchison House West Mains Road, Edinburgh EH9 3LA, Scotland, U.K.
‡British Geological Survey, Murchison House, West Mains Road, Edinburgh EH9 3LA, Scotland, U.K.

tion vector, but are inclined to the phase-velocity direction at angles which vary with the incidence angle.

When measuring polarizations, we recognize that wave energy arriving at the geophone has traveled in the group-velocity (seismic ray) direction, which also deviates from the phase-velocity direction in anisotropic media (Crampin, 1981). The deviation depends upon the degree and type of symmetry of the anisotropy, the propagation direction, and the type of wave; thus, the three waves arriving at the geophone from a given group-velocity direction have different phase-velocity directions, as shown schematically in Figure 1. We cannot measure the phase-velocity direction at a single three-component geophone, so the polarization angle measured at the geophone is the angle between the polarization and the group-velocity direction, not the angle between the polarization and the phase-velocity direction.

The deviation of *SV* polarization from the normal to the group-velocity direction shows on a three-component seismogram as a small signal on the component parallel to the group-velocity direction, coinciding with the main *SV* arrival on the perpendicular components.

THE EXPERIMENTS OF ROBERTSON AND CORRIGAN

Robertson and Corrigan (1983) recorded shear-wave vibrator shot lines with three-component downhole geophones at two sites: Geary, Oklahoma, where the geophone was at a depth of 430 ft (131 m) in the Permian Dog Creek shale; and Sulphur Springs, Hopkins County, Texas, where two lines were shot running north and east from a geophone buried at 175 ft (53 m) in the Eocene Wills Point formation shale. At both sites the shale extends from the surface to below the depth of the geophone. The arrangement of shotpoints and geophone is shown in Figure 1.

The data from both sites are displayed as record sections in Figures 2, 3, and 6–10 in Robertson and Corrigan (1983). These record sections are for *SH* and *SV* sources separately, so that shear-wave splitting can only be recognized by careful comparison of arrival times from different source orientations. Note a misprint in Figure 7 of Robertson and Corrigan (1983): the values of angle θ along the bottom of that figure should run from 5 degrees to 75 degrees, not 10 degrees to 80 degrees as shown (Robertson, pers. comm.).

DATA PROCESSING TO REVEAL ANISOTROPY

Observing shear-wave splitting on a single three-component seismogram requires a source of mixed polarity shear waves. The shear-wave vibrator baseplate oriented parallel or perpendicular to the shot-borehole line sends waves of only one polarity along the line; intermediate orientations of the baseplate are needed to give mixed polarity shear waves at the geophone. The azimuthal radiation test results in Figures 6 and 14 in Robertson and Corrigan (1983) show such a mixed polarity signal, but since the test was performed at only one vibrator position, we cannot see the signal's variation with incidence angle. To show how this variation might appear, we simulated a shot with baseplate orientation of 45 degrees at each shotpoint of the polar radiation tests (Figures 2, 3, 7, 8, 9, and 10 in Robertson and Corrigan, 1983) by adding vectorially the signals from the radial-baseplate and transverse-baseplate shots.

To investigate the angle between *SV* polarization and group-velocity direction, we assumed that the group-velocity direction was along the straight ray from source to geophone (Figure 1). Robertson and Corrigan found that, at high incidence angles, the *SV* polarization at the geophone appeared to indicate an arrival angle greater than the straight-ray angle; they attributed this to curvature of the raypaths caused by an increase in velocity with depth. For each shot they estimated the difference between the arrival angle and the straight-ray incidence angle by rotating the *P'* (radial) and *SV'* (vertical) components of the signal from radial baseplate motion to give a maximum amplitude arrival on the *SV'* component. This means that their *SV'* component is parallel to the direction of *SV polarization*, which in anisotropic media deviates from the perpendicular to the group-velocity direction (the direction of the raypath). We cannot directly determine the group-velocity direction: by assuming it to be the straight-ray direction, we also assume that the increase in velocity with depth did not cause the raypath to curve significantly. Our results compare the effects of the polarization deviation and the increase in velocity with depth on the measured *SV* arrival angle, and show that Robertson and Corrigan overcompensated for the increase in velocity with depth by not allowing for the effect of the anisotropy-induced polarization deviation.

To observe the polarization, we reoriented the *P'* component records of Robertson and Corrigan parallel to and the *SV'* component perpendicular to the straight-ray direction by rotating both about an angle equal to the difference between the straight-ray and polarization-estimated incidence angles. The *SV*-estimated and straight-ray angles for each shot at Sulphur Springs are listed in Table 1.

RESULTS

We plotted the Sulphur Springs data, after these rotations, as record sections (Figures 2 and 3) and polarization diagrams (Figures 4 and 5). The Geary data, which are not shown, gave similar results.

Center sections in Figures 2 and 3 show mixed *SH* and *SV* signals from the 45 degree baseplate. The 45 degree baseplate

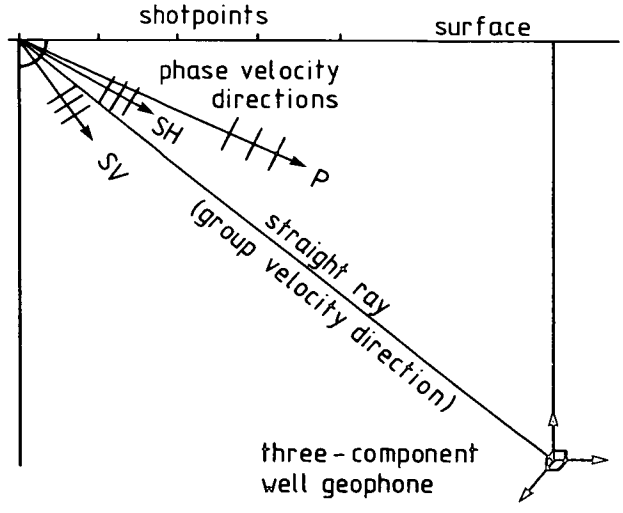

FIG. 1. Layout of experiments by Robertson and Corrigan showing schematic planes of constant phase and divergence of phase velocity from group velocity in a transversely isotropic medium.

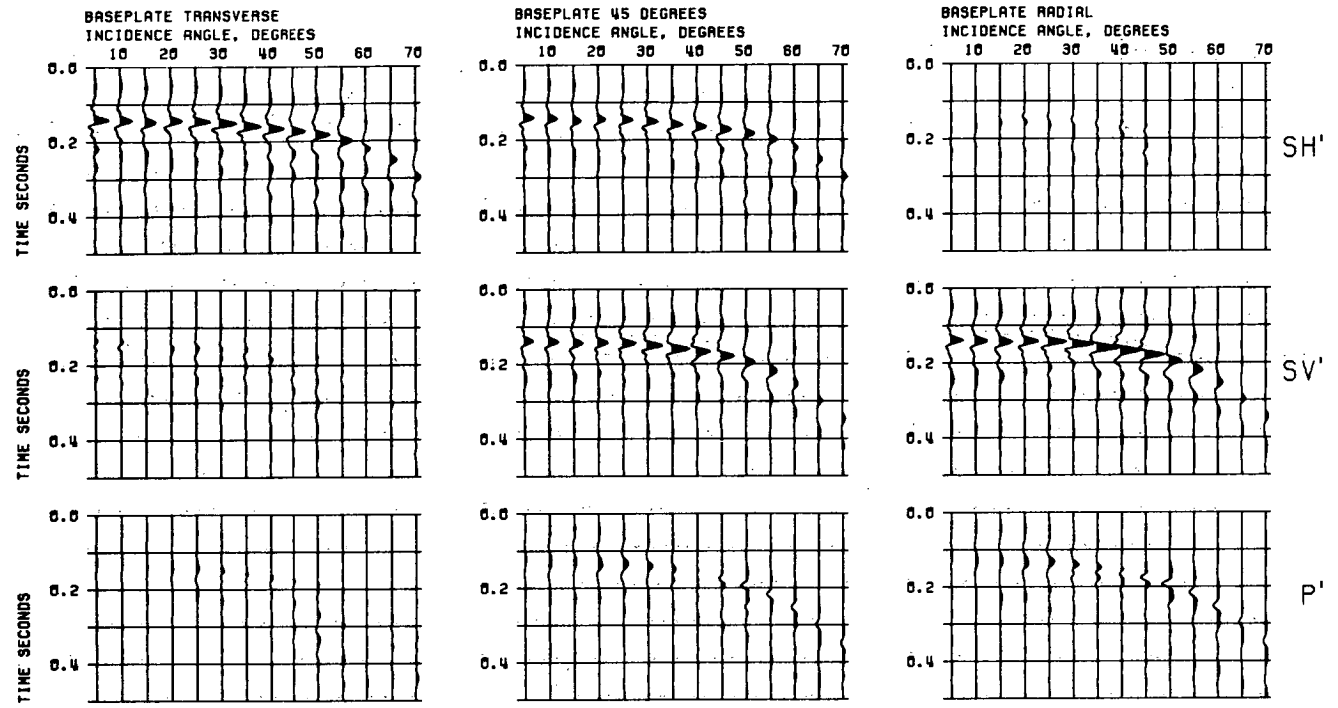

FIG. 2. Sulphur Springs test, east line: observed record sections with baseplate transverse (left) and baseplate radial (right), and simulated sections for baseplate at 45° (center). Reference axes rotated for each shot: straight-ray, P'; perpendicular to the straight ray in the vertical plane, SV'; and horizontal transverse, SH'.

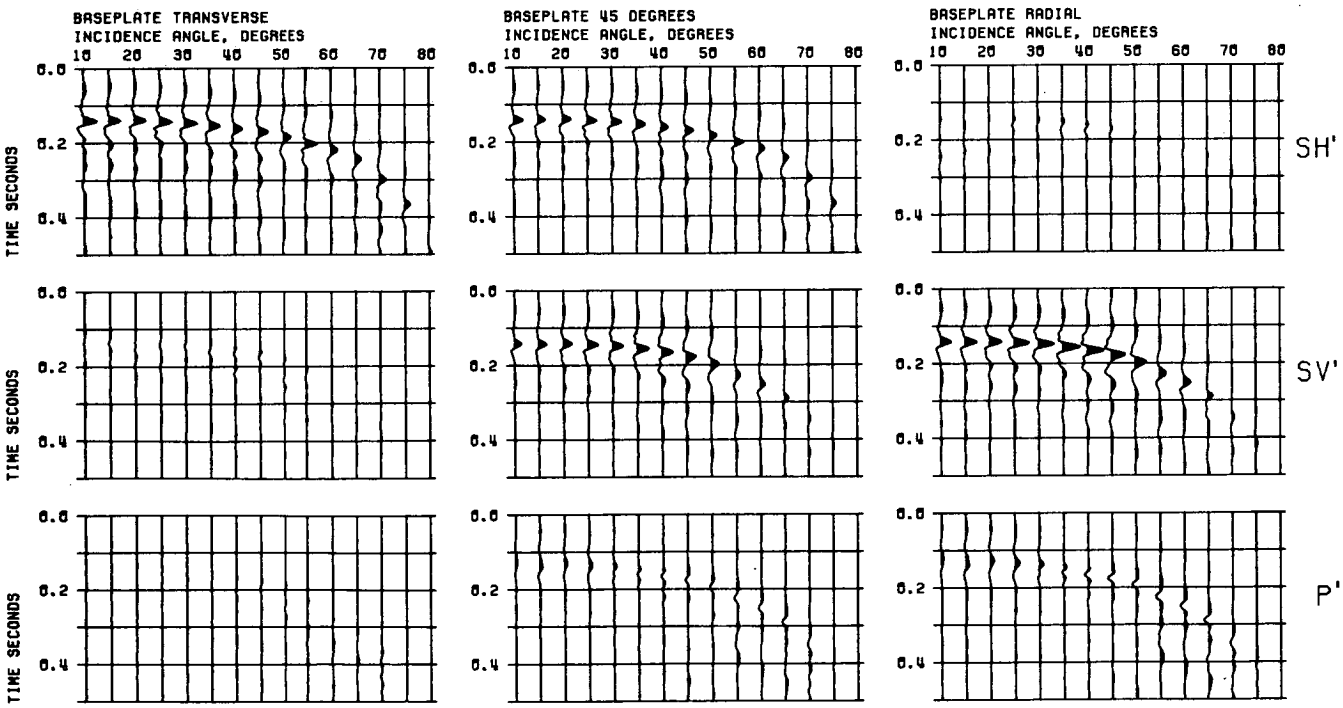

FIG. 3. Sulphur Springs tests, north line. Notation as in Figure 2.

Table 1. *SV*-arrival-derived incidence angles and corresponding straight-ray angles at Sulphur Springs (Robertson, pers. comm.).

Incidence angles in degrees			
East line		North line	
Straight ray	*SV*-derived	Straight ray	*SV*-derived
5	5	10	5
10	5	15	5
15	10	20	10
20	10	25	20
25	20	30	30
30	30	35	40
35	40	40	50
40	50	45	60
45	60	50	70
50	80	55	90
55	85	60	95
60	100	65	105
65	105	70	120
70	115	75	125
		80	130

and the radial baseplate also show small *P'*-component arrivals coincident with the main *SV* arrivals, caused by deviation of the *SV* polarization from perpendicular to the group-velocity direction, and at larger incidence angles, by the curvature of the raypath away from the straight-ray direction.

Shear-wave splitting

Shear-wave splitting is shown by the different arrival times of the *SH*- and *SV*-waves at larger angles of incidence on the simulated three-component seismograms. This difference in arrival time is more clearly displayed in the polarization diagrams in Figures 4a and 4b, which display shear-wave arrivals from the simulated shots with the baseplate at 45 degrees. The degree of splitting of the two shear-wave components increases with the incidence angle. The increase appears in three stages: (1) linear particle motion as the two components arrive almost simultaneously (for incidence angles between 5 degrees and 35 degrees); (2) elliptical motion as the two arrivals are partially separated (incidence angles 40 degrees to 55 degrees); and (3) L-shaped traces as the separation becomes more complete, with the faster *SH*-wave arriving first (incidence angles greater than 55 degrees).

SV-wave polarization anomalies

Polarization diagrams in Figures 5a and 5b are the components of particle displacement parallel (*P'*) and perpendicular (*SV'*) to the straight-ray direction of the *SV* arrival from radial baseplate motion. Both the deviation of *SV* polarization from normal to the straight-ray direction and the refraction of the ray away from the straight raypath cause an inclination of the main *SV* motion from the *SV'*-axis. The motion becomes more inclined to the right of the *SV'*-axis as the incidence angle increases. At small incidence angles the motions are made triangular by the "noise" slightly before the main *SV* arrival. This is probably due to failure of the crosscorrelation process to simulate perfectly a single pulse from the vibrator signal.

Table 2. Elastic constants of the Sulphur Springs shale

		Density = 1.8 g/cm^3 Elastic constants (units 10^9 N/m^2)	
		Robertson and Corrigan	This paper
c_{1111}	A	3.52	3.52
c_{3333}	C	2.02	2.02
c_{2233}	F	2.03	2.02
c_{1313}	L	0.27	0.26
c_{1212}	N	0.42	0.51

COMPARISON WITH THEORY

We compared the results with theoretical variations of wave velocity, polarization angle, and group-velocity deviation angle in the shale at Sulphur Springs. All these variations are calculated from the elastic constants and densities listed in Table 2, and are taken from Table 2 of Robertson and Corrigan (1983). We slightly altered the values calculated by Robertson and Corrigan for the constants F, L, and N to give a marginally better fit of theoretical group velocities to the observed velocities.

Velocities

Observed velocities are compared with recalculated theoretical velocities in Figure 6. They agree well with the theoretical velocities for incidence angles less than 60 degrees; at greater incidence angles the observed velocities of both *SH*- and *SV*-waves are considerably greater than the theoretical values. The most probable cause is an increase in velocity with depth, possibly accompanied by a change in the degree of velocity anisotropy, although the data are insufficient to specify these more exactly.

Theoretical *S*-wave phase and group velocities in the Sulphur Springs shale are plotted in Figure 7 against the theoretical incidence angle of the group-velocity vector. At small incidence angles (less than 35 degrees) the *SV*-wave velocity is almost identical to the *SH*-wave velocity. At greater incidence angles the *SH* and *SV* velocity values separate, and the difference between them is greatest at 90 degrees (horizontal) incidence. In the polarization diagrams of Figures 4a and b, the increasing difference in arrival times of the two shear waves with increasing incidence angle is due partly to the increase in the velocity difference between the two waves and partly to the increase in their travel path length through the anisotropic shale. The curved raypath caused by an increase in velocity with depth lengthens more with increasing incidence angle than does the straight raypath.

Polarization angles

Figure 8a shows the calculated deviations of the phase-velocity vectors of the three body waves from the group-velocity direction, as a function of group-velocity incidence angle in the Sulphur Springs shale. *P* and *SH* phase-velocity incidence angles are consistently less than the group-velocity incidence angle, but the *SV* phase-velocity incidence angle switches rapidly at 40 degrees from being less than the group-

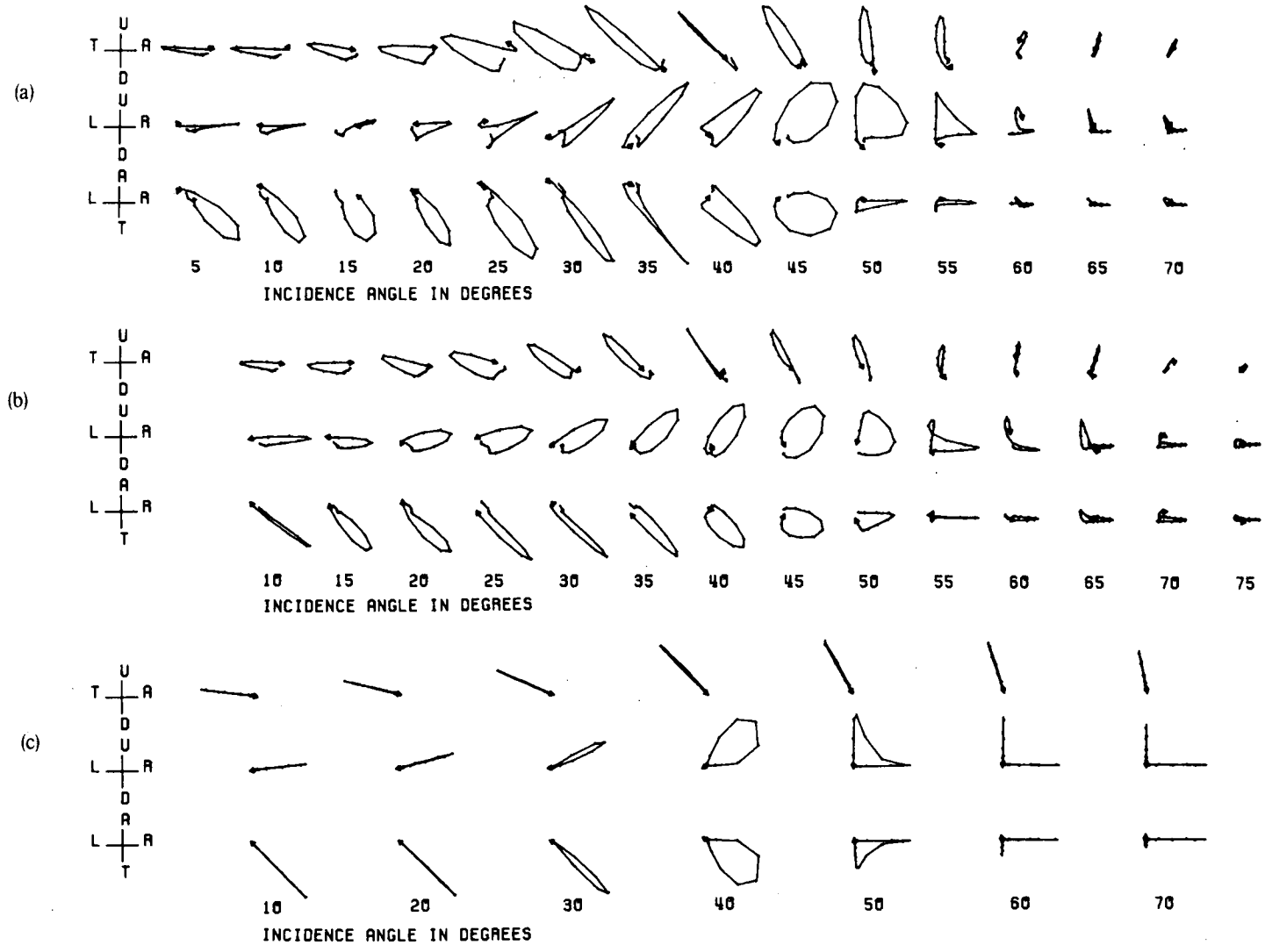

FIG. 4. Polarization diagrams from the simulated shots of Figures 2 and 3 with the baseplate at 45°. (a) East line, from Figure 2. (b) North line, from Figure 3. (c) Corresponding polarization diagrams from synthetic records of Figure 10. Axes rotated to vertical, horizontal radial, and horizontal transverse orientations. Motions shown are up (U), down (D), toward (T) and away (A) from the geophone, and left (L) and right (R) of the source to geophone line.

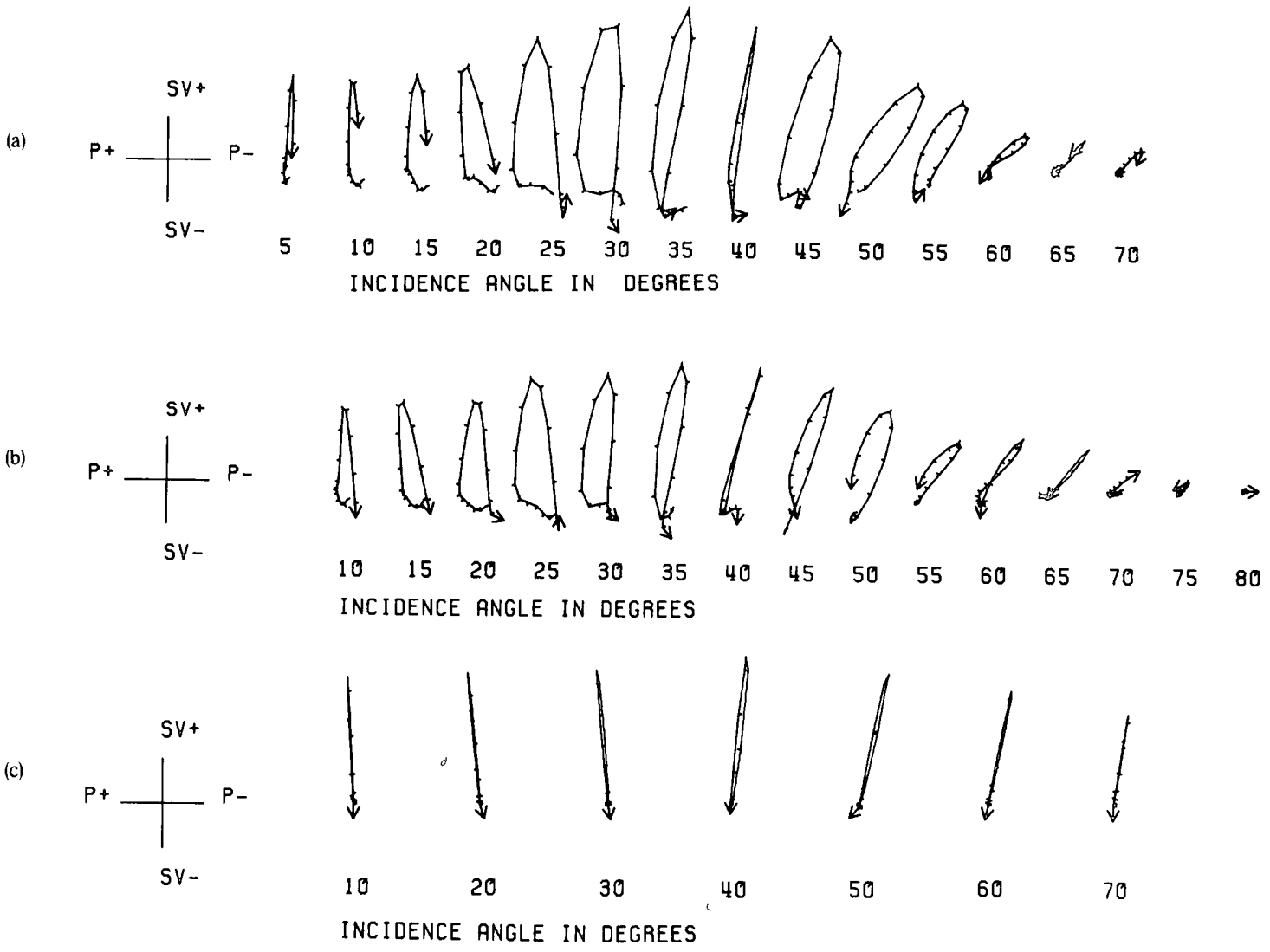

FIG. 5. P'- and SV'-component polarization diagrams from shots with the baseplate radial. (a) East line. (b) North line. (c) Synthetic. Following Robertson and Corrigan, axis labels $P+$ and $P-$ represent motion toward and away from the geophone, respectively, along the straight raypath between shot and geophone. SV represents motion perpendicular to the straight raypath in the vertical plane; $SV+$ is upward and $SV-$ is downward.

velocity angle to being greater than that angle.

The *SV* phase-velocity deviation is plotted again in Figure 8b along with the calculated angle between the *SV* polarization and phase-velocity directions. The sum of these two angles is the angle between the polarization and the group velocity (or ray direction), and it is this angle that can be measured at the geophone. Its variation with incidence angle is shown as a solid line in Figure 8b, and in Figure 9 it is compared with the observed angle between the straight-ray direction and the *SV* polarization in the records of Robertson and Corrigan (data in Table 1).

The observed angle in Figure 9 agrees well with the theoretical for small incidence angles, but for incidence angles larger than 45 degrees the observed angle is much greater than the theoretical. The most probable explanation is again an increase in velocity with depth, which causes the raypaths to curve so that the true incidence angle of the group-velocity vector is larger than the straight-ray incidence angle.

Robertson and Corrigan attributed all observed deviation of *SV* arrival from the straight-ray direction to raypath curvature, but Figure 9 shows the deviation at Sulphur Springs is wholly due to the anisotropy for incidence angles less than 45 degrees, and only at incidence angles greater than about 55 degrees does the effect of the increase in velocity with depth become more significant than the effect of the anisotropy.

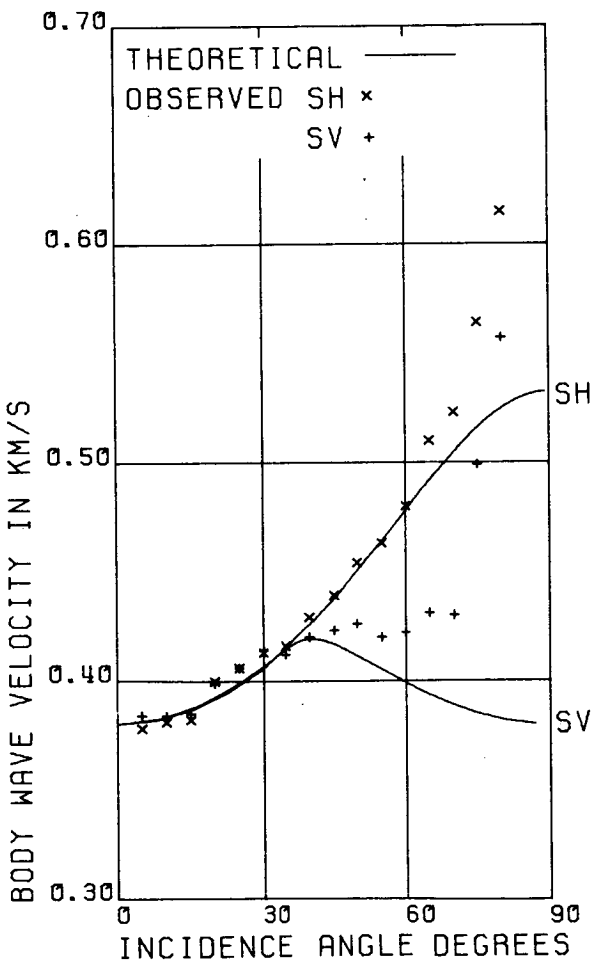

FIG. 6. Observed and theoretical group-velocities at Sulphur Springs plotted at the group-velocity incidence angle.

SYNTHETIC SEISMOGRAMS

The simple arrangement of source, medium, and geophone in the experiments of Robertson and Corrigan is well suited to modeling with synthetic seismograms. We used the program described in Keith and Crampin (1977 a, b) which synthesizes a plane wave propagating through a set of anisotropic layers sandwiched between two isotropic half-spaces. The model used was a single anisotropic layer between the two half-spaces. Plane shear waves with appropriate polarizations are incident on the upper boundary, and the program calculates the signal received at the lower boundary.

We simulated the different incidence angles of the real experiment by altering the orientation of the anisotropic symmetry axis within the layer, rather than by altering the incidence angle of the plane waves. This avoided unwanted mode conversions of waves incident obliquely on the layer interfaces. The orientations of the symmetry axes were chosen to give *group-velocity* incidence angles equal to the straight-ray incidence angles of the real experiment, since energy travels from the source to the geophone at the group velocity. The change in the length of the travel path with incidence angle in the real experiment was modeled by altering the thickness of the anisotropic layer in the model. The real seismograms have already been corrected for spherical divergence, assuming straight-ray propagation. We did not attempt to simulate the remaining decrease in amplitude of the real seismograms with incidence angle, which Robertson and Corrigan attributed to attenuation and to undercorrection for spherical divergence.

Synthetic seismograms for an anisotropic layer with the same elastic constants as the Sulphur Springs shale are shown

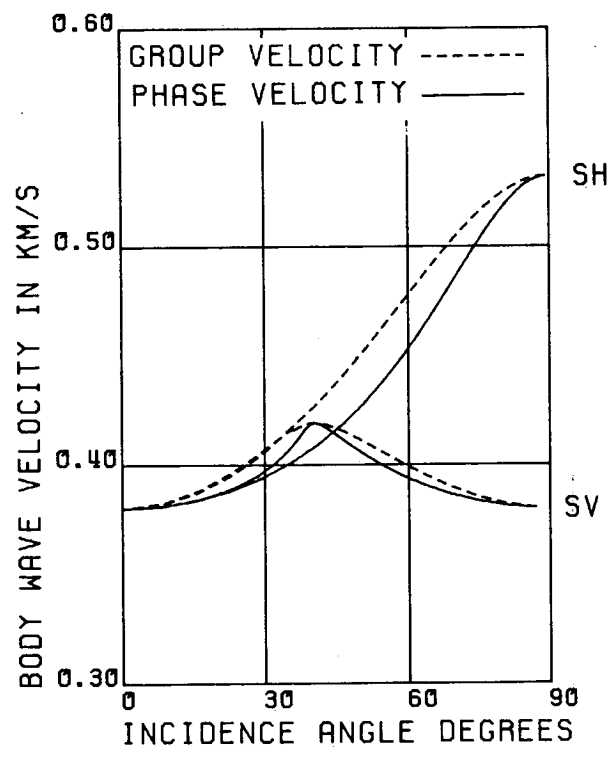

FIG. 7. Calculated variation of *S*-wave phase- and group-velocity with group-velocity incidence angle in the Sulphur Springs shale.

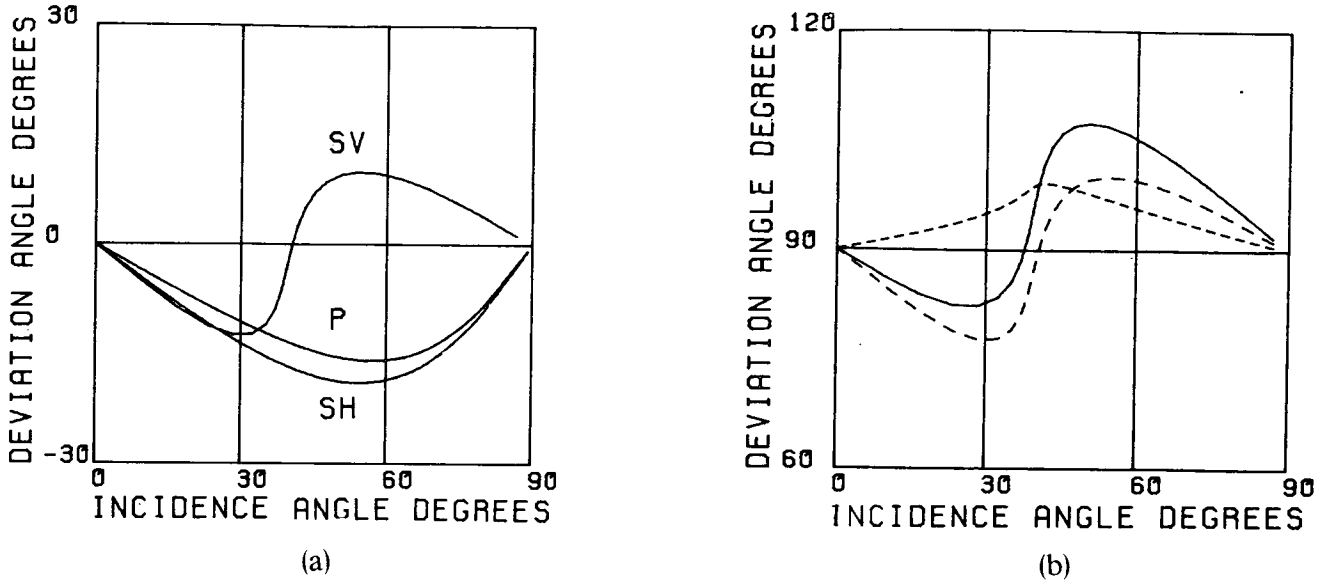

FIG. 8. Variation of calculated deviation angles with group-velocity incidence angle in the Sulphur Springs shale. (a) Deviation of *P*, *SH*, and *SV* phase velocities from the group-velocity direction. (b) Angle between *SV*-wave phase-velocity direction and polarization (short dash); angle between group- and phase-velocity directions, as in (a) (long dash); and resultant angle between polarization and group-velocity direction (solid line).

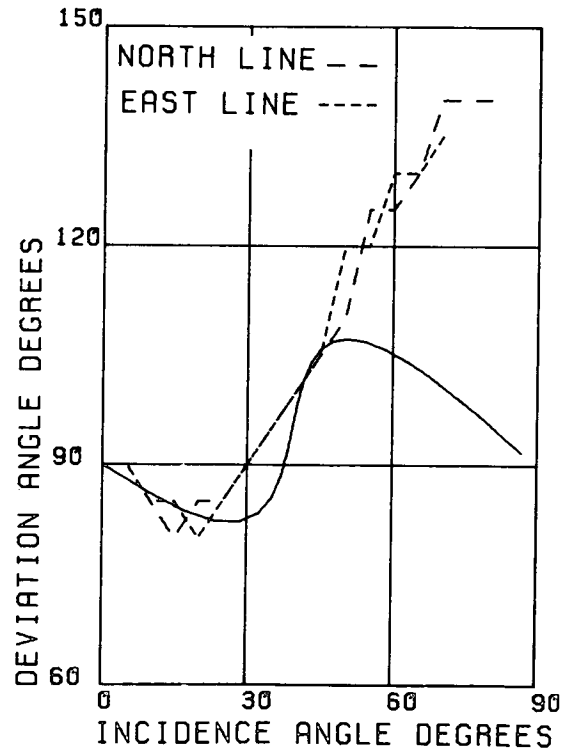

FIG. 9. Observed variation of the angle between *SV* polarization and straight-ray direction at Sulphur Springs (dashed lines), superimposed on the theoretical, anisotropy-induced variation of the angle between *SV* polarization and group-velocity direction, as in Figure 8b (solid line).

in Figure 10, superimposed on the real seismograms from the north shot line. For small incidence angles the synthetic and real seismograms agree well. At incidence angles larger than 50 degrees the real shear-wave arrival is earlier than the synthetic, because the synthetic seismogram model does not allow for any increase in velocity with depth.

In Figure 4c polarization diagrams from the synthetic seismograms of Figure 10 for "baseplate 45 degrees" are compared with the observed particle motions in Figures 4a and 4b. The increase in the degree of shear-wave splitting with increasing incidence angle is reproduced well in the synthetic diagrams.

Figure 5c shows the polarization diagrams of the *SV'* and *P'* components of the synthetic seismogram from an input *SV*-wave. As in Figures 5a and 5b, the inclination of the traces from parallel to the *SV'*-axis is the measure of the deviation of *SV*-wave polarization from perpendicular to the group velocity. The inclination is not as great as in the plots of real data from Sulphur Springs in Figures 5a and 5b, again because the synthetic seismogram model does not include any increase in velocity with depth in the real shale. Refraction caused by an increase in velocity with depth is probably responsible for a large part of the observed deviation of *SV* polarization from the straight-ray direction at high incidence angles (Figures 5 and 9). The deviations of the synthetic polarizations in Figure 5c match the calculated deviation of polarization from group velocity in Figure 9.

CONCLUSIONS

After further processing Robertson and Corrigan's records from transversely isotropic shale, we determine the results expected from three-component recording of the signal from a shear-wave vibrator not oriented radial or transverse to the geophone site. From Figures 2, 3, and 4 we show that a single shot with the baseplate at 45 degrees can reveal as much

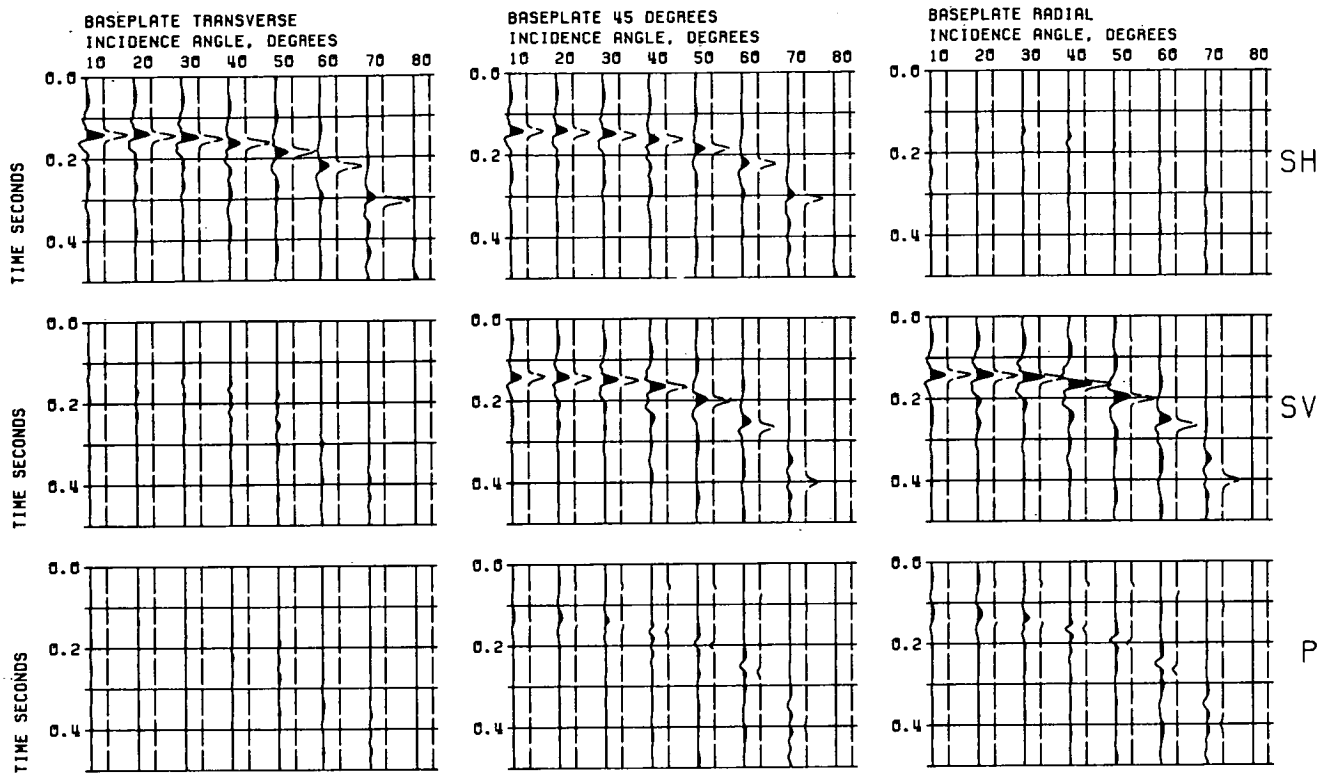

FIG. 10. Synthetic seismograms of *SH*, *SV*, and mixed polarity shear waves passing through the Sulphur Springs shale (dashed lines) compared with the real seismograms (solid lines) from the north shot line (as in Figure 3) at every ten degrees of incidence angle.

about the anisotropy of surface rock layers as two shots at the same site with the baseplate oriented radially and transversely. When data from such a shot are presented as polarization diagrams, shear-wave splitting (probably the most important indicator of anisotropy) can be readily observed, and anisotropy can be recognized from a single three-component trace.

We also investigated polarization anomalies caused by the transverse isotropy of shales at the experiment sites. Anisotropy-induced polarization anomalies in the *SV*-waves gave effects similar to those caused by refraction due to the increase of velocity with depth. Comparison with calculated anomalies shows that the observed polarization anomaly was entirely caused by anisotropy for incidence angles less than 50 degrees, and the anisotropy had a significant effect at larger incidence angles.

This example of misinterpretation of the direction of arrival of the *SV*-wave has important implications for three-component vertical seismic profiles (VSPs). Alignment of the horizontal axes in VSP is often determined by polarization of the shear waves, and ignoring polarization anomalies caused by anisotropy could lead to gross misalignment of the horizontal axes.

Synthetic seismograms model both shear-wave splitting and *SV* polarization anomalies caused by the transversely isotropic shale. This is probably the first detailed observation of particle motions of waves in a transversely isotropic medium modeled by synthetic seismograms. The phase and group velocities, the polarizations, and the shear-wave splitting of the synthetic seismograms agree remarkably well with the real data. Agreement between synthetic and observed records demonstrates the classic simplicity of the experiments of Robertson and Corrigan.

ACKNOWLEDGMENTS

We thank James D. Robertson for his data and for patiently answering our many questions. This work was supported by the Natural Environment Research Council (NERC) and is published with the approval of the Director of the British Geological Survey (NERC).

REFERENCES

Crampin, S., 1981, A review of wave motion in anisotropic and cracked elastic-media: Wave Motion, **3**, 343–391.
——— 1985, Evaluation of anisotropy by shear-wave splitting: Geophysics, **50**, 142–152.
Evans, R., 1984, Effects of the free surface on shear wavetrains: Geophys. J. Roy. Astr. Soc., **76**, 165–172.
Keith, C. M., and Crampin, S., 1977a, Seismic body waves in anisotropic media: reflection and refraction at a plane interface: Geophys. J. Roy. Astr. Soc., **49**, 181–208.
——— 1977b, Seismic body waves in anisotropic media: propagation through a layer: Geophys. J. Roy. Astr. Soc., **49**, 209–223.
Robertson, J. D., and Corrigan, D., 1983, Radiation patterns of a shear-wave vibrator in near-surface shale: Geophysics, **48**, 19–26.